KU LEUVEN

FACULTEIT WETENSCHAPPEN

A compact CZT γ-ray detector for nuclear applications in medicine

Willemijn GOOSSENS

Promotor: Prof. T.E. Cocolios
Instituut voor Kern- en Stralingsfysica
(KU Leuven)

Begeleider: *W. Wojtaczka*
Instituut voor Kern- en Stralingsfysica
(KU Leuven)

Proefschrift ingediend tot het
behalen van de graad van
Master of Science in de Fysica

Academiejaar 2021-2022

Preface

Ever since I started studying physics, I have been interested in medical radiation physics. So, when I saw the thesis topics on the production of medical radioisotopes in the interdisciplinary research group of prof. Thomas Elias Cocolios, I was immediately intrigued. I'm very grateful that I could be a part of this research group for a year.

While working on my thesis, I received support from many people. First and foremost, I want to thank my promoter, prof. Thomas Elias Cocolios, and my supervisor, Wiktoria Wojtaczka. They supported me throughout my whole thesis and guided me in every step of the way. I have enjoyed our interesting discussions and I have learned a lot from both of them. I particularly want to thank Thomas for giving me the opportunity to visit CERN. I found it very fascinating to attend an experiment on-site and it helped me to gain insight in the ISOLDE and MEDICIS facilities. On top of that, it gave me the chance to talk in-person to some of the researchers whom I had previously been in contact with for my thesis. In short, it was an extraordinary experience that I will never forget. Thank you! I also want to thank Wiktoria for helping me during the experiments and for correcting my thesis (even during her holiday!). Thank you for being such a nice supervisor!

Secondly, I want to thank the other members of the research group, who were prepared to help me wherever they could. Special thanks goes out to Michael Heines. He always had useful tips and tricks for the analysis of γ-spectra and so much more. I especially want to thank him for proofreading my entire thesis and for encouraging me throughout the year. I also want to thank Jake Johnson and Cyril Bernerd. From figuring out FLUKA together to setting up measurements in the lab, Jake was always ready to help out. Cyril made sure I was well-informed on any new developments of Tb collections at CERN, and he wrote a code that simplified the series of long measurements for my own experiment.

Next, I want to thank Valérie Augustyns. As member of the radio-protection team at UZ Leuven, she provided all the information I needed on the cyclotron parts from PARTICLE.

Of course, I also want to thank my friends in Leuven and beyond. For the interesting talks about each others theses, but also for the relaxed moments in between.

Last but not least, I want to thank my mother, my grandparents and my godmother. They have truly supported me in every way they could. It has been a stressful year, so I want to thank them especially for their patience. I particularly want to thank my grandfather, for proofreading my thesis and always being prepared to talk things through.

Thank you all!

Contribution Statement

Part of the measurements and simulations presented in parts II and III of this thesis were performed by other people. Therefore, I want to use this space to list all contributors and to thank them for their work.

Michael Heines provided me with his code for the SNIP algorithm. This algorithm was used throughout the analyses of the γ-spectra in parts II and III to approximate the smooth background.

All ^{155}Tb collections and associated measurements discussed in chapter 4 were performed by the team of researchers at MEDICIS. I particularly want to mention Charlotte Duchemin and Cyril Bernerd, who kept me informed on any new developments and provided me with collection reports, logbooks and all the data I needed to make an analysis of the collections. Charlotte also performed the FLUKA simulations of the target irradiation at CERN mentioned in the discussion section of chapter 4.

The FLUKA simulations presented in chapter 6 in the context of waste management at PARTICLE, I performed myself. The SRIM simulations were done by Michael Heines. All the graphs illustrating the results of the SRIM simulations were also made by Michael.

For the spectroscopic study of waste materials from PARTICLE discussed in chapter 7, all known information on the objects was provided by the radio-protection team from UZ Leuven. Part of the investigation on the materials was performed by Ruben Driesen. The results and conclusions of his work can be found in Ref. [1]. In this thesis, only the spectroscopic study with the CZT detector is presented. The calibration of the detector was performed by Kaat Spoormans. Other than that, I performed all of the measurements myself, except during my exam period in January. Then, Wiktoria Wojtaczka and Jake Johnson continued the experiment according to the plan I prepared. For all measurements, a program was used that automatically starts and stops acquisitions at regular time intervals. The code of this program was written by Cyril Bernerd.

Contents

List of Acronyms

ARBIS	Algemeen Reglement op de Bescherming van de bevolking en de werknemers tegen het gevaar van Ioniserende Stralingen
CERN	Conseil Européen pour la Recherche Nucléaire
CZT	Cadmium Zinc Telluride
EC	Electron Capture
FANC	Federaal Agentschap voor Nucleaire Controle
FLUKA	FLUktuierende KAskade
FWHM	Full Width at Half Maximum
HPGe	High Purity Germanium detector
IAEA	International Atomic Energy Agency
IBA	Ion Beam Applications
IKS	Instituut voor Kern- en Stralingsfysica
ISOL	Isotope Separation On-Line
ISOLDE	Isotope Separation On-Line DEvice
MDA	Minimal Detectable Activity
MEDICIS	MEDical Isotopes Collected from ISolde
MELISSA	MEdicis Laser Ion Source for Separator Assembly
MYRRHA	Multi-purpose hYbrid Research Reactor for High-tech Applications
NIRAS	Nationale Instelling voor Radioactief Afval en verrijkte Splijtstoffen
PARTICLE	PARticle Therapy Interuniversity Center LEuven
PET	Positron Emission Tomography

PSB	Proton Synchrotron Booster
RILIS	Resonance Ionisation Laser Ion Source
SCK CEN	StudieCentrum voor Kernenergie / Centre d'Étude de l'énergie Nucléaire
SNIP	Statistics-sensitive Non-linear Iterative Peak-clipping
SPECT	Single Photon Emission Computed Tomography
SRIM	Stopping and Range of Ions in Matter
TAT	Targeted Alpha-Therapy

List of Symbols

Physics Constants

c	Speed of light in vacuum	
h	Planck constant	
k_B	Boltzmann constant	
m_0	Rest mass of an electron	

Recurring Symbols

χ^2_{red}	Reduced χ^2-value (statistics)	
$\epsilon_{abs}(E)$	Absolute detection efficiency	[%]
$\epsilon_{intr}(E)$	Intrinsic efficiency of the detector	[%]
λ	Isotope-specific decay constant	[s^{-1}]
Ω	Solid angle	
σ	Standard deviation of Gaussian distribution	
A	Radioactivity	[Bq]
E	Energy	[eV]
E_g	Bandgap in electronic bandstructure	[eV]
E_γ	Photon energy	[eV]
I	Intensity of radiation	[%]
m	Mass	[kg]
$N(E)$	Number of counts detected	
$R(E)$	Energy resolution	[%]
T	Temperature	[K]

t	Time / Livetime of the measurements	[s]
$T_{1/2}$	Isotope-specific half-life	[s]
Z	Atomic number	

Symbols in Part I

ϵ	Ionisation energy to produce an e-h pair	[eV]
σ	Reaction cross section	[b]
θ	Scattering angle	[°]
N	Number of neutrons	
$N(t)$	Number of radionuclei	
n_{e-h}	Number of electron-hole pairs	

Symbols in Part II

ϵ_{diff}	Diffusion efficiency	[%]
ϵ_{eff}	Effusion efficiency	[%]
$\epsilon_{implant}$	Implantation efficiency	[%]
ϵ_{ion}	Ionisation efficiency	[%]
ϵ_{sep}	Mass separation efficiency	[%]
$\epsilon_{transport}$	Transport efficiency	[%]
B	Magnetic field	[T]
c_{decay}	Correction factor for radioactive decay	
q	Charge	[C]
r	Radius	[m]
v	Velocity	[m/s]

Symbols in Part III

a	Activity concentration	[Bq/kg]
b	Background level at a given energy	
C	Clearance level	[Bq/kg]
D	Detector area	[cm^2]
d	Sample-detector distance	[cm]

Scientific Summary

This thesis presents two case studies for the use of a compact CZT γ-ray detector (manufactured by Kromek) in a medical context. The aim is to evaluate the potential of this type of detector for common nuclear applications in medicine.

CZT γ-ray detectors are a type of semiconductor detectors, made of $Cd_{0.9}Zn_{0.1}Te$. Owing to the particular band structure of the material ($E_g = 1.57\,\text{eV}$), CZT detectors can operate at room temperature. This is a major benefit compared to, for example, HPGe detectors, which must be cooled to limit thermal excitation. Moreover, the CZT detectors of Kromek's GR family, which are considered in this thesis, are compact: the detection crystal and electronics are contained in a $2.5\,\text{cm} \times 2.5\,\text{cm} \times 6.3\,\text{cm}$ casing. Therefore, these detectors can be used in remote places that might be inaccessible to other detection systems. In both case studies, the CZT detector is used for γ-spectroscopy. In this technique, energy spectra of γ-ray emitting samples are investigated to identify and quantify the present radioactive isotopes.

The first case study for the use of a compact Kromek CZT detector involves the production of terbium radioisotopes for medical applications at CERN MEDICIS (Geneva, CH). The Tb radionuclide family is very promising for nuclear medicine, because it contains four radioisotopes with complementary decay characteristics suitable for both imaging and therapy. For the neutron-rich radioisotope, ^{161}Tb, large-scale production has been established at SCK CEN (Mol, BE) by neutron irradiation of Gd targets. The neutron-deficient radioisotopes, ^{149}Tb, ^{152}Tb and ^{155}Tb, are predominantly produced at MEDICIS. In this case, a heavy target of Gd or Ta is irradiated by energetic protons up to 1.4 GeV, and the Tb radioisotopes are separated from the other species by the ISOL (Isotope Separation On-Line) method. Finally, the separated isotopes of interest are collected on implantation foils. At MEDICIS, the Tb activity can be monitored during the collection using the Kromek GR1 CZT detector installed in front of the collection chamber. In this thesis, the γ-spectra acquired by the detector during the ^{155}Tb collections in 2021 are analysed. They show the presence of $^{139}Ce^{16}O$ as isobaric contaminant that is collected together with ^{155}Tb. Furthermore, they indicate that (self-)sputtering occurs in the collection chamber, limiting the amount of ^{155}Tb that stays implanted on the foil. Finally, combined with ion current measurements, the γ-spectra suggest that target conditioning prior to the collection is useful to prevent saturation of the ion source.

In the second case study, a Kromek CZT detector is used in the context of radioactive waste management at the proton therapy facility PARTICLE (Leuven, BE). Due to direct irradiation by the proton beam of 230 MeV or indirect irradiation by scattered protons,

nuclear reactions are induced in the construction elements of the beam-line. A variety of radioisotopes is produced, depending on the composition of the construction material and the energy of the protons. In this manner, radioactive waste is created. To decide on the proper treatment for specific components, the radioisotopes generated in them must be identified and quantified. In this thesis, that is done with a Kromek GR05 CZT detector for 12 parts of the accelerator at PARTICLE. ^{22}Na, ^{54}Mn, ^{57}Co, ^{60}Co and ^{65}Zn are identified as common radioisotopes. This is in agreement with FLUKA simulations of the proton irradiation of conventional construction materials. Furthermore, it is observed that higher activities are produced in objects that are directly irradiated. Consequently, it takes longer for these objects to decay to activities below the appropriate clearance level for disposal.

In both case studies discussed in this thesis, the Kromek CZT detector presents itself as a suitable device to apply γ-spectroscopy in a medical context. Given its ability to operate at room temperature as well as its compact size and mobility, the detector can be used in remote locations.

Wetenschappelijke Samenvatting

In deze thesis worden twee onderzoeken gepresenteerd betreffende het gebruik van een compacte CZT-detector van γ-stralen (ontwikkeld door Kromek) in een medische context. Het doel is het potentieel van dit type detector te evalueren voor nucleaire toepassingen binnen de geneeskunde.

CZT-detectoren zijn een type halfgeleider detectoren gemaakt van $Cd_{0.9}Zn_{0.1}Te$. Omwille van de specifieke elektronische bandstructuur van dit materiaal ($E_g = 1.57\,\text{eV}$), kunnen CZT-detectoren gebruikt worden bij kamertemperatuur. Dit is een groot voordeel ten opzichte van bijvoorbeeld HPGe-detectoren, die gekoeld moeten worden om thermische excitatie te beperken. Bovendien zijn de CZT-detectoren van de Kromek GR familie – die in deze thesis bestudeerd worden – compact van vorm: zowel het detectie-kristal als de elektronica passen in een omhulsel van $2.5\,\text{cm} \times 2.5\,\text{cm} \times 6.3\,\text{cm}$. Hierdoor kunnen deze detectoren gebruikt worden in kleine ruimtes die minder toegankelijk zijn voor andere detectiesystemen. In beide casussen in deze thesis wordt de CZT-detector gebruikt voor γ-spectroscopie. Hierbij worden energie-spectra van bronnen die γ-stralen uitzenden, onderzocht om de aanwezige radioactieve isotopen te identificeren en te kwantificeren.

Het eerste onderzoek is gericht op het gebruik van een Kromek CZT-detector bij de productie van terbium isotopen voor medische toepassingen in CERN MEDICIS (Genève, CH). De familie van Tb-radionucliden is veelbelovend voor de nucleaire geneeskunde, omdat ze vier radio-isotopen bevat met complementaire verval-eigenschappen geschikt voor zowel beeldvorming als therapie. Het neutron-rijke radio-isotoop ^{161}Tb wordt reeds op grote schaal geproduceerd in SCK CEN (Mol, BE) via neutron-bestraling van Gd targets. De neutron-arme radio-isotopen ^{149}Tb, ^{152}Tb en ^{155}Tb worden voornamelijk gegenereerd in MEDICIS. In dit geval wordt een zwaar target zoals Gd of Ta bestraald met energetische protonen tot 1.4 GeV. Vervolgens worden de gegenereerde Tb radio-isotopen gescheiden van de andere via de ISOL (Isotope Separation On-Line) techniek. Tot slot worden de gewenste isotopen gecollecteerd op een implantatie plaatje. In MEDICIS wordt de geïmplanteerde activiteit tijdens de collectie opgevolgd met de Kromek GR1 CZT-detector. Deze is voor de collectie-kamer geïnstalleerd. In deze thesis worden de γ-spectra geanalyseerd die tijdens de ^{155}Tb collecties in 2021 zijn gemeten met de CZT-detector. Deze spectra wijzen op de aanwezigheid van $^{139}Ce^{16}O$ als isobare contaminant die samen met ^{155}Tb geïmplanteerd wordt. Tevens blijkt uit de analyses dat er (zelf-)sputtering plaatsvindt in de collectie-kamer. Dit beperkt de hoeveelheid ^{155}Tb die geïmplanteerd blijft op de implantatie folie. Ten slotte suggereren de γ-spectra – in overeenkomst met de metingen van de ionen-stroom – dat conditionering van het target voorafgaand aan de collectie voordelig is om te voorkomen dat de ionen-bron verzadigd raakt.

In het tweede onderzoek in deze thesis wordt een Kromek CZT-detector gebruikt in het kader van het beheer van radioactief afval in het protontherapie-centrum PARTICLE (Leuven, BE). Ten gevolge van directe bestraling door de protonen van 230 MeV of indirecte bestraling door verstrooide protonen worden er kernreacties geïnduceerd in het raamwerk van de straallijn. Afhankelijk van de samenstelling van het constructiemateriaal en de energie van de protonen, wordt een verscheidenheid van radio-isotopen geproduceerd. Zo ontstaat er radioactief afval. Om de gepaste behandeling van specifieke componenten te kunnen bepalen, dienen de gegenereerde radio-isotopen geïdentificeerd en gekwantificeerd te worden. In deze thesis is dit met behulp van een Kromek GR05 CZT-detector gerealiseerd voor 12 onderdelen van de deeltjesversneller in PARTICLE. ^{22}Na, ^{54}Mn, ^{57}Co, ^{60}Co en ^{65}Zn werden daarbij geïdentificeerd als meest voorkomende radio-isotopen. Dit komt overeen met FLUKA-simulaties van de proton-bestraling van conventionele constructiematerialen. Daarnaast werd vastgesteld dat hogere activiteiten van de radio-isotopen aanwezig waren in de objecten die direct bestraald werden. Bijgevolg duurt het langer vooraleer de activiteiten in deze objecten vervallen naar waardes beneden het niveau waarop ze vrijgegeven mogen worden.

In beide casussen die bestudeerd zijn in deze thesis, heeft de compacte Kromek CZT-detector zich bewezen als geschikt detectiesysteem om γ-spectroscopie mee toe te passen in een medische context. Dankzij de mogelijkheid om bij kamertemperatuur te werken, alsook de compacte vorm en mobiliteit van de detector, kan de Kromek CZT detector gebruikt worden in een verscheidenheid aan opstellingen, inclusief kleine ruimtes die minder toegankelijk zijn voor andere detectiesystemen.

Layman Summary

According to the World Health Organization, cancer is one of the leading causes of death worldwide. Therefore, there are multiple branches in medicine dedicated to cancer therapy as well as medical imaging to allow an early diagnosis. In this thesis, two specific branches are explored from a nuclear physics point of view.

The first branch that we consider, is nuclear medicine. In nuclear medicine, radioactive tracer molecules or "radiopharmaceuticals" are administered to the patient. These radiopharmaceuticals are designed to specifically target cancer cells. At the tumour site, they either enable diagnostic imaging or they exert a therapeutic effect and kill the cancer cells. For both cases, a minimum amount of radioactivity is required to achieve the desired effects. Therefore, it is important to establish large scale production of the radioactive material or "radioisotopes" for medical applications. In this thesis, the production of medical terbium (Tb) radioisotopes is investigated at CERN MEDICIS (Geneva, CH). To quantify the produced Tb activity, a technique called "gamma-spectroscopy" is applied. This technique relies on the detection of gamma-radiation to identify and quantify radioisotopes. For this purpose, a CZT detector manufactured by Kromek is used.

The second branch that is explored in this thesis, is hadrontherapy. Hadrontherapy is a form of radiation therapy where the patient is irradiated with heavy charged particles to kill the cancer cells while largely sparing healthy tissue. When the charged particles interact with surrounding construction materials, various radioisotopes are produced. Therefore, radioactive waste is generated after disassembly. There are many regulations that define how radioactive waste should be treated, in order to protect the public from the dangers of radioactivity. To decide on the appropriate treatment for a specific piece of waste, one needs to know which radioisotopes are present in the sample and at which respective activity levels. That can be investigated using the same technique as for monitoring the production of radioisotopes: gamma-spectroscopy. In this thesis, gamma-spectroscopy is performed on 12 radioactive construction materials from the proton therapy centre PARTICLE (Leuven, BE) to guide the waste management. The same type of detector is used as in the first case study, namely a Kromek CZT detector.

In both studies discussed in this thesis, the compact Kromek CZT detector presents itself as a suitable device to perform γ-spectroscopy in medical applications. Concerning production of medical Tb radioisotopes, the measurements allow to identify several factors that may improve the efficiency of the production. With respect to the radioactive waste from PARTICLE, it is possible to determine how long each piece must be held for decay-in-storage before it becomes safe to dispose of it.

Samenvatting voor een breed publiek

Volgens de Wereld Gezondheidsorganisatie vormt kanker wereldwijd één van de belangrijkste doodsoorzaken. Daarom zijn vele takken in de geneeskunde gewijd aan kankertherapie alsook aan medische beeldvorming met het oog op vroegtijdige diagnoses. Voor deze thesis wordt in twee van deze domeinen onderzoek verricht vanuit een kernfysisch standpunt.

Het eerste onderzoek betreft nucleaire geneeskunde. Bij nucleaire geneeskunde worden radioactieve tracer moleculen of "radiofarmaca" toegediend aan de patiënt. Deze radioactieve geneesmiddelen zijn ontworpen om zich specifiek te richten op kankercellen. Hierdoor wordt in het ene geval de tumor gemakkelijker en beter in beeld gebracht, in het andere geval hebben deze farmaca een therapeutisch effect door het doden van de kankercellen. In beide gevallen is er een minimale hoeveelheid van radioactiviteit nodig om het gewenste resultaat te bekomen. Daarom is het belangrijk om op grote schaal radioactief materiaal of "radio-isotopen" te produceren geschikt voor medische toepassingen. In deze thesis wordt de productie van terbium (Tb) radio-isotopen voor medisch gebruik onderzocht in CERN MEDICIS (Genève, CH). Om de opgewekte Tb-activiteit te meten, wordt de techniek van "gamma-spectroscopie" toegepast. Deze techniek is gebaseerd op de detectie van gammastralen om radio-isotopen te identificeren en te kwantificeren. Hiervoor wordt een CZT-detector gebruikt die ontwikkeld is door de firma Kromek.

Hetzelfde type detector wordt ingezet in het medische domein "hadrontherapie". Hadrontherapie is een soort bestralingstherapie waarbij de patiënt bestraald wordt met zware, geladen deeltjes om de kankercellen te bestrijden zonder veel schade aan gezonde weefsels. Wanneer deze deeltjes in aanraking komen met de materialen van de bestralingsapparaten, worden verschillende radio-isotopen geproduceerd. Dit leidt tot radioactief afval bij de ontmanteling van de apparatuur. Ter bescherming tegen de gevaren van radioactiviteit zijn er veel voorschriften die definiëren hoe radioactief afval dient behandeld te worden. Om de gepaste behandeling voor een specifiek stuk afval te bepalen, moet geweten zijn welke radio-isotopen zich daarin bevinden en met welk activiteitsniveau. Dat kan opnieuw onderzocht worden met gamma-spectroscopie. In deze thesis gebeurt dit met een Kromek CZT-detector op 12 stalen van het protontherapie-centrum PARTICLE (Leuven, BE).

In beide studies toont de Kromek CZT-detector zich als een apparaat dat geschikt is voor het uitvoeren van gamma-spectroscopie in medische toepassingen. Bij de productie van medische Tb radio-isotopen wijzen de metingen op verschillende factoren die de efficiëntie van de productie kunnen verhogen. In het kader van het radioactieve afvalverwerking, kan met de detector bepaald worden hoe lang elk stuk moet bewaard worden in een veilige ruimte voor "vervalstockage" vooraleer het vrijgegeven mag worden.

Introduction

Introduction

Since its discovery in 1896 by Henri Becquerel, radioactivity has always been a controversial topic of conversation. On one hand, it is praised for its potential in medical applications. On the other, the biological effects of ionising radiation on the human body are also a cause for concern – especially after the nuclear accidents in the last century. As with anything, it is the dose that makes the poison. Therefore, it is very important to be able to quantify radioactivity in given samples. Over the years, various detectors have been developed to measure the different types of radiation emitted by radioactive sources. In this thesis we focus on one particular type, namely a compact CZT detector manufactured by Kromek.

Two case studies for the use of a compact CZT detector in a medical context are presented in this thesis. The aim is to evaluate the potential of this type of detector for nuclear applications in medicine. In the first case study, the production of terbium radioisotopes for medical applications at CERN MEDICIS (Geneva, CH) is investigated. The second case study addresses the issue of radioactive waste management in the proton therapy facility PARTICLE (Leuven, BE).

To structure the discussion, this thesis is divided into three parts. Part I presents all the necessary background information on radioactive decay and explains how the CZT detector is used to identify and quantify radioisotopes in a sample. Part II is devoted to the use of the CZT detector for the production of Tb for medical applications at MEDICIS. In this part, first the MEDICIS facility and its working are described in chapter 3, followed by an analysis of the Tb collections that were performed in 2021 in chapter 4. The case study for the use of the compact Kromek CZT detector in the context of waste management at PARTICLE is discussed in part III. This part consists of three chapters. Chapter 5 explains the general topic of waste production in hadrontherapy; chapter 6 presents a series of simulations to numerically predict which radioisotopes are produced; and chapter 7 gives the analysis of an experimental study of radioactive waste materials from PARTICLE using the CZT detector. Finally, part IV provides a conclusion on the use of compact CZT detectors for nuclear applications in medicine.

Part I

Gamma-ray Spectrometry

Chapter 1

Production of Radioactivity

This chapter provides some background information on relevant concepts for the rest of this thesis. First, the notions of radioactivity and radioactive decay are reviewed. This is followed by a more detailed treatment of radioactivity as produced by proton-induced nuclear reactions. In that light, the simulation software FLUKA is introduced at the end of this chapter, which can be used to predict the outcome of diverse nuclear reactions.

1.1 Basics of Nuclear Physics

1.1.1 Radioactivity

The vast majority of all known nuclei are unstable. This is illustrated by the nuclear chart in Fig. 1.1. Atomic nuclei consist of protons and neutrons held together by the strong nuclear force. At short distances, the nuclear force is stronger than the Coulomb force, such that it can overcome the Coulomb repulsion between the positively charged protons and they bind to form a nucleus. However, the more protons a nucleus contains, the more neutrons are required to maintain the right balance between the increasing Coulomb repulsion and the nuclear force [2]. Therefore, there is an optimal neutron-to-proton ratio (N/Z), which on average increases for increasing atomic number Z. If a nucleus has too few or too many neutrons in this regard, or it simply becomes too large in size, then it is unstable and it will convert to a lower energy configuration by various modes of decay (see next section).

Radioactive decay is a stochastic process. One cannot predict precisely when a nucleus will decay; rather, each radioisotope is characterised by a certain probability to decay within a time interval dt. This probability is governed by the isotope-specific decay constant λ [s^{-1}]. The rate of decay, also known as the activity A [Bq], can then be written as

$$A \equiv -\frac{dN(t)}{dt} = \lambda N(t), \tag{1.1}$$

where $N(t)$ denotes the number of nuclei [2]. This integrates to the well-known exponential law of radioactive decay

$$N(t) = N_0 e^{-\lambda t}. \tag{1.2}$$

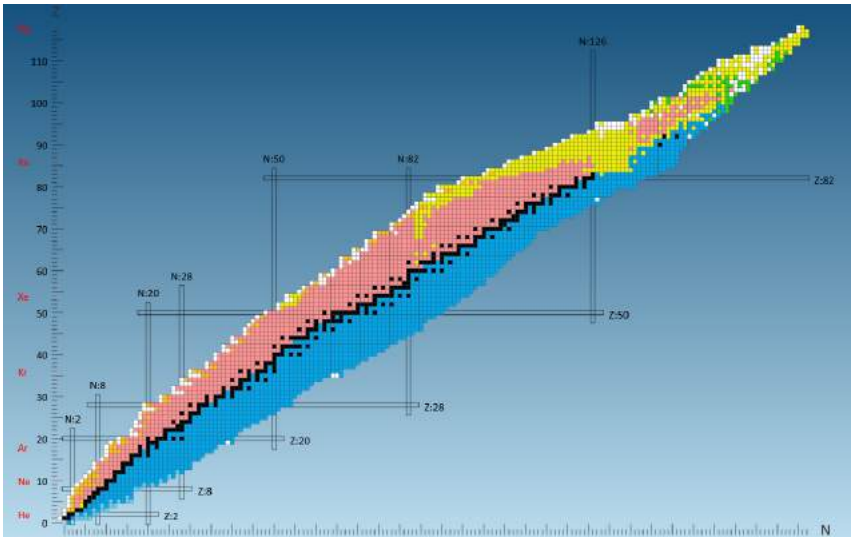

Figure 1.1: Nuclear landscape [3]. The black squares indicate stable isotopes, whereas all other colours indicate unstable nuclei according to their main mode of decay.

A similar relation holds for the activity $A(t)$. The time after which half of the nuclei have decayed is called the half-life $T_{1/2}$. From the above expression it can be calculated to be

$$T_{1/2} = \frac{\ln 2}{\lambda}. \tag{1.3}$$

Aside from the type and energy of the emitted radiation, the half-life is a very important characteristic of any radioisotope. It determines how long the isotope remains present in significant amounts after its production. This plays a crucial role in medical applications (where a minimum activity is required to exert the effects for imaging or therapy) as well as waste management (where the half-life determines how long radioactive waste must be stored before it becomes safe to be disposed of or recycled). In parts II and III of this thesis, respectively, these two cases are further illustrated.

1.1.2 Types of Radioactive Decay

There are three primary decay modes for radioactive nuclei: α, β and γ-decay. In α-decay, the radioactive nucleus emits a ${}^4_2\mathrm{He}$ nucleus (α-particle) to transmute into a lighter, more stable configuration:

$${}^A_Z\mathrm{X} \rightarrow {}^{A-4}_{Z-2}\mathrm{Y} + {}^4_2\mathrm{He}. \tag{1.4}$$

The kinetic energy of the emitted α-particle, typically ranging between 4 MeV and 6 MeV, is fixed for a given transition [4]. As the spontaneous emission of an α-particle is a Coulomb repulsion effect [2], this decay mode becomes increasingly important for heavy nuclei. For lighter nuclei, β-decay is much more often encountered. This decay type is itself still divided in two types, namely β^-- and β^+-decay. In the former, a neutron from the nucleus is converted into a proton, thereby emitting an electron (β^--particle) and an anti-neutrino:

$${}^A_Z\mathrm{X} \rightarrow {}^A_{Z+1}\mathrm{Y} + e^- + \overline{\nu_e}. \tag{1.5}$$

This is generally the preferred decay mode for radioisotopes with an excess number of neutrons. Since there are three particles at the end of the reaction, the electron does not

have a well-defined energy (as did the α-particle in the previous case), but a continuous distribution of energies, from zero up to the "endpoint energy". The upper limit to the energy is equal to the energy difference between the initial and final states of the decay process [2]. The same holds for the β^+-particle emitted in β^+-decay. In that case, a proton is converted into a neutron, thereby emitting a positron (β^+-particle) and a neutrino:

$$ {}^{A}_{Z}\mathrm{X} \rightarrow {}\ {}^{A}_{Z-1}\mathrm{Y} + e^+ + \nu_e. \tag{1.6} $$

This decay mode is encountered for radioisotopes with an excess number of protons. In matter, the positron will annihilate with a nearby electron as soon as it has slowed down sufficiently. This generates two photons with energy equal to the rest-mass of an electron (511 keV) at approximately 180° to each other. This process characteristically follows any β^+-decay. A competing process for β^+-decay is so-called electron capture (often indicated by EC or ε) [2]. Here, an orbital electron of the atom is absorbed by the nucleus and reacts with one of the protons, producing a neutron and a neutrino. As this results in a vacancy in one of the inner atomic orbitals, electron capture is always followed by the emission of characteristic X-rays of the atom.

After any of the aforementioned decay modes, the daughter nucleus is often left in an excited state. In most cases, it subsequently rapidly decays towards the ground state by emitting one or more photons via γ-decay:

$$ {}^{A}_{Z}\mathrm{X}^* \rightarrow {}\ {}^{A}_{Z}\mathrm{X} + {}^{0}_{0}\,\gamma. \tag{1.7} $$

Each photon has an energy equal to the energy difference between the initial and final states of the transition in question. For nuclear states, these differences are in the keV to MeV range. A process that often competes with γ-decay is internal conversion. The nucleus then de-excites by transferring its energy directly to an atomic electron, which consequently gets ejected from its orbital. The kinetic energy of the emitted electron is equal to the transition energy less the binding energy of the electron in the atom [2]. Similar to the case of electron capture, a vacancy is left in one of the atomic orbitals after this decay, leading to the emission of characteristic X-rays.

Most radioisotopes do not decay via a single predestined process, rather they have multiple competing decay modes. Each channel is then characterised by a certain probability, which is expressed by the "branching ratio" [2]. This is defined as the number of nuclei that decay by that specific channel with respect to the total number of nuclei that decay. Similarly, not every decay leaves the resulting daughter nucleus in the same state, resulting in probabilities of emitting certain energies of γ's, often referred to as intensities.

1.2 Nuclear Reactions

Only a limited number of radionuclides occur in nature, namely the very long-lived or "primordial" isotopes and isotopes produced in their decay or in interactions of background radiation with the environment. All other radioisotopes are produced artificially via a variety of nuclear reactions. The case studies presented in parts II and III of this thesis both deal with radioisotopes produced by interactions of protons with a stationary target: for the production of terbium isotopes for medical applications at CERN MEDICIS

(part II), a proton beam of 1.4 GeV is directed onto a tantalum target, and in the considerations on waste management in the PARTICLE facility (part III), radioactive isotopes are produced by interactions of a proton beam of 230 MeV with surrounding construction materials. Therefore, the first part of this section gives an overview of the principal concepts of proton-induced nuclear reactions. The second part introduces the software FLUKA, which allows to simulate nuclear reactions to predict and investigate their effects.

1.2.1 Proton-Induced Nuclear Reactions

Protons always require a minimum energy to be able to interact with nuclei in a stationary target. The reason for this is that protons are positively charged, so they need to overcome Coulomb repulsion in order to come close enough to a nucleus for interaction. The Coulomb barrier thus determines a threshold energy for proton-induced nuclear reactions. As the energy of the protons rises above this threshold, more and more reaction channels are opened [5]. For energies of the order 5 MeV to 15 MeV, (p, n) and (p, α) reactions prevail. At energies of several 10s MeV, $(p, 2n)$, $(p, 2p)$, $(p, 3n)$ and so forth become possible as well. Finally, for 100 MeV and more, high-energy nuclear reactions start to occur [5].

Reactions induced by high-energy protons are commonly divided into four categories: spallation, fission, fragmentation, and fusion-evaporation [7, 8]. Spallation is the emission of a large number of nucleons from the target nucleus after irradiation. This happens in a two-step process. First, the proton interacts via a sequence of nucleon-nucleon collisions inside the target nucleus. This is referred to as the "intra-nuclear cascade". During this stage, some nucleons escape from the target nucleus as secondary particles, leading to

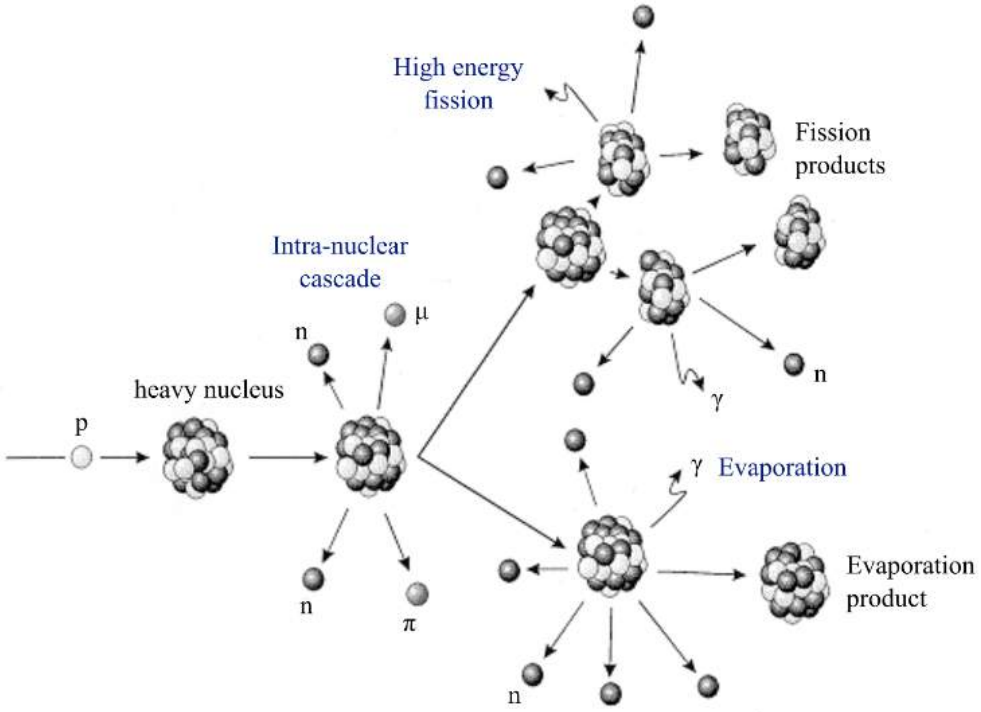

Figure 1.2: Schematic representation of proton-induced fission and spallation reactions. Ref. [6].

"pre-equilibrium emission" [9]. In the next step, the remaining nucleus (also called "pre-fragment") de-excites via nucleon or cluster evaporation and subsequent γ-decay [9, 10]. The higher the energy of the incident protons, the larger the variety of product nuclei generated in this process. In particular, for energies on the order of GeV, virtually all nuclei lighter than the target nucleus itself can be produced [5, 11]. The spallation mechanism is illustrated in the bottom part of Fig. 1.2. As shown in the top part of that figure, for very heavy targets fission competes with the second step of the spallation process. In this case, the compound nucleus formed after proton irradiation divides into two lighter fragments of comparable mass. These fission fragments are neutron-rich isotopes with mass numbers ranging from 50 to 170 [11] and maintain the N/Z ratio of the target nucleus. The third reaction that can occur with high-energy protons is fragmentation. Here, small fragments are violently split off from the target nucleus, resulting in a large variety of isotopes. Besides isotopes close to the initial nucleus, very light nuclei are produced in this reaction mechanism [7, 8]. Finally, proton-induced fusion-evaporation generates neutron-deficient isotopes close to the line of stability via fusion of the proton with the target nucleus, followed by evaporation of α-particles, protons and neutrons [7]. This process differs from all the above in the sense that fusion-evaporation reactions are selective. The isotopes that are generated depend on the decay characteristics and the competition between different decay channels of the compound nucleus [7, 11]. The probability for any reaction channel is expressed by the "cross section" (σ) [b = 10^{-28} m^2]. This depends on a number of factors, including the energy of the incident proton. Hence, for different energies different reactions may be more likely to occur, producing different isotopes.

By way of example, Fig. 1.3 shows the energy dependence of the cross section for $^{27}_{13}$Al (p, X) $^{22}_{11}$Na reactions. There is a threshold energy below which the reaction does not take place ($\sigma \approx 0$). This is the Coulomb barrier plus some additional threshold

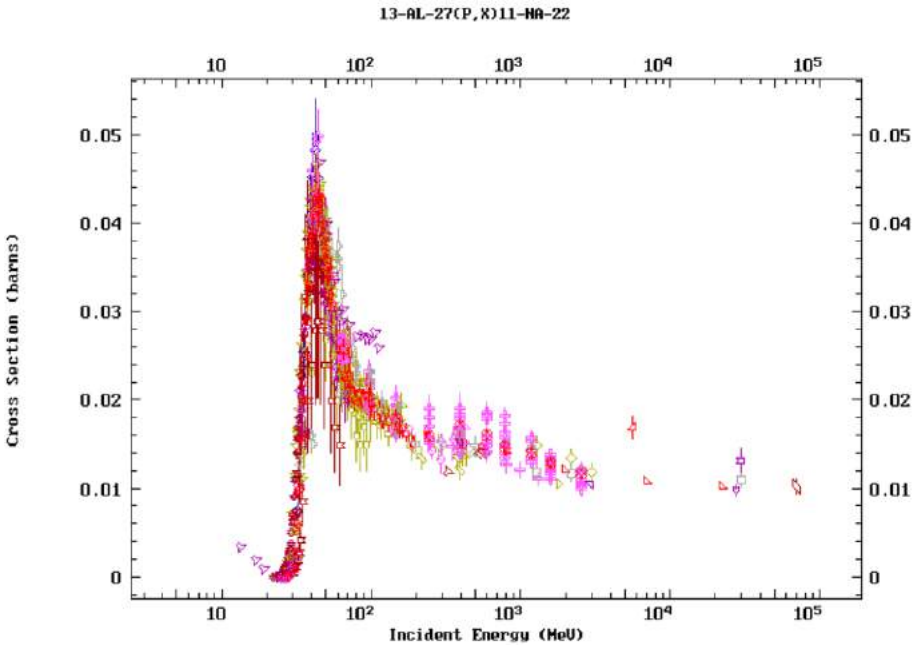

Figure 1.3: Measured cross sections of proton-induced reactions of the type $^{27}_{13}$Al (p, X) $^{22}_{11}$Na. *Data from Ref. [12].*

depending on the particles that are emitted. For energies above the threshold the cross section rapidly rises to a maximum, which is reached around 40-50 MeV. Afterwards, it declines again to a lower, yet non-zero value. The peak exhibited in the cross section is quite sharp, meaning that the proton-induced reaction from $^{27}_{13}$Al to $^{22}_{11}$Na only has high probability to occur in a limited energy range. Nevertheless, the probability is non-zero at higher energies. In this region, whether the reaction will take place depends on the relative probabilities of other proton-induced reaction channels on $^{27}_{13}$Al.

From the above considerations, we note that the energy of the incident proton plays a crucial role in determining which nuclear reactions will occur in the target material. Not only does it control which types of reactions are energetically allowed, it also influences the relative probabilities of the different reaction channels. This complicates matters when one takes into account that protons lose energy in any finite-sized target material. A range of proton energies must thus always be considered, with different cross sections for each energy. This integral process quickly becomes too hard to solve analytically. Hence, one must turn to numerical simulations to predict which reactions will occur and which isotopes they will produce. In this thesis, the FLUKA software is used for this purpose.

1.2.2 FLUKA Simulation Software

FLUKA (FLUktuierende KAskade) is a Monte Carlo code for multi-particle transport, developed jointly by the European Laboratory for Particle Physics (CERN) and the Italian Institute for Nuclear Physics (INFN) [13, 14]. It is the workhorse behind all beam-accelerator calculations at CERN and is also routinely used in applications concerning energy deposition, radiation damage, shielding activation and design, target design, dosimetry, waste disposal etc. [14].

In Monte Carlo methods, random numbers are used to solve a wide class of problems [15]. Regarding interactions of ionising radiation with matter, Monte Carlo simulations can predict the average outcome of the interactions by randomly sampling them. For this purpose, an interaction model must be implemented for the incoming particles in the medium. This is provided in the form of a database of differential cross sections for all possible interaction mechanisms. The cross sections determine the probability density functions (pdf's) of energy, position, direction and time of production of the particle after interaction, which in turn fully determine the particle track [15, 16]. By randomly sampling these pdf's, the energy loss and change of direction of the particle as well as the production of secondary particles are sampled. The Monte Carlo simulation is performed for a predefined number of primary particle tracks. The more primary particles (also called "primaries") are simulated, the smaller the statistical uncertainty on the results will be, but also the longer the computing time [15]. In practice, one must always look for the right compromise between these two effects. Per primary particle, the transport and interactions are simulated step-wise. At each step, all possible interactions between the particle and the medium are randomly sampled according to their relative probabilities. When the particle is fully stopped in the medium or has reached the boundaries of the geometry, the code starts the simulation of a new primary. This process is repeated until the user-defined number of primaries is reached.

FLUKA can simulate the interaction and propagation in matter of about 60 different particles over energy ranges from a few keV to several TeV [13]. Microscopic models are adopted whenever possible, ensuring consistency among all reaction steps. Furthermore, FLUKA enforces conservation laws in each step of the simulation and checks results against experimental data at single interaction level. This greatly enhances the accuracy and predictive power of the simulations. In addition, FLUKA's algorithm provides a robust independence of results from the step length in the individual particle track simulations [13]. This presents a major improvement compared to early Monte Carlo codes.

A convenient interface for FLUKA is provided by "Flair". This is a very user-friendly software, so for most applications no programming skills are required. To define the input for a simulation, Flair holds an extensive set of "cards". These allow to enter the necessary information (type of particles, beam energy, duration of the irradiation etc.) in a clear and structured way. Another useful feature of Flair is its graphical interface for the geometry defined in the input cards. Complex geometries can be generated in FLUKA by means of combinatorial geometry [13], meaning that complex shapes are created by adding and subtracting simpler shapes. The graphical interface in Flair allows to visualise the defined geometry and readily debug it, if necessary. Besides input cards, Flair also contains output cards that can be used to define which physical quantities should be scored in the simulation. One of the outputs that FLUKA can provide is the activity of all the isotopes produced in the medium (per unit volume). The scored quantities are evaluated after predetermined decay times given in the input. This allows, for example, to follow the time evolution of radioactivity created in the medium after various cooling times. The obtained data after the simulation can either be directly processed and plotted in Flair or extracted for further analysis with other software programs.

In this thesis, FLUKA is used to simulate the irradiation processes discussed in parts II and III, to determine which radionuclides are produced in them and what their activities are. The outcomes are then compared to the results of the respective γ-spectrometry analyses. How the latter are performed is explained in the next chapter.

Chapter 2

Gamma-spectrometry with a CZT Detector

The study of decay characteristics of radioisotopes is a very useful way to gain information about nuclear structure and the properties of nuclear excited states. A variety of techniques have been developed for α, β and γ-decay spectroscopy, most of which are complementary. Nevertheless, γ-spectroscopy is considered to be the primary means to investigate the structure of excited states. That has to do with the relative ease of γ-ray detection compared to α and β-particles, as well as the available high-resolution and high-precision techniques [2].

In this thesis, γ-spectroscopy is applied for the purpose of identifying and quantifying the presence of radioisotopes in a sample. The identification relies on the fact that the γ-spectrum of a nucleus serves as a unique fingerprint of that nucleus. Quantification, on the other hand, is possible by observing the intensities of the emitted γ-rays in addition to their energies. In this chapter, first the different interactions of γ-rays with matter and their respective effects on acquired γ-spectra are reviewed. Then, the working of the type of detector used for this thesis (i.e. CZT detectors) is explained, and finally, the methodology for analysis of the γ-spectra is presented.

2.1 Interactions of γ-rays with Matter

The three main mechanisms of interaction of γ-rays with matter are the photoelectric effect, Compton scattering and pair production [4]. Their relative importance depends on both the energy of the γ's and the atomic number of the material with which they interact, as portrayed in Fig. 2.1.

Photoelectric Effect Via the photoelectric effect, the incoming photon gives all its energy to an atomic electron in the absorbing material, which is thereby ejected from its orbital. The electron acquires a kinetic energy of $E_\gamma - B_{e^-}$ with E_γ the energy of the incoming γ-ray and B_{e^-} the binding energy of the electron in its bound orbital [4]. The

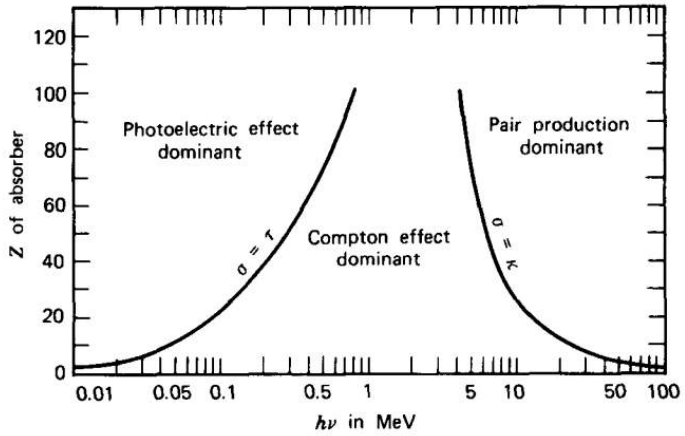

Figure 2.1: Regions of dominance of the three most relevant γ-ray interactions as function of the energy $E = h\nu$ of the radiation and the atomic number Z of the absorbing material. The curves indicate the values of $h\nu$ and Z for which two neighbouring effects are equally important. Picture from Ref. [4].

atom is ionised and left in an excited state. It decays back to the ground state by emitting characteristic X-rays.

Compton Scattering In Compton scattering, the photon is scattered by an electron in the absorbing material. The photon is deflected by an angle θ and part of its energy is transferred to the electron. The relation between the energy of the scattered photon and the scattering angle θ is given by

$$E'_\gamma = \frac{E_\gamma}{1 + \frac{E_\gamma}{m_0 c^2}(1 - \cos\theta)}, \tag{2.1}$$

where E_γ and E'_γ represent the initial and final energy of the photon, respectively, and $m_0 c^2 = 511\,\text{keV}$ is the rest-mass of the electron [4]. The most energy is transferred to the electron for $\theta = 180°$. The residual energy of the scattered photon is then

$$E'_{\gamma,\text{min}} = \frac{E_\gamma}{1 + 2\frac{E_\gamma}{m_0 c^2}}. \tag{2.2}$$

Pair Production If the incoming photon has an energy above 1.022 MeV (twice the rest-mass of an electron), it can also interact with matter via pair production. In this case, a electron-positron pair is generated and the photon disappears in the process. Any excess energy above 1.022 MeV of the incoming photon is carried away by the positron and electron as kinetic energy [4]. After the positron has slowed down in the absorbing material, it annihilates with a nearby electron, leading to the emission of two 511 keV photons at an angle of approximately 180°. The deviation of this angle originates from the residual momentum of the positron.

2.2 Features of γ-spectra

As a photon transfers all its energy to the detector material in a single step by a photoelectric interaction, this is the preferred interaction in any γ-ray detector [4]. It leads to a peak in the γ-spectrum centred around the energy of the incident photon. From Fig. 2.1 it can be seen that for γ-rays with energies in the keV to MeV range (stemming from nuclear transitions, see section 1.1.2), the photoelectric effect is the dominant interaction mechanism only for high Z materials. Therefore, detectors for γ-spectroscopy are as a rule manufactured from materials that incorporate elements with high atomic numbers [4]. Nevertheless, the other interaction types can never be fully eliminated and this has significant effects on the acquired spectrum.

Firstly, if an incoming photon interacts via Compton scattering in the detector, only part of its energy is transferred. If many successive Compton interactions occur, the photon may eventually lose all of its initial energy to electrons of the detector material. However, due to the finite size of detectors, the scattered photon usually leaves the active detection volume before this happens. As a result, a lower energy than the initial incoming energy is recorded by the detector. The maximal energy transfer takes place at scattering angle $\theta = 180°$, in which case the energy of the scattered photon is given by Eq 2.2. Since all scattering angles can occur in the detector, there is a continuum of values for the transferred energy, ranging from zero up to the "Compton edge" determined by $E_\gamma - E'_{\gamma,\min}$ [4].

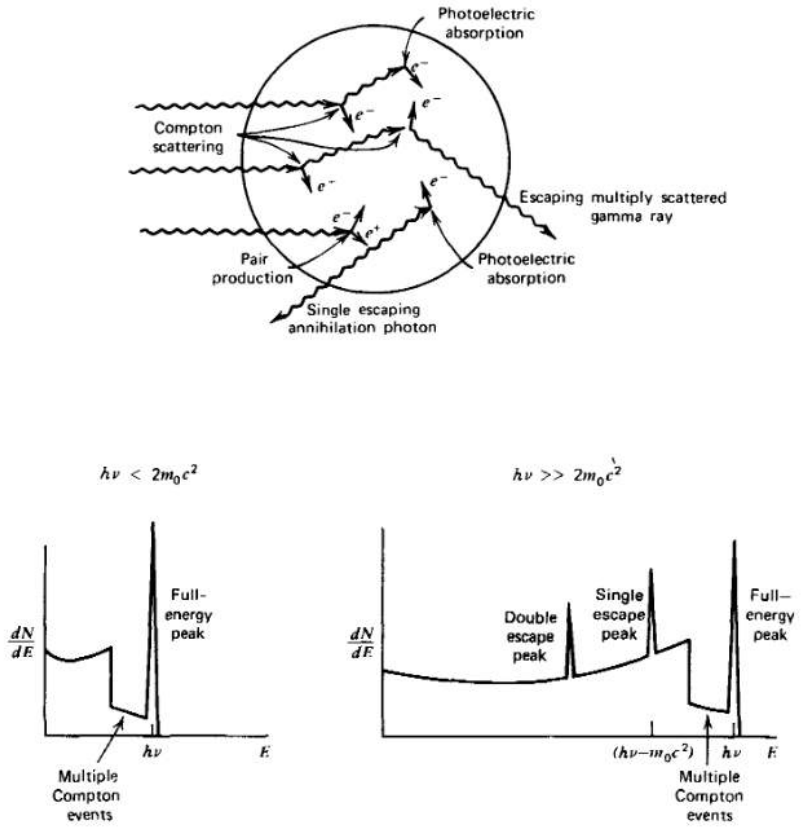

Figure 2.2: Effects of Compton scattering and pair production in a finite size detector on the acquired γ-spectrum. Picture from Ref. [4].

Hence, in the spectrum this continuum appears as a broad band left of the photo-peak, called the "Compton continuum". This is illustrated in Fig. 2.2.

If the energy of the incoming photon is larger than 1.022 MeV, pair production becomes a possible interaction mode as well. In this case, the two 511 keV photons generated after annihilation of the positron could carry part of the initial energy back out of the detection volume. If both photons escape, this leads to an additional peak in the spectrum at energy $E_\gamma - 1.022\,\text{MeV}$. This peak is then referred to as the "double escape peak". If only one of the annihilation photons escapes the detection volume, one gets analogously a peak at $E_\gamma - 511\,\text{keV}$, called the "single escape peak" [4]. Both features are shown in Fig. 2.2

Besides undesired interactions within the detector, also interactions of γ-rays with any materials surrounding the detector have an impact on the final spectrum. If photoelectric absorption occurs in the surrounding material, the subsequent characteristic X-rays of the material can enter the detection volume and lead to an additional peak in the γ-spectrum. Secondly, Compton scattering in the surrounding gives rise to a broad peak around 200-250 keV, called the "backscatter peak" [4]. This peak originates from photons that are scattered over large angles. It can be shown from Eq. 2.1 that the energy of the scattered photon is nearly identical for all scattering angles above 110°-120°, so the energy of the backscatter peak corresponds roughly to that of a photon scattered over $\theta = 180°$ given in Eq. 2.2. In the limiting case that the initial energy of the γ-ray is much larger than

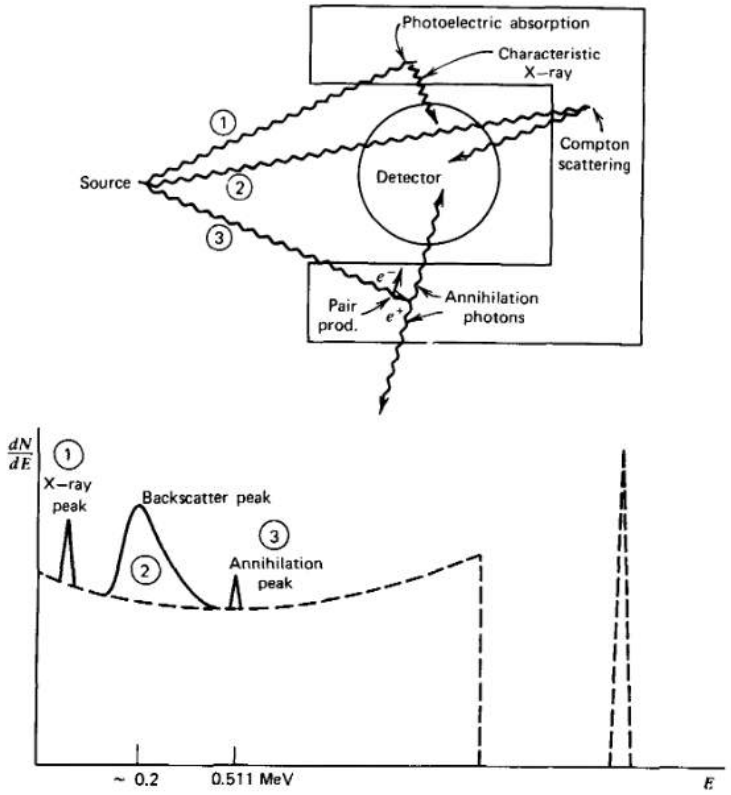

Figure 2.3: Schematic representation of the possible interactions within the surrounding material, together with the respective effects on the γ-spectrum. Picture from Ref. [4].

1.022 MeV, this reduces to

$$E'_\gamma(\theta = 180°) \approx \frac{m_0 c^2}{2} \approx 250\,\text{keV}. \tag{2.3}$$

So, the backscatter peak will always appear at an energy of maximally 250 keV [4]. Lastly, if the initial γ-ray interacts via pair production in the surrounding material, one of the generated annihilation photons can be detected. This leads to an annihilation peak at 511 keV. All of these effects are illustrated in Fig. 2.3.

From the above considerations, we note that there are many additional features that can appear in a γ-spectrum. Naturally, it is important to be aware of them and to take the different effects properly into account during analysis.

2.3 CZT Detectors

Over the years, many different detectors have been developed for γ-ray detection. The three main types are gas-filled detectors, scintillators, and solid-state or semiconductor detectors. The detection mechanism is different for each type. Scintillators first convert the incoming radiation into visible light, which is subsequently detected. In gas-filled detectors, γ-rays are detected by the ionisation of the gas molecules. Lastly, in semiconductor detectors they are detected by the creation of electron-hole pairs [4]. For this thesis, a particular type of semiconductor detector is considered, namely a cadmium zinc telluride ($Cd_{1-x}Zn_xTe$ or CZT) detector with Zn concentrations in the range $x = 0.1 - 0.2$ [17, 18].

2.3.1 Working Principle

The operation of semiconductor detectors relies on the band structure for electron energies in solids. Due to collective interactions of the atoms in a crystal lattice, solids exhibit energy bands rather than discrete energy levels as in free atoms [2]. The highest occupied band and lowest unoccupied band at absolute zero temperature are called the valence band and conduction band respectively. They are shown in Fig. 2.4 for a conductor, semiconductor and insulator. The valence band corresponds to outer-shell electrons that are bound to a specific site in the lattice, whereas the conduction band corresponds to electrons that are allowed to migrate through the crystal and thus contribute to electrical conductivity. For metals, the valence and conduction band overlap, explaining their high conductance. In contrast, in semiconductors and insulators, both bands are separated by a range of forbidden energies, called the bandgap. The difference between an insulator and a semiconductor is the size of this gap (E_g) [2]. For insulators it is usually 5 eV or more, whereas for semiconductors it is of the order of only 1 eV [2, 4].

Electrons can be excited from the valence band to the conduction band, if sufficient energy is provided to cross the bandgap. Physically, this corresponds to the excitation of the electron from its specific bonding site, such that it can move freely throughout the crystal [4]. In the valence band, a positively charged hole is left behind, which can also migrate in the crystal. The pair is referred to as an electron-hole (e-h) pair. When an electric field is applied over the semiconductor by two electrodes, the electron and hole are attracted to the anode and cathode, respectively. This is what happens in a

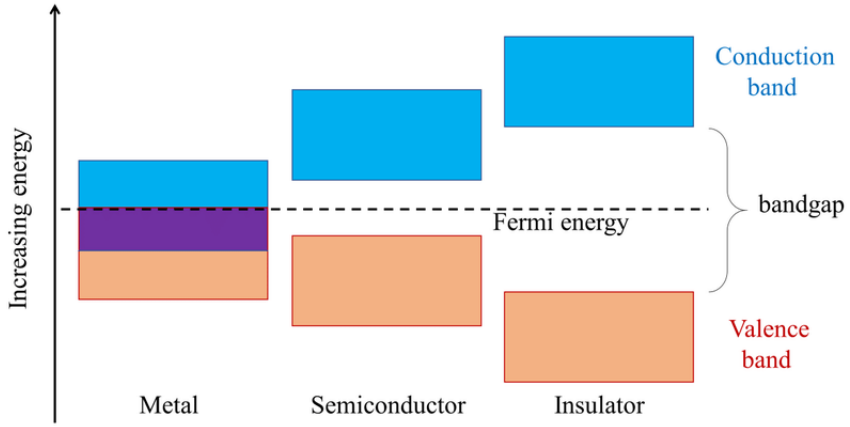

Figure 2.4: Band structure for a conductor (metal), semiconductor and insulator. Ref. [19].

semiconductor detector: the incoming radiation releases its energy in the semiconductor and produces many e-h pairs, which are subsequently collected at electrodes to generate a measurable current that can be read out by electronics. The number of e-h pairs created by an incoming photon of energy E_γ depends on the average energy required to produce one e-h pair. This quantity is called the "ionisation energy" ϵ and is largely independent of the energy and type of the incoming radiation [4]. That allows to write the number n_{e-h} of produced e-h pairs as

$$n_{e-h} = \frac{E_\gamma}{\epsilon}. \tag{2.4}$$

Hence, the current collected at the electrodes is proportional to the energy of the detected radiation. As a result of this linear relation, energy spectra can be acquired.

2.3.2 Advantages

The ionisation energy ϵ for semiconductor detectors is typically below 5 eV thanks to the small size of the bandgap [17]. Compared to the energies of the order of 30 eV and 100 eV needed to create the respective charge carriers in gas-filled detectors and scintillators [4], this is a major improvement. It implies a much larger number of charge carriers is generated in a semiconductor detector for an incoming γ-ray of the same energy. Consequently, the statistical fluctuation on the number of carriers per pulse ($\propto \sqrt{n_{e-h}}$) is reduced significantly, allowing a better energy resolution [4].

For CZT detectors with composition $Cd_{0.9}Zn_{0.1}Te$, the band gap equals 1.57 eV [18]. This is considerably higher than the values for silicon (1.11 eV) and germanium (0.66 eV) [20], which are very often used as semiconductor detectors. Analogously to the argument above, this means that the energy resolution is poorer in CZT detectors compared to Si and Ge detectors. Nevertheless, there is a major advantage to the increased bandgap, namely that CZT detectors can operate at room temperature. That has to do with the fact that e-h pairs are also thermally generated in semiconductors. The probability for this to occur is

$$p(T) = MT^{3/2} \exp\big(-\frac{E_g}{2k_BT}\big), \tag{2.5}$$

where T is the absolute temperature in Kelvin, k_B represents the Boltzmann constant, and M is some proportionality constant characteristic of the material [4]. Given the very small bandgaps (E_g) for Si and Ge, these detectors need to be cooled in order to suppress leakage current due to thermal e-h pairs. The larger bandgap in $Cd_{0.9}Zn_{0.1}Te$ makes this unnecessary. Therefore, CZT detectors effectively fill the gap between lower resolution gas-filled and scintillation detectors on one hand, and high-resolution but high maintenance Si and Ge solid-state detectors on the other [21].

Other benefits of CZT detectors include their high count rate capability, high collection efficiency, small dimensions, high density, and high effective Z [21]. Regarding the last of these, the high atomic numbers of cadmium ($Z = 48$), zinc ($Z = 30$) and tellurium ($Z = 52$) implicate that these materials have higher photon absorption efficiencies than silicon ($Z = 14$) and germanium ($Z = 32$), according to Fig. 2.1. Overall, the combination of properties described in this section – and, in particular, the combination of high resolution, high count rate capability and the ability to work at room temperature – makes CZT detectors very promising for medical and industrial applications [21].

2.3.3 The Kromek GR Family

One of the major suppliers of CZT detectors is the Kromek Group [21]. They manufacture a large variety of devices, each with its own applications. In this thesis, two detectors of Kromek's GR family for high-performance γ-spectrometry are studied: the GR1 and GR05 detectors. The difference between them lies in the size of the detection crystal. For the GR1 detector, it is $1\,\text{cm} \times 1\,\text{cm} \times 1\,\text{cm}$, whereas the GR05 has an even smaller crystal of $0.5\,\text{cm} \times 0.5\,\text{cm} \times 0.5\,\text{cm}$ [21]. Other detector characteristics are largely the same. For example, the energy range that can be detected is 30 keV to 3.0 MeV and the maximum throughput is 30 000 counts/s [21]. In both cases, the detector crystal is enclosed in a $2.5\,\text{cm} \times 2.5\,\text{cm} \times 6.3\,\text{cm}$ casing, together with all the read-out electronics [21]. The system is thus completely self-contained, and the output of digitised pulse heights is directly sent to a computer via a USB cable. This is illustrated in Fig. 2.5. The USB connection also serves as a power supply for the device, so no external power supply is needed. Together

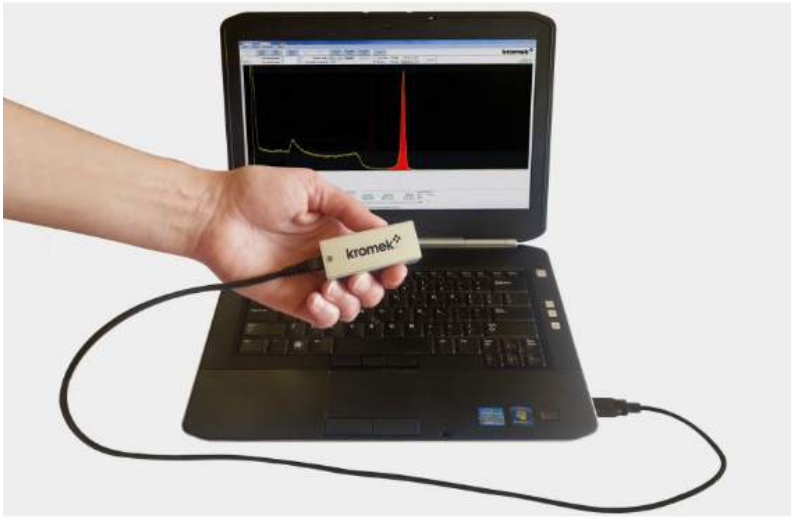

Figure 2.5: Kromek's GR05 detector together with the KSpect acquisition software [21].

with the small size of the detectors, this allows them to be used in remote places that might be inaccessible to other detection systems.

The data from the detectors are read out by Kromek's acquisition software KSpect. The software performs spectral acquisition, display, detector calibration and storage functions [21]. The obtained spectra can be saved and exported for further analysis. The detector calibration data can be saved in KSpect as well, and it can be associated with a particular detector by its serial number [21]. Finally, KSpect allows some basic analysis to be performed, such as defining regions of interest and fitting peaks to determine peak energies and count rates.

2.4 Methodology for Analysis

Parts II and III of this thesis present two case studies where a Kromek GR detector is used for γ-spectrometry in a medical context. In this section, the methodology that is used for the analysis of the obtained spectra is described.

2.4.1 Peak Assignment

The peaks in the γ-spectra are assigned with the help of InterSpec. This is a spectral radiation analysis software by Sandia National Laboratories (SNL) [22]. It can read data files from most common spectral radiation detectors, including the Kromek CZT family. After the energy calibration is applied (which defines the relationship between the detector's channel numbers and the energy of the incident radiation), one can easily start to look for the radioisotopes corresponding to the peaks in the spectrum.

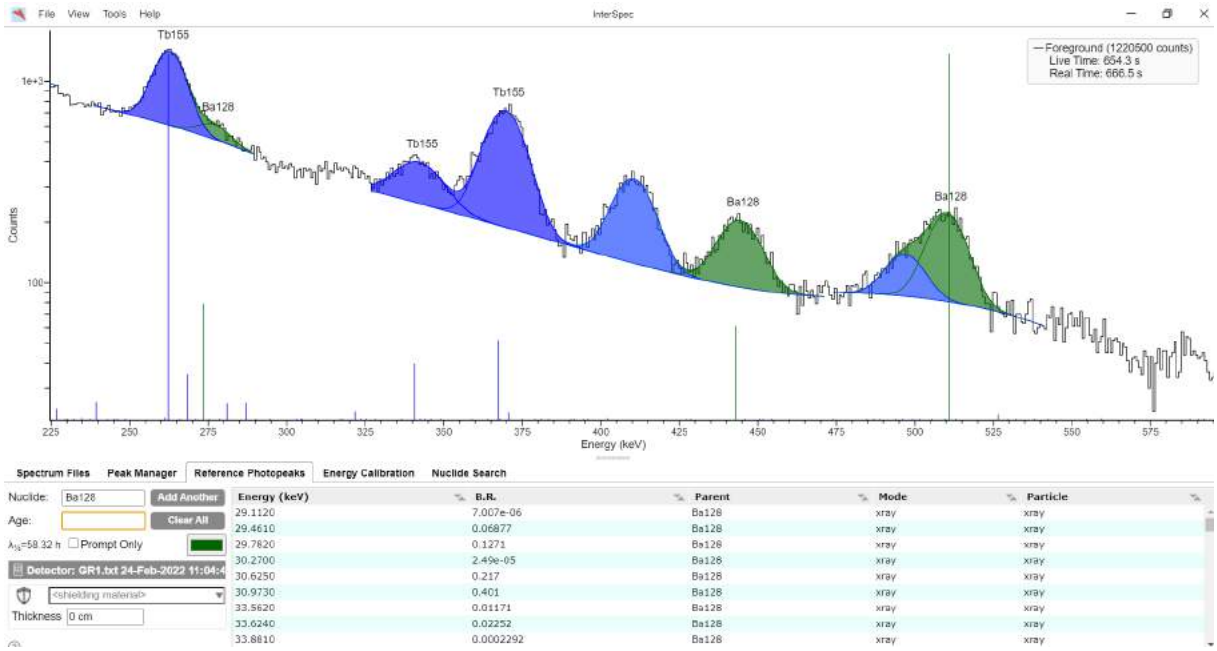

Figure 2.6: Screenshot of the InterSpec interface illustrating the use of reference lines for peak assignment: the lines of ^{155}Tb *and* ^{128}Ba *correspond nicely to most peaks in the spectrum.*

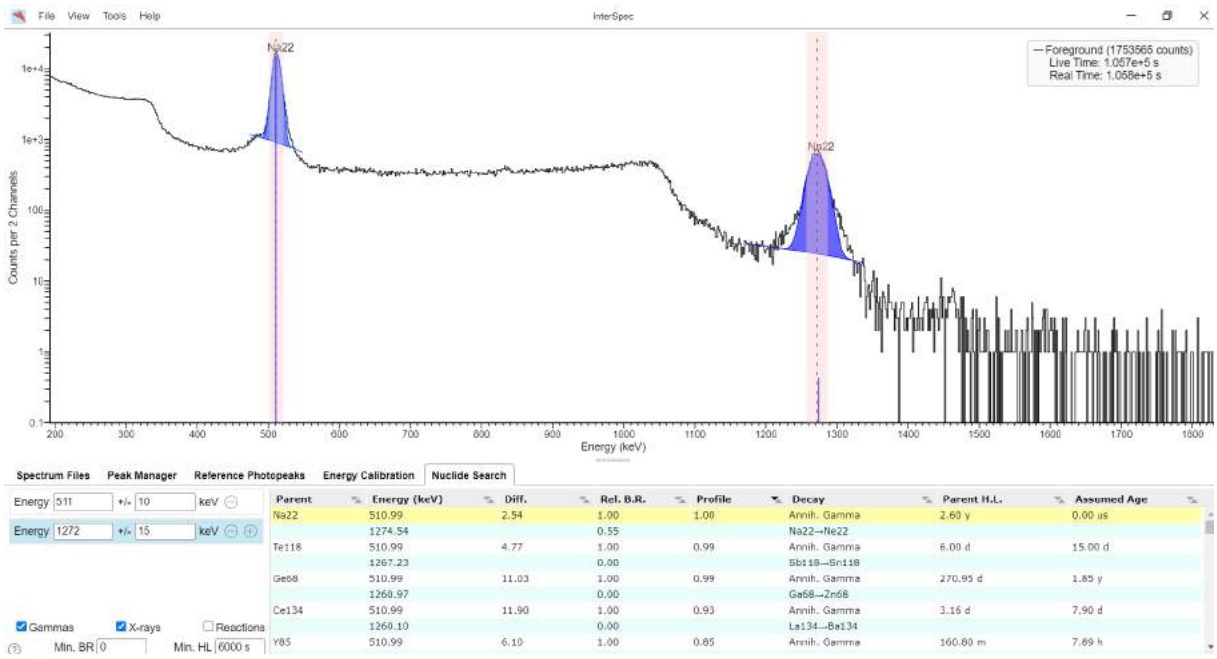

Figure 2.7: Screenshot of the InterSpec interface illustrating a nuclide search for the two peaks in the spectrum: ^{22}Na *appears to be a likely radioisotope.*

InterSpec holds an extensive database of nuclei with their half-lives, decay radiation, corresponding intensities and so forth. X-rays are also included. All spectral lines from a desired isotope can be superimposed on the uploaded spectrum, to see whether they overlap with any of the peaks. This is illustrated in Fig. 2.6. The relative heights of the lines correspond to the relative intensities of the emitted γ-rays. This is a helpful feature to check whether the observed amplitudes of the peaks in the spectrum make sense for the isotope under consideration (taking into account the absolute efficiency profile for the used setup as well). Reference lines can be shown for as many isotopes as desired, with a different colour for each. Besides looking at the lines of specific nuclei, one can also search by energy. InterSpec has a "Nuclide Search" option, which generates a list of all radioisotopes that emit radiation within a certain range around a selected energy. The list includes information such as the half-life of the radioisotopes and the energy difference between the selected energy and the emitted radiation by the isotope. This is useful in the process of selecting the most likely radioisotope from a vast number of candidates. If desired, the nuclide search can also be performed on more than one peak energy simultaneously. The generated list then consists of radioisotopes that emit radiation within a fixed range around each selected energy. An example of a nuclide search for two peaks is shown in Fig. 2.7.

2.4.2 Activity Calculation

Once all peaks in a γ-spectrum have been assigned to their corresponding radioisotope, one can quantify the activities of the different isotopes present in the sample under investigation. That is achieved by applying the following formula to each peak:

$$A = \frac{N(E)}{I(E) \times \epsilon_{abs}(E) \times t}. \tag{2.6}$$

In this expression, $N(E)$ represents the number of counts in the peak around energy E, $I(E)$ the intensity of the radiation contributing to that peak, $\epsilon_{abs}(E)$ the absolute detection efficiency of the setup at E, and t the livetime of the acquired spectrum (i.e. the duration of the measurement corrected for the dead time of the detector). The formula is derived from the definition of absolute efficiency [4].

The appropriate values for $I(E)$ are obtained from databases such as the Laboratoire National Henri Becquerel [23] and the ENSDF database by the National Nuclear Data Center (NNDC) of Brookhaven National Laboratory [24]. The livetime t of each acquisition is directly determined by KSpect. The absolute detection efficiency of the setup must either be calibrated for that particular setup or be calculated from the intrinsic efficiency of the used detector. In the latter case, one must correct for the solid angle Ω of the detector in the current setup, such that $\epsilon_{abs} = \epsilon_{intr} \frac{\Omega}{4\pi}$ [4]. Finally, to obtain the number of counts for each peak, each peak is fitted by a Gaussian profile and the fit is integrated within 2 to 3 standard deviations around the central energy. This is performed in python using the `lmfit` package. However, to ensure that as few as possible counts from the (Compton) background are included in the calculation – which would lead to an overestimate of the activity – first a Statistics-sensitive Non-linear Iterative Peak-clipping (SNIP) algorithm is applied to the spectrum. This is an iterative method that estimates the continuous background [25]. The estimated background can then be subtracted from the spectrum, thereby greatly reducing the influence of Compton effects on the activity calculation.

With the information from this chapter and the previous one in mind, we now turn to two case studies for the use of a Kromek CZT detector for γ-spectrometry in medical applications. The first case study (part II) deals with the production of terbium radioisotopes for medical applications. During the production process at CERN MEDICIS (Geneva, CH), γ-spectra are acquired with a Kromek GR1 detector to monitor the activity of Tb that is being collected. The γ-spectra also allow to identify and quantify possible contaminants in the collections. The second case study (part III) addresses the issue of waste management in hadrontherapy. In particular, proton-activated construction materials of the beam-line of the proton therapy centre PARTICLE (Leuven, BE) are studied. A Kromek GR05 detector is used to acquire γ-spectra of the waste materials, from which the radioisotopes produced by proton-induced reactions with construction materials can be identified and quantified.

Part II

Case Study 1: Terbium Production at MEDICIS

Chapter 3

Terbium Radioisotopes for Medical Applications

The first case study of the use of a Kromek CZT detector deals with the production of terbium radioisotopes for medical applications. The Tb radionuclide family contains four isotopes with suitable decay characteristics for use in nuclear medicine, namely ^{149}Tb, ^{152}Tb, ^{155}Tb and ^{161}Tb. The first section of this chapter discusses their individual and complementary potential. Afterwards, the production of the neutron-deficient radioisotopes ^{149}Tb, ^{152}Tb and ^{155}Tb is investigated. Section 3.2 of this chapter explains the Isotope Separation On-Line (ISOL) technique used for this purpose. Section 3.3 describes how this is implemented at the CERN MEDICIS facility. The role of the CZT detector at MEDICIS is explained in that section as well. The next chapter then reviews the operation of MEDICIS for the production of Tb in 2021, based on data acquired by the CZT detector during Tb collections.

3.1 The Tb Quadruplet

Terbium is the only element for which there are four radioisotopes with suitable decay characteristics for clinical use [26]. The so-called "Tb quadruplet" consists of ^{149}Tb, ^{152}Tb, ^{155}Tb and ^{161}Tb [26, 27]. In Fig. 3.1 an overview is given of the decay properties for each of these isotopes. Of particular interest is the α-emitter ^{149}Tb, which would fill the current gap in the medical radionuclide landscape regarding targeted α-therapy (TAT). It is the only α-emitter lighter than lead with well-known chemical properties and a half-life that is suitable for medical applications. Moreover, it decays to long-lived daughter

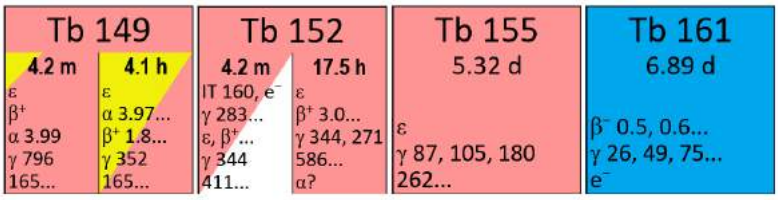

Figure 3.1: Decay characteristics for the four clinically relevant Tb radioisotopes [3].

nuclei that are stable against α-decay, thereby limiting additional radiation dose to the patient due to decay of the daughter nuclei [28, 29]. This represents a major advantage of ^{149}Tb over other candidates for TAT. Thanks to its β^+-decay branch, ^{149}Tb can also be used for positron emission tomography (PET). This imaging technique is based on coincident detection of the two annihilation photons stemming from β^+-decay inside the body. When applied during the treatment, it allows to track the bio-distribution of ^{149}Tb and to verify the progress of the α-therapy [29]. The second isotope in the Tb quadruplet, ^{152}Tb, also finds applications in PET imaging. In particular, it would be useful to perform PET with ^{152}Tb before administering α-therapy with ^{149}Tb, because this makes patient-specific dosimetry possible [26, 27]. The third isotope, ^{155}Tb, can be used for single-photon emission tomography (SPECT). In this technique, γ-rays emitted in the decay of the radioisotope are detected to acquire an image of its bio-distribution. Finally, ^{161}Tb is suitable for both SPECT imaging and targeted electron therapy. Similarly to the case of ^{149}Tb and ^{152}Tb, patient-specific dosimetry for the electron therapy with ^{161}Tb could be performed by first making a SPECT scan with ^{155}Tb [26, 27].

The different decay modes for all four isotopes allow the Tb quadruplet to be used for both imaging and therapy. This opens the door to "theranostics", where diagnostics and therapy are combined using a matched pair of diagnostic and therapeutic radioisotopes. The advantage of using radioisotopes of the same element for this purpose is that their chemistry is the same. Hence, radiopharmaceuticals can be developed with the same pharmacokinetics and bio-distribution for all isotopes and thus for both imaging and therapy [27]. That way, personalised treatments become possible.

3.2 ISOL Production

Whether a radioisotope can be used for medical applications depends not only on its decay characteristics (i.e. half-life and type and energy of decay radiation) but also on the ease with which it can be produced at a large scale and high purity [5]. Of the Tb quadruplet, only the production of the neutron-rich isotope ^{161}Tb has been established so far. ^{161}Tb is produced by neutron irradiation of purified gadolinium samples via the reaction $^{160}\mathrm{Gd}(n,\gamma)^{161}\mathrm{Gd}$ after which ^{161}Gd β^--decays to ^{161}Tb [27, 30]. This is carried out, for example, at the BR2 reactor at SCK CEN in Belgium [30]. Thanks to the aforementioned identical radiochemistry of the radioisotopes from the Tb quadruplet, preclinical research is already ongoing with ^{161}Tb, paving the way for the others. Meanwhile, further research is being done on the production of the neutron-deficient radioisotopes. Various production routes have been investigated, such as light ion induced reactions, heavy ion induced reactions and spallation reactions. In the end, it is the latter combined with Isotope Separation On-Line (ISOL) that seems the most promising [27].

The ISOL production method starts from the irradiation of a heavy target by a proton beam of high energy, such that spallation reactions can occur. Remembering the discussion on proton-induced reactions in section 1.2.1, for very high proton energies, one can expect virtually all isotopes lighter than the target nucleus and on the neutron-deficient side of the line of stability to be produced. Then, the generated nuclei are extracted from the target, ionised, and the desired radioisotope is separated from all the others. Fig. 3.2

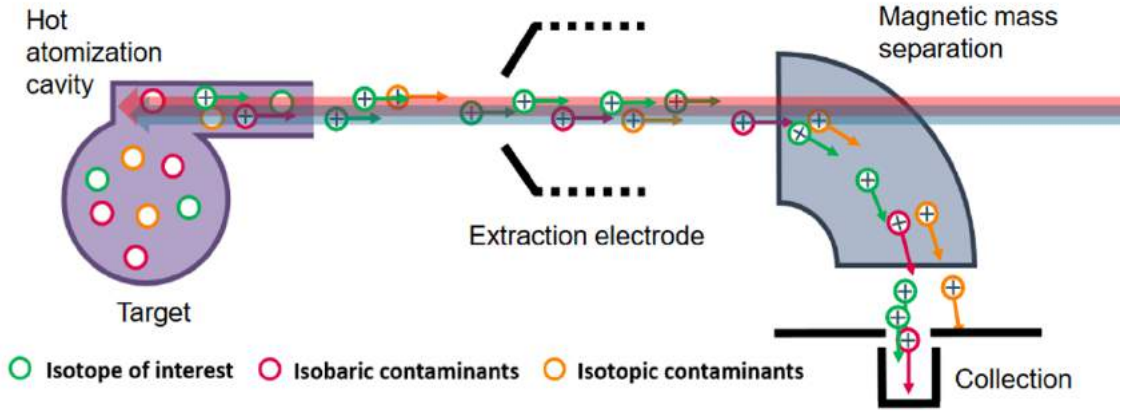

Figure 3.2: Schematic representation of the ISOL method with laser ionisation. The separation of the isotope of interest from isobaric and isotopic contaminants throughout the different steps of the method is highlighted. Picture from Ref. [31].

gives a schematic overview of the different steps in the ISOL production method (except the target irradiation).

Diffusion & Effusion After production by spallation reactions, the radioisotopes must be extracted from the target. For this purpose, the target is heated to temperatures on the order of 2000 °C [32, 33]: under influence of the provided thermal energy, the atoms diffuse through the target until they eventually effuse out of it and into an ion source. The target is heated by applying a current to it. Below approximately 2100 °C, a linear relationship holds between the current applied to the target and the target's temperature. Research is ongoing to determine the relation at high temperatures.

Ion Source In the ion source, the atoms of the element of interest are ionised, so they become charged and can be attracted by an extraction electrode for collection. There are three types of ion sources that are most commonly used at ISOL facilities. They rely on electron impact ionisation, surface ionisation and element-selective laser ionisation [8]. For the Tb collections at MEDICIS in 2021 (see chapter 4), both a surface ion source and laser ion source were used. Surface ionisation is based on the interactions of atoms with a heated surface. Depending on the ionisation potential and electron affinity of the element, the atom can lose or gain an electron in these interactions. For positive surface ion sources (i.e. generating singly-charged positive ions), construction materials that have high work functions and can be heated to high temperatures are used. Typical material choices include tantalum, tungsten and rhenium [8]. A disadvantage of surface ionisation is that this process is selective only when the produced elements have very different ionisation potentials [8]. So, in general, aside from the desired radioisotope, other elements are ionised as well. Much higher selectivity is obtained by laser ionisation. This approach makes use of the unique electronic level structure for each element. By tuning the wavelength of one or more lasers, the atoms of a specific element are step-wise excited towards the continuum of states above the ionisation energy. The highest ionisation efficiency is obtained when the ionisation step is also a resonant excitation, for

example to an auto-ionising state. Ion sources using this technique are called resonance ionisation laser ion sources (RILIS) [8, 32].

Mass Separation Once atoms are ionised, they are accelerated towards a mass separator. The mass separator consists of an analysing magnet that separates isotopes by mass according to their bending radius through a homogeneous magnetic field. This relies on the effect of the Lorentz force due to the magnetic field on the charged particles: it bends each particle into a circular path with radius

$$r = \frac{mv}{qB}, \tag{3.1}$$

where m is the mass of the particle, v its velocity, q its charge, and B the size of the magnetic field [2]. Thus, a different mass induces a different radius, and different isotopes of the same element can be separated from each other.

Chemical Purification In the best case scenario, the ion source is perfectly element-selective, such that it excludes all elements other than that of the desired radioisotope from the collection. The electromagnetic mass separator subsequently removes any isotopic contaminants, and the desired radioisotope is collected at very high purity. However, in reality, surface ionisation will always lead to isobaric contamination (i.e. contamination by isotopes of a different element but approximately the same mass). These contaminants cannot be removed by mass separation, so they are collected together with the desired radioisotope [7, 33]. This is illustrated in Fig. 3.2. Hence, to obtain a high purity sample of the desired radioisotope, chemical purification techniques must be applied after the collection. The potential of RILIS becomes exceedingly clear in this respect: by specifically enhancing the ionisation efficiency of the desired element, it greatly improves the purity of the generated ion beam [33].

Currently, the ISOL method is being performed for the neutron-deficient Tb isotopes only at CERN MEDICIS (and ISOLDE to a less extent) [30]. How the technique is implemented at that facility is described in the following section.

3.3 The MEDICIS Facility

The CERN MEDICIS facility (MEDical Isotopes Collected from ISolde) is a unique facility designed for the production of non-conventional radioisotopes for research and development in medical imaging and therapy [34]. An overview of its different components is given in Fig. 3.3. MEDICIS is an off-line facility built as an extension to ISOLDE (Isotope Separation On-Line DEvice). At ISOLDE, the ISOL method is applied to produce radioisotopes for medical applications as well as for diverse experiments in fundamental nuclear physics research. For the latter purpose, the radioisotopes are sent to specialised experimental setups after the mass separator, instead of being collected. The targets at ISOLDE are irradiated with a 1.4 GeV proton beam from CERN's Proton Synchrotron Booster (PSB). MEDICIS exploits the fraction of protons that have not interacted in the ISOLDE target ($> 65\%$) by placing an additional target right behind it [35]. This is illustrated in Fig. 3.4. This irradiation mode is referred to as "indirect irradiation". Direct

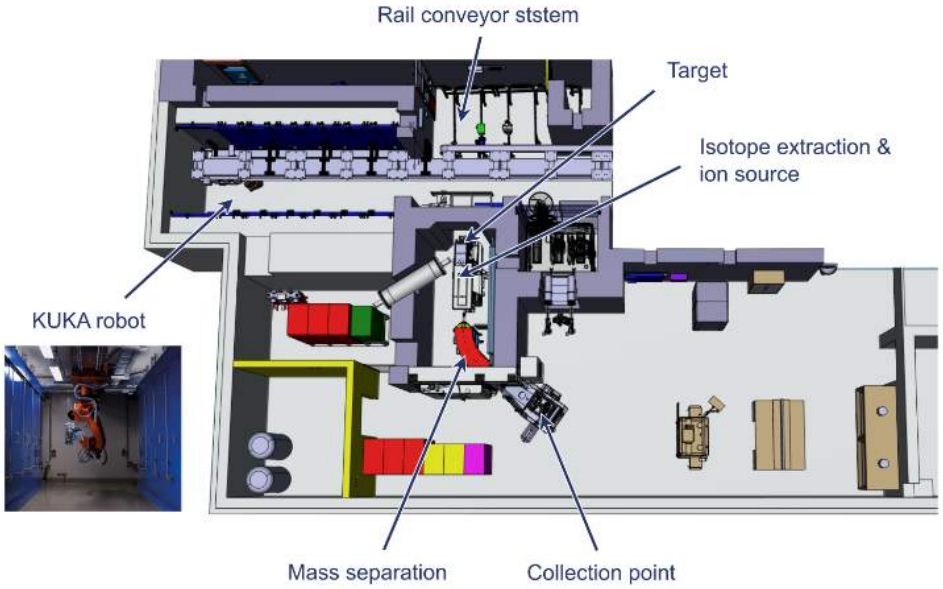

Figure 3.3: Overview of the MEDICIS facility at CERN. Picture from Ref. [36].

irradiation by the 1.4 GeV proton beam from PSB is possible as well, if one removes the ISOLDE target [35]. After irradiation, the MEDICIS target is transported to the off-line facility by a robotic arm ("KUKA robot") for radioisotope separation (see Fig. 3.3).

3.3.1 Off-line Separation & Collection

As MEDICIS is an off-line facility, the target irradiation and subsequent extraction and separation of radioisotopes are decoupled. So, the application of the ISOL method is in this case not truly "on-line". Nevertheless, all the steps discussed in section 3.2 remain valid once the irradiated target is installed at the target position in MEDICIS: the target is heated to high temperatures to allow diffusion and effusion, the radioisotopes are ionised

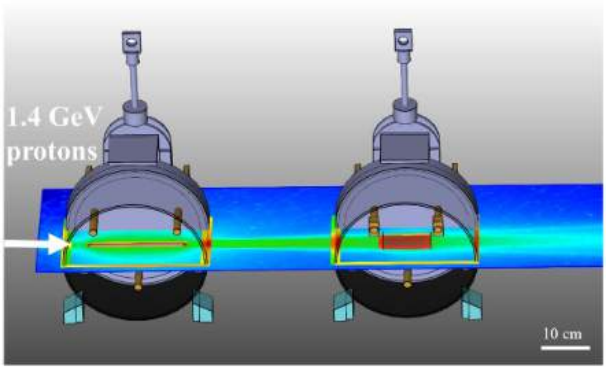

Figure 3.4: Schematic representation of the arrangement of the targets for ISOLDE (left) and MEDICIS (right). Picture from Ref. [34].

by an ion source[1], and finally mass separated using an electromagnetic mass separator. After mass separation, the separated isotopes are collected by implanting them on one-sided Zn-coated gold foils (0.5 mm thick) [34]. A blueprint of the collection chamber where this happens is shown in Fig. 3.5a. Three implantation foils can be inserted into the collection box simultaneously on a rail. By adjusting the position of the rail appropriately, one can select the foil on which the radioisotopes are implanted. This allows to obtain multiple, distinct samples of the desired radioisotope during a single collection, simply by moving the rail. However, one can also opt for collecting a high activity of the isotope on a single foil instead of dividing it over three. Not all three positions on the rail must then be loaded with an implantation foil. An example where this is the case is shown in Fig. 3.5b. This is a picture of the collection box with foils M148 and M149, which were used for the collection of ^{155}Tb in August 2021 (more about this collection in chapter 4).

After the collection is terminated, the implanted foils are retrieved from the collection box with a shielded trolley [34] and then subjected to precision γ-spectrometry with a high purity germanium detector (HPGe, type Falcon 4). Finally, they are transported to partner institutes and research facilities for further radiochemistry manipulation [34].

The off-line separation process at MEDICIS offers the advantage that externally irradiated targets can be handled as well [34, 35]. Consequently, the operation of MEDICIS is not dependent on the proton supply by PSB. Furthermore, it means that targets can be irradiated at lower energies at other facilities, such as ARRONAX in France (30 MeV) [35]. The different energy of the protons influences the nuclear reactions by which radioisotopes are produced in the target, resulting in a different mixture of product isotopes (see section 1.2.1). Depending on the cross sections for the reactions leading to a specific radioisotope, it may be more valuable to irradiate at low or intermediate energy instead of 1.4 GeV at CERN. Another benefit of the off-line separation is that the target may be temporarily stored and allowed to cool down before the extraction at MEDICIS. This aspect is further discussed in chapter 4 in light of the Tb collections of 2021.

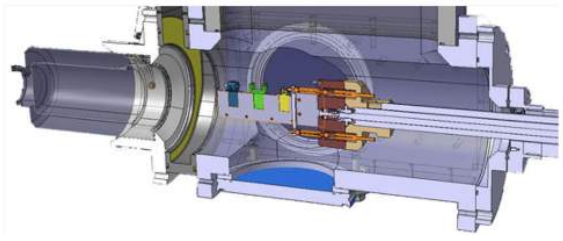

(a) Technical drawing of the collection box with three foils inside. Ref. [38].

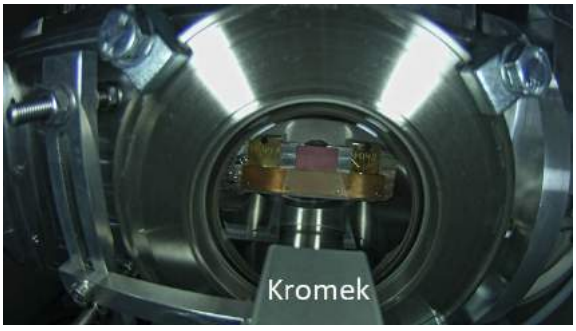

(b) Picture of the collection box. Two foils are visible, the middle site is left empty.

Figure 3.5: Technical sketch (a) and picture (b) of the Zn-coated Au foils inside the collection box for implantation. On the picture, the position of the Kromek CZT detector in front of the chamber is indicated.

[1]For laser ionisation, MEDICIS has its own resonance ionisation laser ion source (RILIS), called MELISSA or MEdicis Laser Ion Source for Separator Assembly [37, 34].

3.3.2 Use of the Kromek GR1 CZT Detector

At the end of a collection, the activity of the implanted radioisotope is evaluated by γ-spectrometry with a HPGe detector [34]. Even so, it is valuable to be able to track the progress of the collection while it is happening as well. At MEDICIS, this is achieved by using a CZT detector of type Kromek GR1. Thanks to the compact size of the detector, it can be conveniently mounted in front of the collection box. This is illustrated in Fig. 3.6. The purpose of the CZT detector is to acquire γ-spectra regularly during the collection, from which the activity of the implanted radioisotope can be determined. That way, the activity can be monitored, and one can, for example, easily observe when the target is depleted of the desired radioisotope (i.e. when its activity stagnates or even starts to decrease due to decay). In addition, the spectra acquired by the CZT detector can be used to investigate the effect of target temperature and other parameters on the efficiency of the collection. Finally, it is also a useful tool to detect contaminants early on. All of this is put into practice in the next chapter for the analysis of the Tb collections in 2021.

Before starting with the analysis, it is important to point out the characteristics of the specific GR1 detector used at MEDICIS. A thorough calibration of this detector was performed by P. Christodoulou (see Ref. [16]). The relationship between energy and channel number in the detector was found to be

$$E\ [\text{keV}] = 0.7510(10) \times \text{channel} - 0.99(36). \tag{3.2}$$

The efficiency response of the detector was fitted by

$$\begin{aligned}\epsilon_{\text{abs}}(E) = \exp\Big(&- 953(224) + 617(150) \cdot \ln E - 150(38) \cdot (\ln E)^2 \\ &+16(4) \cdot (\ln E)^3 - 0.6(2) \cdot (\ln E)^4 \Big).\end{aligned} \tag{3.3}$$

In this expression, ϵ_{abs} represents the absolute efficiency (not in %) for the detection setup used in the collection chamber. In other words, attenuation due to the window of the collection box etc. are directly taken into account. In determining the activity according to Eq. 7.4, no further corrections need to be applied to the efficiency factor.

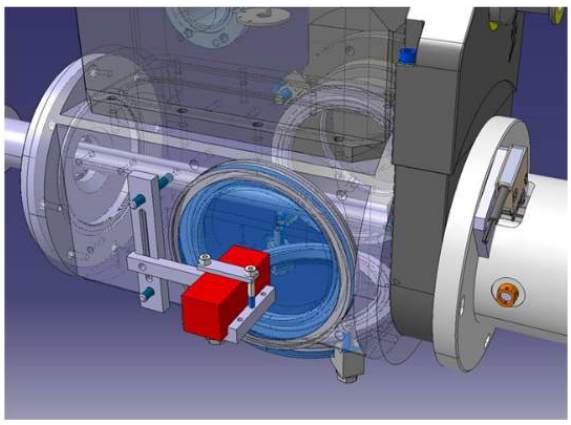

(a) Sketch of the collection box with GR1 detector in front of it. Ref. [16].

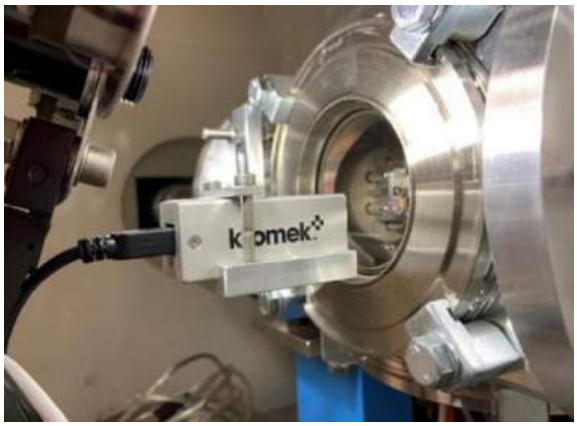

(b) Picture of the GR1 detector mounted in front of the collection box. Ref. [35].

Figure 3.6: Technical drawing (a) and picture (b) of the positioning of the Kromek GR1 detector in front of the collection box.

Chapter 4

Review of Tb Collections at MEDICIS in 2021

In 2021, there were three collections for the neutron-deficient isotope ^{155}Tb at MEDICIS. This chapter presents an analysis of the results of those collections, with particular focus on the spectra acquired by the Kromek GR1 CZT detector. The first section provides an overview of the conditions under which the different collections were performed, as well as the data that were collected for each. The discussion of the data is given in the second section of this chapter. The third and final section presents a conclusion on the operation of MEDICIS for ^{155}Tb in 2021 and an outlook towards future research on the production of neutron-deficient Tb isotopes at MEDICIS.

4.1 Collection Data

For all ^{155}Tb collections at MEDICIS in 2021, a tantalum target was irradiated at CERN with the 1.4 GeV proton beam from PSB. Furthermore, the same type of ion source was used for the three collections: laser ionisation was applied using the two schemes shown in Fig. 4.1, and surface ionisation occurred as well through interactions of the generated

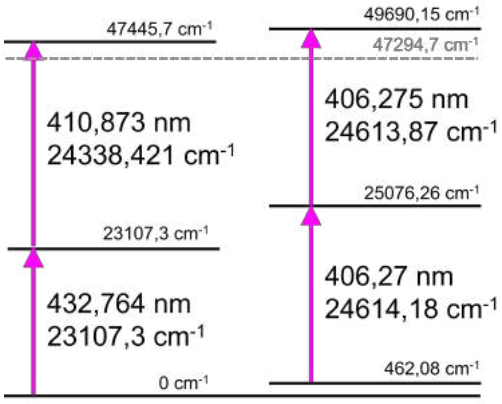

Figure 4.1: Laser schemes used at MEDICIS for the resonant laser ionisation of Tb.

atoms with the rhenium sides of the ionisation tube (see section 3.2). All other conditions, including duration of the collection and heating history of the target, were different. Here, the specifics for each collection are outlined, along with all the acquired data.

4.1.1 July Collection

The first ^{155}Tb collection of 2021 took place in July. The tantalum target was irradiated at ISOLDE for a total of 105 h before it was brought to the MEDICIS target extraction site. From July 15 to July 19, the indirect irradiation mode was employed for 88.7 h. Thereafter, the target was directly irradiated for another 16.3 h until July 20. At MEDICIS, first ^{128}Ba was extracted from the target and implanted in the collection chamber from July 22 onward. During this collection, a series of mass scans were performed[1], from which it was observed that there was ^{155}Tb coming out of the target. These mass scans are shown in Fig. 4.2a. For the rising target temperatures up to 600 A ($\approx$ 1970 °C), the peak in ion current around mass number 155 increases. Therefore, when no more ^{128}Ba was coming out of the target, it was decided to start a new collection for ^{155}Tb. The target was first cooled down to preserve the ^{155}Tb while the implantation foils in the collection box were changed and the laser setup was switched from Ba to Tb. The collection of ^{155}Tb started on July 23 and lasted for 69.8 h. The radioisotope was implanted on two Zn-coated Au foils, labelled M113 and M114.

At the beginning of the ^{155}Tb collection, again a series of mass scans were performed to investigate the effect of the lasers. The relevant part of these scans is shown in Fig. 4.2b. Two scans were taken with the lasers on, and one with the lasers off. Afterwards, the lasers were left on throughout the rest of the collection.

Six γ-spectra were acquired with the GR1 CZT detector during the collection. All spectra are given in Fig. 4.3. The peaks were assigned using Interspec (see section 2.4.1) and show

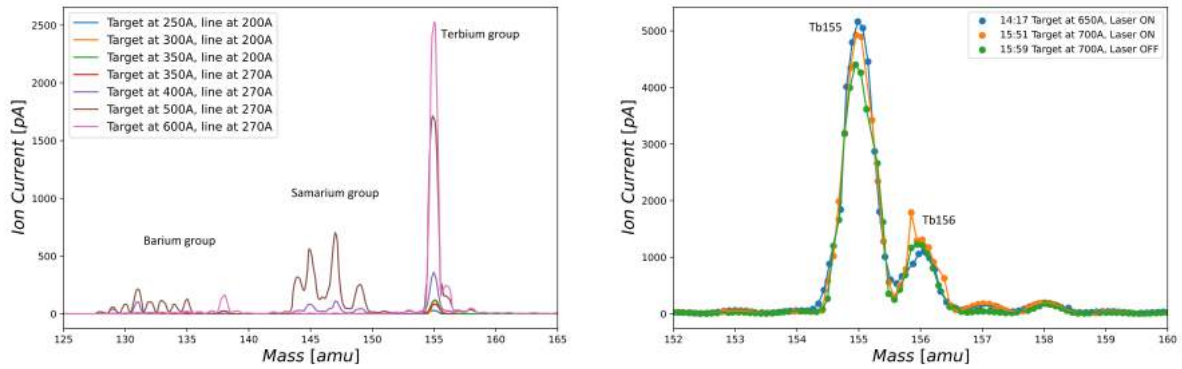

(a) Mass scans performed during the ^{128}Ba collection prior to the ^{155}Tb collection.

(b) Relevant part of the mass scans performed on 23/07 at the start of the ^{155}Tb collection.

Figure 4.2: Mass scans performed before (a) and during (b) the July collection of ^{155}Tb. The individual mass scans are labelled by the currents applied to the target and the transfer line to the ion source (defining their temperatures, as explained in section 3.2).

[1]In a mass scan, the mass separator scans over a range of masses and for each mass the ion current is measured. For the measurement of the current, at MEDICIS a Faraday cup is used.

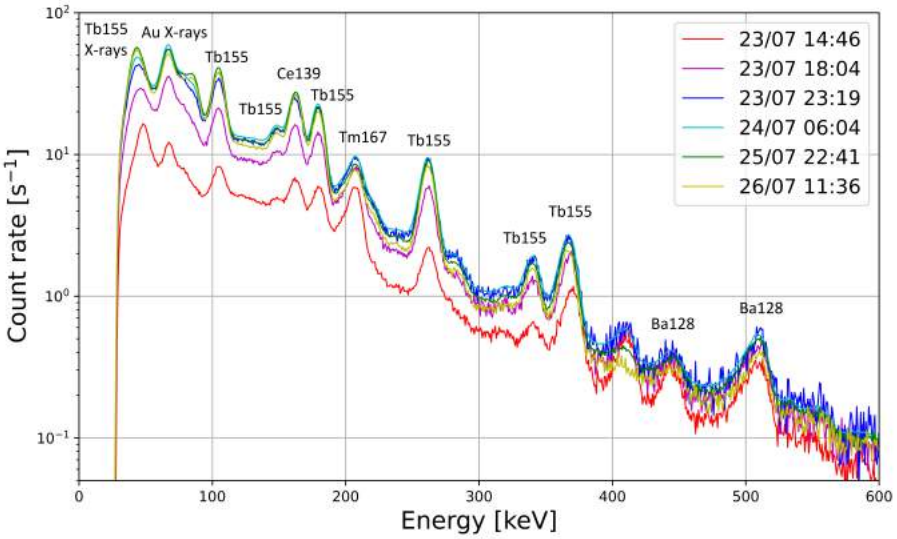

Figure 4.3: All γ-spectra acquired by the CZT detector during the July ^{155}Tb collection.

the presence of ^{128}Ba, ^{155}Tb, ^{139}Ce and ^{167}Tm as well as gold (X-rays). The Au X-rays can be ascribed to excitation of the gold implantation foils (see section 2.2). The ^{128}Ba stems from the collection of this radioisotope prior to the ^{155}Tb collection: not all ^{128}Ba was implanted on gold foils, part of it was sputtered inside the collection chamber. The signal of this sputtered radioisotope is still detected by the CZT detector, yet it does not mean that there is also ^{128}Ba implanted during the ^{155}Tb collection. Similarly, the peak corresponding to ^{167}Tm in the γ-spectra stems from sputtered ^{167}Tm of a previous collection of that radioisotope. In contrast, the presence of ^{139}Ce cannot be ascribed to previous collections. Instead, this radioisotope is implanted together with ^{155}Tb: cerium oxide (^{139}Ce^{16}O) represents an isobaric contaminant of ^{155}Tb [33]. The activity was calculated for both ^{155}Tb and the contaminating ^{139}Ce^{16}O for each acquired γ-spectrum. This was done as described in the methodology in section 2.4.2. A proof of principle is

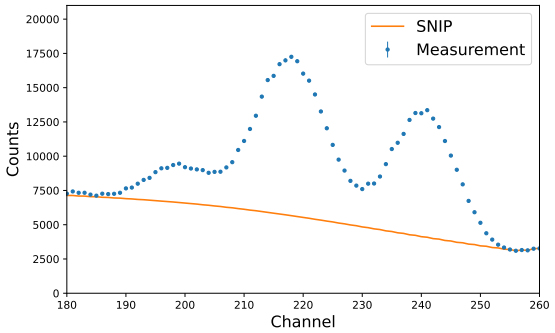

(a) Approximation of the smooth background by the SNIP algorithm. This background is subtracted before any further analysis.

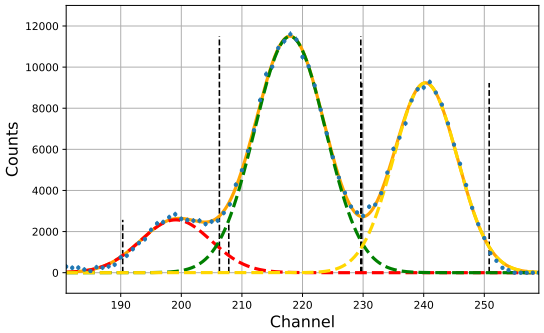

(b) Gaussian fits of the peaks ($\chi^2_{red} = 1.668$). The black lines represent the 2σ intervals under which is integrated.

Figure 4.4: Specific example of how the methodology described in section 2.4.2 is put into practice. The example concerns the γ-spectrum acquired at the end of the July collection. The spectrum is shown in channel space for energies between 130 keV and 190 keV. This part of the spectrum contains the peak by ^{139}Ce surrounded by two ^{155}Tb peaks.

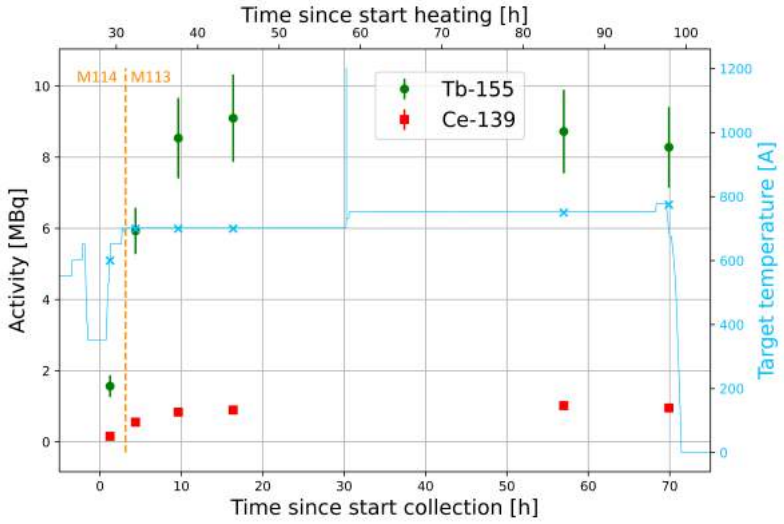

Figure 4.5: Activity trend vs. time for ^{155}Tb *and its contaminant* ^{139}Ce *during the July collection. Note that the error bars on the* ^{139}Ce *activities are too small to be visible in the graph. The orange dotted line indicates the switch between foils M114 and M113 for implantation.*

presented in Fig. 4.4. First, the background in the spectrum was approximated by the SNIP algorithm and subtracted. Then, the remaining peaks were fitted with Gaussian profiles and subsequently integrated within a 2σ interval around their centre. The integrated counts were finally substituted in Eq. 7.4 to determine the activity corresponding to each peak in the spectrum. The efficiency needed for this calculation was determined by Eq. 3.3. As there are several peaks due to ^{155}Tb, the weighted mean was taken of the activities corresponding to the individual peaks. The resulting activities for ^{155}Tb and ^{139}Ce are plotted against time in Fig. 4.5, together with the heating history of the target. The timeline is given with respect to both the start of the ^{155}Tb collection and the start of the heating of the target. There is a significant difference between these two points in time, because of the ^{128}Ba collection preceding the ^{155}Tb collection. During the ^{155}Tb collection, the target was heated up to 800 A ($\approx$ 2330 °C[2]).

On July 26, it was observed that no more ^{155}Tb was coming out of the target, so the collection was ended. The implantation foils were subjected to high-precision γ-spectrometry with a HPGe detector on July 28. The implanted activities of ^{155}Tb and ^{139}Ce on each foil are given in Tab. 4.1.

Table 4.1: Implanted activities of ^{155}Tb *and* ^{139}Ce *as measured on July 28.*

	^{155}Tb activity [Bq]	^{139}Ce activity [Bq]
M113	2.65E+06 ±3.5%	1.55E+05 ±11.0%
M114	2.07E+06 ±3.3%	5.67E+04 ±11.0%

[2]This is an estimate based on a linear relation between target temperature and applied current. Because this relation does not hold above 2000 °C (see section 3.2), the linearly extrapolated value may differ up to 100 °C from the true target temperature. The same holds for all temperatures in this chapter.

4.1.2 August Collection

For the August collection, the same target was used as in July. This time, it was irradiated at ISOLDE for a total of only 18.02 h. The irradiation took place on August 24 and August 25 in three runs with some cooling time in between. Only the direct irradiation mode was employed. Afterwards, the target was transported to the MEDICIS target station by the KUKA robot and the collection of ^{155}Tb was immediately started. The collection ran from August 25 to August 27 for a total of 39.25 h. Two implantation foils were loaded in the collection chamber, labelled M148 and M149, but ^{155}Tb was only implanted on M149.

During the collection, five γ-spectra were acquired by the Kromek GR1 CZT detector. They are shown in Fig. 4.6. The peak assignment points to the presence of Au (i.e. implantation foils), ^{155}Tb, ^{139}Ce and ^{155}Dy. Both ^{139}Ce (under the form of ^{139}Ce^{16}O) and ^{155}Dy represent isobaric contaminants that are implanted together with ^{155}Tb. The activity was calculated for all three radioisotopes for each γ-spectrum. For ^{155}Tb and ^{155}Dy, the weighted mean was taken of the activities determined by individual peaks. The final results for ^{155}Tb, ^{139}Ce and ^{155}Dy are plotted in Fig. 4.7, together with the heating history of the target. For this collection, the target temperature was increased up to 830 A ($\approx$ 2400 °C).

Besides γ-spectrometry with the CZT detector, several mass scans were performed during the collection. The relevant part of these scans is given in Fig. 4.8. The goal of the mass scans was to investigate the effect of the lasers on the yield at mass number 155. Therefore, several scans were taken with the lasers on and off for different target temperatures throughout the collection.

At the end of the collection, the implanted foil was immediately subjected to precision γ-spectrometry with the HPGe detector at MEDICIS. The measured activities for ^{155}Dy, ^{155}Tb and ^{139}Ce are given in Tab. 4.2.

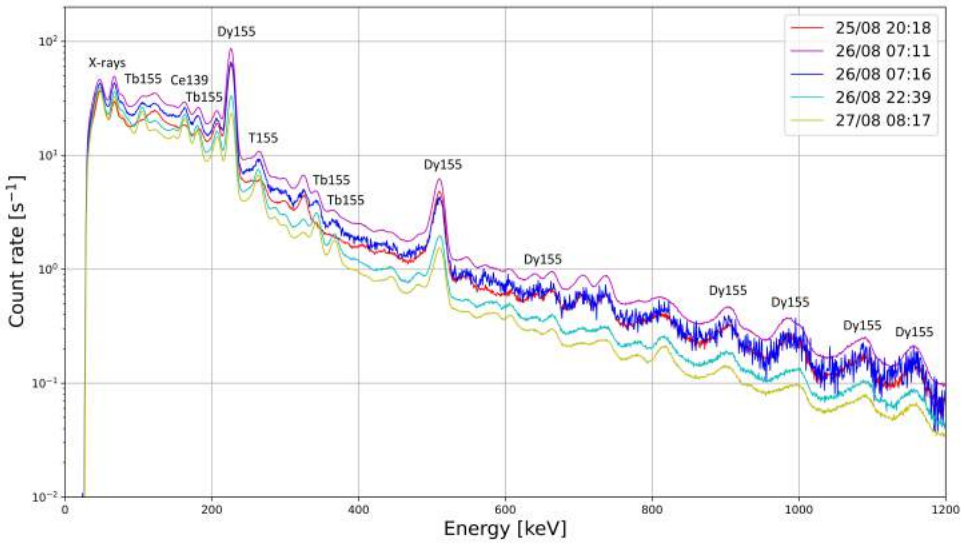

Figure 4.6: All γ-spectra acquired by the CZT detector during the August collection of ^{155}Tb. For clarity reasons, only the relevant peaks have been assigned on the figure.

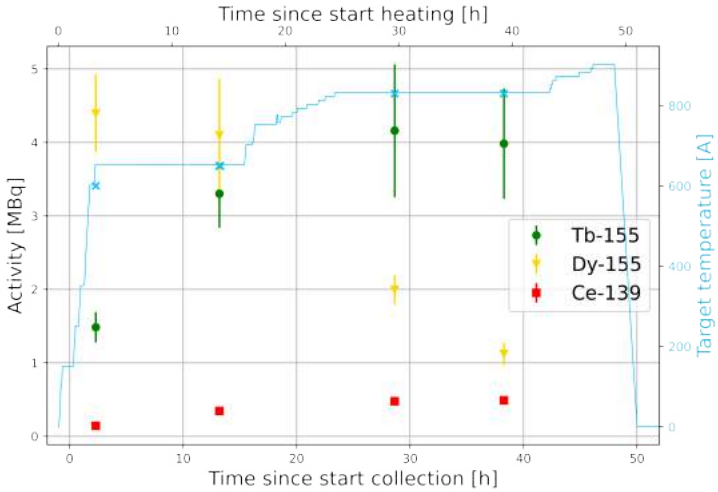

Figure 4.7: Activity trend vs. time for ^{155}Tb, ^{155}Dy and ^{139}Ce during the August collection.

Table 4.2: Implanted activities of ^{155}Dy, ^{155}Tb and ^{139}Ce as measured on August 27.

	^{155}Dy activity [Bq]	^{155}Tb activity [Bq]	^{139}Ce activity [Bq]
M149	6.20E+05 ±4.9%	2.25E+06 ±3.5%	1.63E+05 ±11.9%

4.1.3 October Collection

The last ^{155}Tb collection of 2021 was at the end of October. For this collection, again a tantalum target was irradiated directly. However, no information is available on the duration of the target irradiation nor on the exact starting point of the collection. The only data at hand are three γ-spectra acquired by the CZT detector, the first of which was taken right before the start of the collection (as "background" in the collection box). All spectra are shown in Fig. 4.9. Two observations are immediately made: the two spectra taken during the collection barely differ from the background spectrum, and there are no apparent peaks corresponding to ^{155}Tb. The peak assignment using Interspec reveals that the peaks in the spectra are due to Au (i.e. implantation foils), ^{153}Sm, ^{175}Yb, ^{44}Sc and

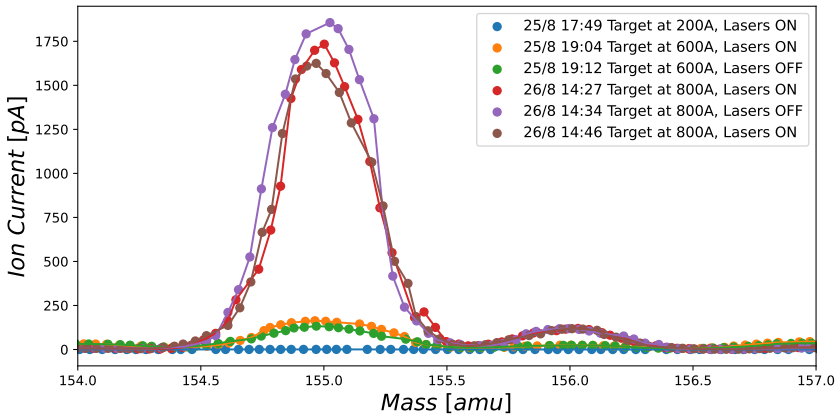

Figure 4.8: Relevant part of the mass scans performed during the ^{155}Tb collection in August.

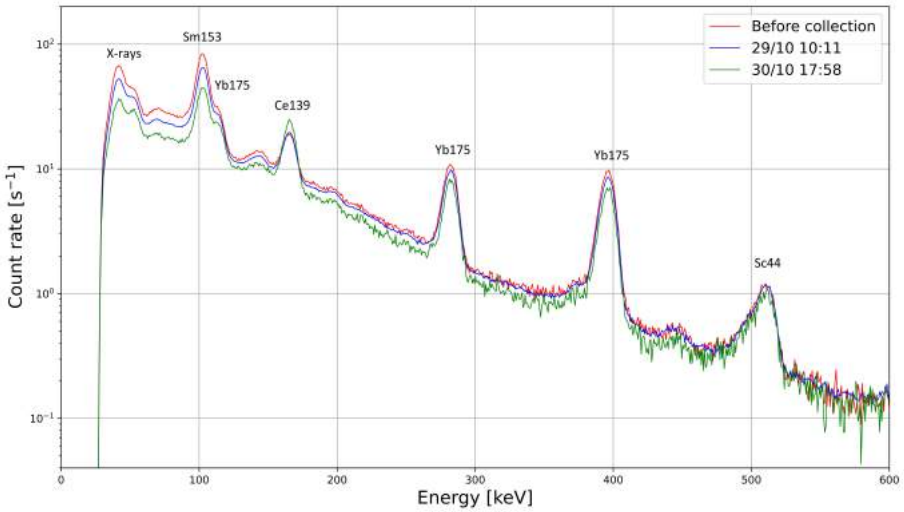

Figure 4.9: All γ-spectra acquired by the CZT detector during the October collection.

^{139}Ce. The first three radioisotopes stem from self-sputtering in the collection chamber during their respective collections earlier in October. The peak by ^{139}Ce, on the other hand, results from the isobaric contaminant ^{139}Ce^{16}O that is collected together with ^{155}Tb.

Activities were calculated for both ^{139}Ce and ^{153}Sm for each γ-spectrum. The latter was included because its peak at 103.180 12(17) keV overlaps with the main γ-ray of ^{155}Tb at 105.318(3) keV [24]. Hence, studying the decay in time of that peak could give an indication whether it is solely due to ^{153}Sm or whether there is a contribution by ^{155}Tb as well. The calculated activities are shown in Fig. 4.10 as function of time, together with the heating history of the target (heated up to a maximum of 700 A ($\approx$ 2145 °C)). The expected decay for pure ^{153}Sm is drawn as well. It agrees with the observed activities within uncertainties, confirming that no ^{155}Tb was implanted during this collection. Possible reasons as to why the collection was unsuccessful are explored in the next section.

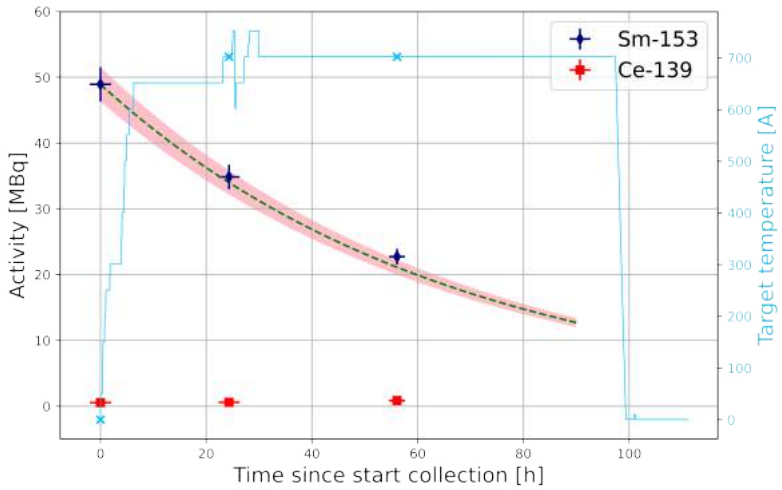

Figure 4.10: Activity trend vs. time for ^{139}Ce and ^{153}Sm during the October collection. The expected decay of ^{153}Sm from its activity in the first spectrum is drawn as well.

4.2 Discussion

To structure the discussion of the data presented above, this section is subdivided into several parts. Each subsection considers a specific aspect of the data to elaborate on. The focus throughout all subsections lies on the influence of various factors (e.g. laser ionisation, heating of the target) on the implanted yield of ^{155}Tb. The main question that is addressed, is "how can the collection efficiency be improved?". First, the efficiency is evaluated for the successful ^{155}Tb collections in July and August 2021. Then, the influence of target temperature and overall conditioning of the target on the ^{155}Tb yield is discussed, followed by the effects of laser ionisation. Finally, the issues of sputtering and contamination are addressed.

4.2.1 Collection Efficiency

To be able to quantify the overall efficiencies for the successful ^{155}Tb collections in July and August, FLUKA simulations of the target irradiation were made by C. Duchemin. These provided the activity of ^{155}Tb created in the target in both instances. The respective efficiencies were then determined as the ratio of the implanted activity (given in Tab. 4.1 for July and Tab. 4.2 for August) with respect to the activity in the target (determined by FLUKA). The results are given in Tab. 4.3. The collection efficiency was higher in July than in August, but for both collections it remained below 0.1 %. In appendix A, a poster is included on which these values are compared to efficiencies of collections of Tb from target that were externally irradiated at ARRONAX (Nantes, FR). The latter prove to be significantly larger (up to 11 %) [34, 39]. In the following subsections, several possibilities to increase the collection efficiency for internal irradiation at CERN are explored, based on the data that was acquired during the ^{155}Tb collections in 2021.

Table 4.3: Produced and implanted ^{155}Tb activities and the resulting collection efficiencies for the July and August collections. The measured activity mentioned for July is the sum of the activities for the two implantation foils given in Tab. 4.1.

	Activity in target [Bq]	Measured activity [Bq]	Efficiency [%]
July	5.00E+09 ±1.43%	4.72E+06 ±2.4%	0.094(3)
August	6.54E+09 ±1.80%	2.25E+06 ±3.5%	0.0344(14)

The total collection efficiency is the product of the efficiencies of all individual steps in the collection process. Therefore, one can write

$$\epsilon_{tot} = \epsilon_{diff} \cdot \epsilon_{eff} \cdot \epsilon_{ion} \cdot \epsilon_{sep} \cdot \epsilon_{transport} \cdot \epsilon_{implant} \cdot c_{decay}. \tag{4.1}$$

In this expression, ϵ_{diff}, ϵ_{eff}, ϵ_{ion} and ϵ_{sep} represent the efficiencies of the subsequent steps in the ISOL separation method: diffusion, effusion, ionisation, and mass separation. $\epsilon_{transport}$ represents the efficiency transport of the radioactive ion beam. $\epsilon_{implant}$ is the efficiency of the implantation process, or in other words the fraction of the isotope of interest which is not sputtered in the collection chamber. Finally, c_{decay} denotes a correction factor for radioactive decay during the collection.

To maximise the total efficiency, all partial efficiency factors must be maximised together. With respect to the correction factor for radioactive decay (c_{decay}), this entails that collections must be limited in duration compared to the half-life of the desired radioisotope (i.e. 5.32(6) d for ^{155}Tb [24]). Nevertheless, they must be long enough to allow sufficient implantation. In practice, one will always need to find the right balance between these two effects. The Kromek GR1 CZT detector can be helpful in this regard: by measuring the activity of the desired radioisotope regularly during a collection, one can directly observe when it stagnates or starts to decrease. For example, Fig. 4.5 and Fig. 4.7 show a decreasing trend for the ^{155}Tb activity towards the end of the July and August collection, respectively. This points to the target being depleted of ^{155}Tb, such that radioactive decay becomes the dominant effect over implantation. For the July collection, the ^{155}Tb activity starts to decrease sometime between approximately 20 h and 55 h after the start of the collection. For the August collection, the decrease sets in between 30 h and 40 h after the start of the collection. These numbers suggest the optimal duration of ^{155}Tb collections to be on the order of 30 h–40 h for an activity of the order of 5 GBq to 6 GBq produced in the target (see FLUKA results in Tab. 4.3). For different activities of ^{155}Tb in the target, the optimal duration will differ. To decide the exact moment to stop any particular collection, active monitoring of the ^{155}Tb activity with the CZT detector to detect stagnation or decrease seems to be a suitable solution.

Besides optimising the duration of the collection and thus c_{decay}, the partial efficiencies in Eq. 4.1 must all be maximised. The efficiency of the mass separation process (ϵ_{sep}) is very high and can effectively be approximated by 100 % [39]. Regarding the diffusion and effusion efficiencies (ϵ_{diff} and ϵ_{eff}), the influence of the heating history and conditioning of the target on the ^{155}Tb yield is discussed in section 4.2.2. Afterwards, in section 4.2.3 the effect on ϵ_{ion} of applying laser ionisation in addition to surface ionisation is investigated. Lastly, the efficiency of implantation ($\epsilon_{implant}$) and the issue of sputtering are considered in section 4.2.4.

4.2.2 Target Temperature & Conditioning

The effect of target temperature on the diffusion and effusion of ^{155}Tb out of the target is investigated here entirely in terms of the current applied to the target. However, it is important to keep in mind that at very high temperatures (i.e. above 2000 °C to 2100 °C) the relation between target current and target temperature is no longer linear (see section 3.2). Furthermore, when targets are reused, the same current might not induce the same temperature anymore, due to changed material properties and target degradation. Investigations are ongoing for both effects. For the time being, we focus strictly on the target current. To translate this to temperature, the power on the target should be studied.

Consider the mass scans acquired during the July and August ^{155}Tb collections, given in Fig. 4.2 and Fig. 4.8, respectively. Both sets of mass scans show an increasing trend in the ion current for increasing target currents. Looking at the scans that were acquired during the ^{128}Ba collection prior to the ^{155}Tb one in July (see Fig. 4.2a), the ion current

gradually rises up to a maximum of 2530 pA[3] while the target current is increased to 600 A (≈ 1970 °C). Upon increasing the target current further to 650 A (≈ 2032 °C) and 700 A (≈ 2145 °C) for the scans acquired during the ^{155}Tb collection itself (see Fig. 4.2b), the ion current at mass number 155 roughly doubles and reaches up to 5162 pA. As for the mass scans acquired during the August ^{155}Tb collection (see Fig. 4.8), the ion current increases first from about 1 pA to 163 pA upon going from 200 A (≈ 1025 °C) to 600 A, after which it shoots up to 1734 pA at 800 A (≈ 2330 °C). Besides the qualitative increasing trend, we note from the above numbers that the gain in ion current with each temperature step becomes ever larger for rising temperatures. From this, it can be concluded that the dependence on temperature does not obey a linear relationship, and that Tb needs very high temperatures in order to effuse out of the target efficiently.

Compared to the values from July, the ion current is significantly lower at similar (to even higher) temperatures in August. This can be explained in multiple ways. On one hand, the larger ion currents in July might be the consequence of the longer target irradiation time for that collection. More radioisotopes were produced throughout the whole irradiation process, and the long-lived ones built up in the target, leading to increased ion currents for all mass numbers upon extraction. It is important to note, however, that the contribution of ^{155}Tb to the gain in ion current by this effect is believed to be small. In fact, the ^{155}Tb activity in the target at the end of the whole irradiation process was revealed to be even lower in July than in August by FLUKA simulations (see Tab. 4.3). Thus, strictly considering the effect of the longer irradiation period, the larger ion current in July would be due to larger amounts of isotopes other than ^{155}Tb.
Another reason for the larger ion current could have to do with the influence of target degradation on the relation between the current applied to the target and the target temperature, since the target from the July collection was reused in August. Although research is ongoing to gain in-depth insight into this effect, it has been observed that proton irradiation and multiple heating cycles change the material properties of target. Consequently, the same currents might not correspond to the same temperatures in July and August. Furthermore, due to target sintering, diffusion and effusion of radioisotopes from the target are hampered.
Finally, the larger ion current in July could also be the consequence of conditioning of the target prior to the collection (i.e. heating for some time before the start of the ^{155}Tb collection). In July, there was conditioning of the target in the sense of a ^{128}Ba collection prior to the ^{155}Tb collection. In addition, even the ^{128}Ba collection did not start until two days after the end of the target irradiation, whereas the August ^{155}Tb collection began almost immediately after the end of the irradiation. Hence, a significant amount of the generated radioisotopes had already been extracted or decayed before the start of the ^{155}Tb collection in July. In this light, the gain in ion current can be interpreted as an argument in favour of the hypothesis that Tb is extracted and collected more easily when less other radioisotopes are present. This hypothesis is also supported by the major jump in the ion current observed after one day during the August collection. The steep increase could in this case be ascribed to the combined effect of the increased target temperature (up to 800 A) and the extraction and decay of other radioisotopes, allowing ^{155}Tb to come out more easily. In conclusion, both target temperature and target conditioning prior to

[3]The uncertainty on the measured ion currents is not available. All values quoted in the text are rounded to the nearest integer value.

the collection seem to have an effect on the ^{155}Tb yield. At this point, it is important to point out that the story is different for ^{149}Tb ($T_{1/2}$ = 4.118(25) h [24]) and ^{152}Tb ($T_{1/2}$ = 17.5(1) h [24]): given the short(er) half-lives of these radioisotopes, conditioning of the target prior to the collection is not an option. A potential alternative solution is presented in the conclusion and outlook in section 4.3.

Besides the mass scans, also the ^{155}Tb activities measured by the Kromek GR1 detector during the collections (shown in Fig. 4.5 for July and Fig. 4.7 for August) can provide insights to the discussion on target temperature and conditioning. The recorded activities for July are roughly twice as high as those for August. The final γ-spectra in both collections give 8.3(11) MBq and 4.0(8) MBq, respectively. Firstly, the changed material properties of the degraded target in August might contribute to this difference. As mentioned earlier, research is ongoing on this topic, so no final conclusion can be drawn on this matter here. Secondly, the higher activities in July could be ascribed to the influence of target conditioning prior to the ^{155}Tb collection. Hence, target conditioning might contribute to the higher collection efficiency for July. To uncover the precise dependence of the efficiency on conditioning and to find the most appropriate procedure, systematic research is required. Different temperature profiles must be tested in order to investigate the effect on the release of Tb from the target. It is expected to be particularly useful to study profiles where one first extracts radioisotopes other than ^{155}Tb at relatively low temperatures and then increases the temperature to values of the order of 800 A to allow efficient ^{155}Tb release. Additionally, the influence of target conditioning must be compared for different irradiation conditions. In general, the larger the integrated number of protons during the irradiation, the more radioisotopes are produced in the target. Therefore, target conditioning is expected to play a bigger role after irradiation with a large numbers of protons to ensure sufficient extraction and decay of radioisotopes.

At the end of this subsection, let us consider what can be said about the unsuccessful ^{155}Tb collection in October. No ^{155}Tb was observed by the Kromek GR1 detector during this collection, and there was no noticeable improvement with lasers. This suggests that there was no ionisation at all. In light of the foregoing discussion, it is important to note that the target temperature was of the same order of magnitude as for the successful July and August collections, so this did not prevent Tb from coming out of the target. On the other hand, there was no target conditioning prior to the ^{155}Tb collection in October. Possibly, Tb was blocked by everything else that was created during the direct target irradiation. However, in August the ^{155}Tb collection also started immediately after a period of direct irradiation, and in that case ^{155}Tb was collected. The difference between both collections might lie in the duration of the target irradiation: perhaps the target was irradiated longer in October and more radioisotopes were produced compared to August, which hindered the collection of Tb. Nevertheless, as the information on the duration of irradiation is not available, no definitive conclusion can be drawn on this matter.

4.2.3 Laser Enhancement & Saturation of the Ion Source

As explained in section 3.2, resonance laser ionisation is element-selective and thus strictly enhances the Tb yield, whereas surface ionisation ionises many other elements as well. To quantify the effect of laser ionisation for ^{155}Tb, the ion current at mass number 155 is

compared for lasers on and off, while keeping all other conditions the same. In particular, the target temperature must be constant, and the scans should only be several minutes apart, to minimise decay. We first consider the two mass scans (one with lasers on and one with lasers off) performed at 700 A during the July ^{155}Tb collection (see Fig. 4.2b). The yield at mass 155 is determined for both scans by fitting the peak by a Gaussian and subsequently integrating it within 2σ around its centre. Both fits are shown in Fig. 4.11a, and the resulting yields are given in Tab. 4.4. The increase in yield upon turning the lasers on is then calculated by subtracting the yield for the lasers off from that for the lasers on. This gives a difference of 182(116) pA. So, laser ionisation leads to 6(4) % enhancement of the yield, solely due to additional ^{155}Tb. In the same manner, the enhancement by laser ionisation can be determined for the two scans (again one with lasers on and one with lasers off) acquired at 600 A during the August collection (see Fig. 4.8). The fits of the peak at mass 155 in these scans are shown in Fig. 4.11b, and the resulting yields are given in Tab. 4.4. The difference in yield is in this case equal to 22(4) pA, leading to 28(5) % laser enhancement. The fact that the laser enhancement is considerably larger for these scans compared to those from July might be due to a lower total beam current before the mass separator: it has been observed before that for lower total ion currents, the effect of the lasers is larger [40]. However, for the collections studied in this thesis, no data is available on the total ion current before mass separation, so no definitive conclusion can be drawn on this matter.

The final set of mass scans that can be used to investigate the effect of the lasers on the ^{155}Tb yield is the set of three scans (two with lasers on and one with lasers off) acquired at 800 A during the August collection (see Fig. 4.8). However, in contrast to the aforementioned scans, this time the yield is lower for both scans with lasers on than for the one with lasers off: 752(15) pA and 780(19) pA for lasers on versus 918(22) pA for lasers off (see Tab. 4.4 and Fig. 4.8). So, there is no laser enhancement, and the yield is even reduced when the lasers are turned on. This suggests that the ion source is saturated. As

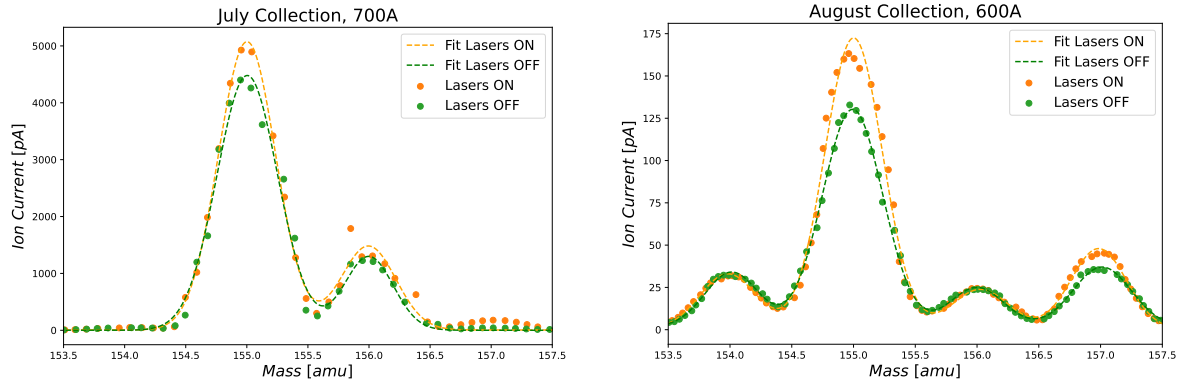

(a) Gaussian fits for the scans at 700 A *during the July collection* ($\chi^2_{red} = 25137$ *for lasers on,* $\chi^2_{red} = 32942$ *for lasers off).*

(b) Gaussian fits for the scans at 600 A *during the August collection* ($\chi^2_{red} = 25$ *for lasers on,* $\chi^2_{red} = 5$ *for lasers off).*

Figure 4.11: Fits of the 155 peak (and surrounding peaks) in the laser mass scans acquired during the July (a) and August (b) ^{155}Tb *collections. The large* χ^2_{red}*-values for the fits in (a) are a consequence of the unknown errors on the ion current. The colours of the individual scans were kept the same as the corresponding graphs in Fig. 4.2b (July) and Fig. 4.8 (August).*

Table 4.4: Overview of the laser mode, target temperature, integrated current over all masses and yield at mass 155 of the mass scans acquired during the July and August ^{155}Tb collections.

	July			August				
Lasers	ON	ON	OFF	ON	OFF	ON	OFF	ON
Temperature [A]	650	700	700	600	600	800	800	800
Total current [pA]*	50344	46811	42564	13656	11635	21115	**22872**	20251
Yield at 155 [pA]	2982(100)	2984(77)	2802(87)	100(4)	78(2)	752(15)	**918(22)**	780(19)

* The uncertainties of the ion currents are unknown, so the measured values are simply rounded to the nearest integer.

there was no target conditioning prior to the ^{155}Tb collection in August, a large variety of radioisotopes are still present in the target. Upon heating the target to 800 A, many radioisotopes are extracted and reach the ion source. As a consequence, so many ions are created by surface ionisation, that only a small portion of them finds their way out of the narrow ionisation tube. Which radioisotopes leave the ion source as ions in the end depends most likely on where they are ionised in the ionisation tube. This is elaborated on later. Furthermore, upon turning the lasers on, there is a small added effect due to the extra Tb that is laser ionised. This leads to the observed drop in the ion current of roughly 5 % compared to the current with the lasers off.

The reduction of ^{155}Tb as consequence of ion source saturation can be checked by activity measurements with the Kromek GR1 detector. Fig. 4.7 shows an overall increasing trend for the ^{155}Tb activity at the time of the mass scans at 800 A (i.e. at approximately 21 h after the start of the collection). However, no measurements were saved at that exact time, so the precise behaviour of the ^{155}Tb activity in response to the ion source saturation remains unknown. It could be that the increase in activity became less steep upon saturation, for example. Therefore, no final conclusion can be drawn here. What can be investigated from the available data is the change in total ion current leaving the ion source (i.e. the ion current integrated over all masses in the mass scans). The total ion current was determined for all three scans at 800 A. The results in Tab. 4.4 show the highest total current for the scan with lasers off. Moreover, the increase with respect to the scans with lasers on is significantly larger than the increase in ^{155}Tb yield alone. This means that the ion current decreases for all mass numbers and not only for ^{155}Tb.

The onset of saturation might have to do with the destruction of plasma in the ionisation tube. At high temperatures – and under influence of the electromagnetic field generated by the current that heats up the ion source – an electron plasma is presumably created in the ion source. This plasma generates an electric field that centres the ions inside the tube and thus prevents them from neutralizing against the walls of the ion source. Hence, even ions that are produced deep in the ion source can still come out, because they do not collide with the sides of the tube and neutralize there. However, when there are too many ions, the plasma collapses and there is no centring of ions anymore. The effect hereof is expected to be different for laser ionised and surface ionised ions. It depends on the distinct positions in the tube where laser ionisation and surface ionisation occur. As surface ionisation relies on interactions with a heated surface (rhenium in our case), this

occurs at the sides of the tube, including at the tip. Laser ionisation, on the other hand, is believed to take place throughout the volume of the tube. Based on this hypothesis, one would expect more reduction of Tb than the surface ionised ions, since part of the latter can still leave the ion source at the tip after the plasma has collapsed. As mentioned earlier, this could be checked by tracking the ^{155}Tb with the Kromek GR1 detector, but from the collection data discussed here, no final conclusion can be drawn. At this point, it is important to note that the destruction of plasma as the cause of saturation of the ion source is also a hypothesis that is still under investigation[4]. What can be considered a proven fact, is the saturation of the ion source itself. For other types of ion sources than the one used at MEDICIS, saturation has been observed as well. An example is given in appendix B, concerning the high purity Laser Ion Source and Trap (LIST) [41]. Besides the lack of target conditioning and target degradation, the saturation of the ion source in August is a potential factor that led to the lower collection efficiency in August compared to July (see Tab. 4.3).

Finally, let us again turn to the unsuccessful ^{155}Tb collection in October at the end of this subsection. Besides the possible influence of target conditioning – or more accurately, the lack thereof – saturation of the ion source might also be a reason why no ^{155}Tb was collected in this run. During the direct target irradiation, a lot of isotopes were created, and many of them were surface ionised in the ion source. The overload of surface ions then may have inhibited Tb from leaving the ion source, such that none was implanted. However, as mentioned at the end of the previous subsection as well, it is very difficult to deduce the exact cause for the absence of ^{155}Tb in the October collection, because of the limited information available. Both target conditioning and ion source saturation may play a role, but they cannot be appointed as the (only) reasons with absolute certainty – especially given the similar conditions for the successful ^{155}Tb collection in August.

4.2.4 Sputtering

In the spectra acquired by the Kromek GR1 CZT detector during the ^{155}Tb collections, not only peaks by ^{155}Tb and its contaminant(s) ^{139}Ce^{16}O (and ^{155}Dy) were identified, but also by other unrelated radioisotopes. For example, ^{128}Ba and ^{167}Tm were observed in July, and ^{153}Sm, ^{175}Yb and ^{44}Sc in October. As mentioned before, this is a consequence of self-sputtering in the collection chamber. In this section, the basic mechanism of (self-)sputtering is clarified briefly, and its effect on the implanted activities of ^{155}Tb and its contaminants is investigated.

Whenever ions are implanted on a thin foil, a number of atoms of the foil are removed due to sputtering [42, 43]. This is illustrated in Fig. 4.12. Over time, sputtering removes a significant fraction of the top layer of the implantation foil, so the thickness of the foil gradually decreases. As a consequence, the ions that were initially implanted at a well-defined depth eventually reach the surface of the foil and become themselves subject to sputtering by the incoming ions. This is referred to as self-sputtering. How much self-sputtering occurs, depends on a number of parameters, including the particle fluence,

[4]One of the people studying the mechanisms that govern the behaviour of ions in the ion source is S. Hurrier. She is predominantly involved in ion source development for SCK CEN, but the general concepts also hold for ion sources used at CERN.

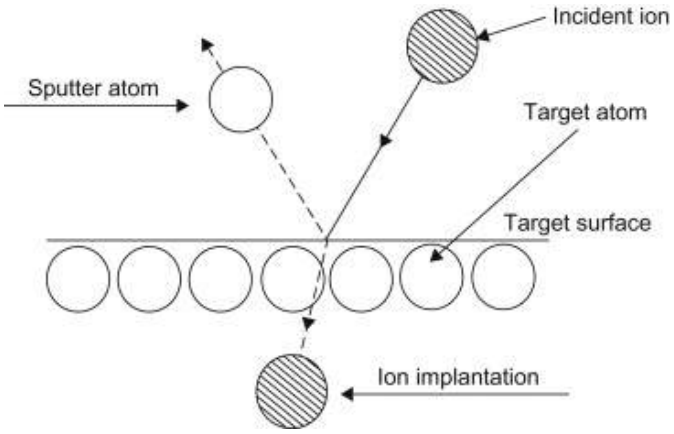

Figure 4.12: Schematic representation of the sputtering mechanism. Image from Ref. [43].

the atomic numbers of the material of the foil as well as of the incoming particles and the beam energy. Ultimately, the sample becomes saturated and each incoming ion ejects a previously implanted one.

In the context of radioisotope collections at MEDICIS, (self-)sputtering implicates that not all of the separated isotopes of interest stay implanted on the Zn-coated Au foils. Instead, part of them are sputtered off the foil again during the course of the collection. The sputtered fraction stays in the collection chamber until it has completely decayed. Therefore, the decay radiation of that particular radioisotope remains measurable by the Kromek GR1 detector even after the collection is ended and the implanted foils are removed from the collection chamber. That also has to do with the positioning of the CZT detector as shown in Fig. 3.6: the detector "sees" the collection chamber in its entirety. In other words, the activity recorded by the detector is equal to the sum of the activities implanted on all loaded implantation foils (e.g. both M113 and M114 in July) as well as the activity in the chamber itself.

To determine to which extent sputtering occurred for ^{155}Tb and it contaminants during the ^{155}Tb collections in July and August 2021, the "live" activities from the Kromek GR1 detector are compared to the activities measured by the HPGe detector after the collection, corrected for decay. The latter measurement is performed on the implanted foils after removing them from the collection box, so any signal of sputtered radioisotopes is removed. The results of those measurements are given in Tab. 4.1 for the July ^{155}Tb collection and in Tab. 4.2 for the August collection. Tab. 4.5 presents the decay corrected values, together with the final activities measured by the Kromek GR1 CZT detector and the consequential sputtered activities. It is important to note here that the results for the sputtered activities are to be interpreted as first approximations to the real sputtered activity, because the efficiency response of the GR1 detector is calibrated for the position of the implantation foil. Other points throughout the collection chamber will correspond to different efficiencies. Another way to quantify sputtering would be to perform an additional measurement with the CZT detector immediately after removing the implanted Au foils from the collection chamber. From the fraction of the activity that was sputtered (given in Tab. 4.5 in absolute units), the efficiency of implantation ($\epsilon_{implant}$) can be determined for each radioisotope per collection. The results in Tab. 4.5

Table 4.5: Measured ^{155}Tb, ^{139}Ce *and* ^{155}Dy *activities inside the collection box (by the Kromek GR1 CZT detector) and on the implantation foils (by the HPGe detector, corrected for decay), together with their calculated difference (i.e. the sputtered activity) and the sputtered fraction. Note that the measurements quoted for July are the summed activities on foils M113 and M114.*

		Activity by CZT [MBq]	Activity by HPGe [MBq]	Activity Sputtered [MBq]	Sputtered Fraction ($1 - \epsilon_{implant}$)
^{155}Tb	July	8.3(11)	6.1(2)	2.2(11)	0.26(14)
	August	4.0(8)	2.27(8)	1.7(8)	0.4(2)
^{139}Ce	July	0.95(50)	0.21(2)	0.74(5)	0.78(7)
	August	0.49(3)	0.16(2)	0.33(4)	0.67(8)
^{155}Dy	August	1.1(2)	0.71(3)	0.4(2)	0.4(2)

show that there is considerably stronger sputtering of ^{139}Ce than of ^{155}Tb and ^{155}Dy, relatively speaking. Thus, the implantation efficiency is higher for ^{155}Tb and ^{155}Dy. Most likely, this can be explained by the order in which the radioisotopes were extracted from the target and subsequently implanted. As discussed in section 4.2.2, Tb generally needs space to come out of the target. ^{139}Ce on the other hand, is extracted more easily and is therefore implanted first on the Zn-coated Au foil. As a consequence, the implanted ^{139}Ce is also the first to start sputtering off the implantation foil again.

To gain more insight into the mechanism of sputtering and how it can be controlled in order to increase the implantation efficiency, more in-depth research is ongoing. One line of investigation that is currently explored is the use of Al instead of Zn-coating on the gold implantation foils: because of its lower atomic number, Al tends to sputter less than Zn.

4.2.5 Contamination

Both ^{155}Dy and ^{139}Ce^{16}O are isobaric contaminants that are collected together with ^{155}Tb. ^{155}Dy decays to ^{155}Tb via β^+-decay with a half-life of 9.9(2) h [24], so it does not pose any problems in light of the production of ^{155}Tb for medical applications. Its relatively short half-life explains why no ^{155}Dy was observed in the γ-spectra from the July collection: after the preceding ^{128}Ba collection, ^{155}Dy had already decayed away. The other isobaric contaminant, ^{139}Ce^{16}O, is actually a contaminant in the sense that it is an unwanted by-product. ^{139}Ce has a half-life of 137.63(3) d [24], meaning that it remains present in significant amounts in the implanted foils even longer than ^{155}Tb itself (which has a half-life of 5.32(6) d). Hence, it must be removed from ^{155}Tb samples intended for medical use by chemical separation techniques. Typically, the radionuclidic purity of radiopharmaceuticals (i.e. ratio of the activity of the desired radioisotope to the total radioactivity of the sample) must be higher than 99.9 % [44, 45]. Of course, it is beneficial to minimise the amount of ^{139}Ce^{16}O implanted together with ^{155}Tb in the first place.

At MEDICIS, the purity of implanted samples can be monitored in real time with the Kromek GR1 CZT detector. The activity ratio of ^{139}Ce with respect to ^{155}Tb is plotted

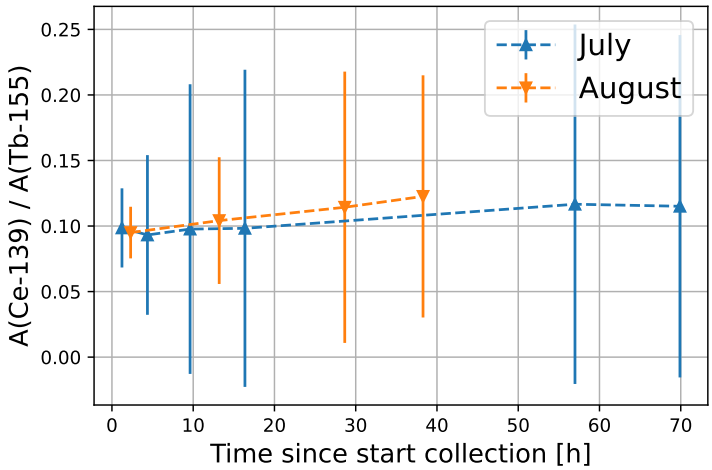

Figure 4.13: Activity ratio of ^{139}Ce to ^{155}Tb as measured by the Kromek GR1 detector, as function of time during the July and August ^{155}Tb collections.

against time in Fig. 4.13 for both the July and August ^{155}Tb collections. From this graph, we note that the ratio fluctuates around 10 %, becoming slightly larger toward the end of the collections. The diminishing purity can be ascribed to the much longer half-life of ^{139}Ce compared to ^{155}Tb: the ^{139}Ce activity remains at a higher level, while the ^{155}Tb already starts to decay. This can also be concluded from the activity trends in Fig. 4.5 for July and Fig. 4.7 for August. Given the slow decrease in purity of the implanted samples, tracking the ^{139}Ce/^{155}Tb activity ratio during a collection might be helpful to determine when the sample becomes too impure with respect to the minimal radionuclidic purity and, related to that, when to stop the collection. However, it is important to point out that the ratios directly determined from measurements of the Kromek GR1 detector include sputtered ^{139}Ce and ^{155}Tb activities. When a detailed investigation is performed on sputtering, perhaps a correction factor can be deduced that gives the implanted ^{139}Ce/^{155}Tb activity ratio from the ratio determined by the Kromek GR1 detector. That would allow even more accurate monitoring of the purity of implanted samples during a collection.

An alternative method to minimise the amount of ^{139}Ce^{16}O implanted together with ^{155}Tb is to irradiate the target at lower proton energies. Fig. 4.14 presents cross section data for the production of ^{155}Tb and ^{139}Ce in tantalum targets, showing that the cross section for ^{155}Tb is maximal around 800 MeV, whereas that for ^{139}Ce is still quite low at this energy and increases steeply for higher proton energies [46]. This opens possibilities for ^{155}Tb production at the future ISOL facility in SCK CEN, ISOL@MYRRHA. The MYRRHA (Multi-purpose hYbrid Research Reactor for High-tech Applications) facility will feature an accelerator-driven system (ADS) research reactor [47], such that it could allow the production of all Tb radioisotopes for medical applications on a single site (using the reactor for ^{161}Tb and the associated ISOL facility for the neutron-deficient isotopes). In the first phase of the project, the linear accelerator will produce a proton beam of 100 MeV. In the second phase, the energy will be extended to 600 MeV [47]. Given the cross sections for ^{155}Tb and ^{139}Ce production at 600 MeV (see Fig. 4.14), this phase would be very well-suited for high-purity production of ^{155}Tb.

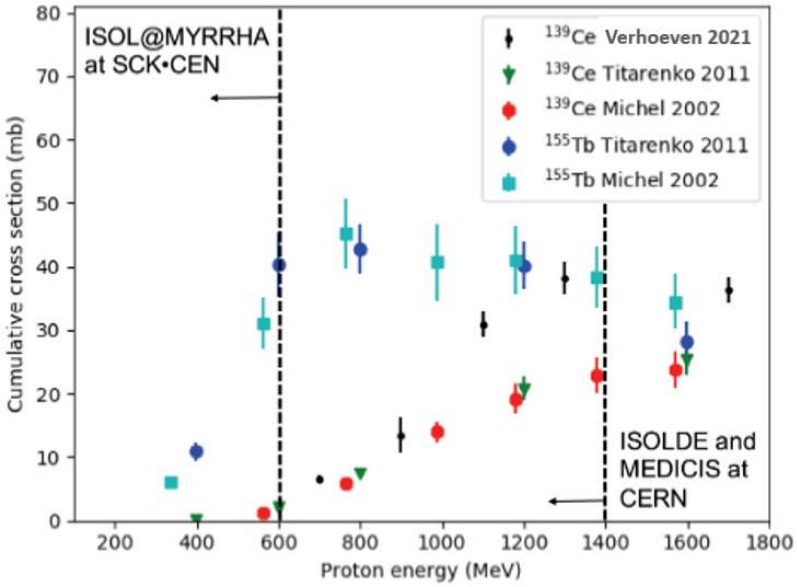

Figure 4.14: Cross sections for the production of ^{155}Tb *and* ^{139}Ce *in tantalum targets as function of the incident proton energy. Image adapted from Ref. [46].*

4.3 Conclusion & Outlook

The analysis of the three ^{155}Tb collections at MEDICIS in 2021 allows to draw some general conclusions about the production of ^{155}Tb as well as the other neutron-deficient Tb isotopes (^{152}Tb and ^{149}Tb) for medical applications. Firstly, it is observed that Tb needs very high temperatures (i.e. above 2000 °C) to effuse out of the target efficiently. Tb also tends to come out more easily when some time is given for other radioisotopes to be extracted from the target or to decay. The possibility of target conditioning prior to the collection therefore proves to be an asset of off-line facilities such as MEDICIS compared to on-line facilities for the production of ^{155}Tb. For ^{152}Tb ($T_{1/2} = 17.5(1)$ h [24]) and especially ^{149}Tb ($T_{1/2} = 4.118(25)$ h [24]), on the other hand, the need for target conditioning poses difficulties, because of their short(er) half-lives. One possible solution might be to produce them at the upcoming ISOL@MYRRHA facility, where fewer other radioisotopes are expected to be produced by the 600 MeV protons. Another outcome of the analysis of the ^{155}Tb collections, is that resonance laser ionisation can improve the Tb yield significantly. Nevertheless, when there are too many ions (e.g. at very high temperatures), the ion source gets saturated and there is no laser enhancement anymore, leading to a reduced Tb yield. To optimise the collection efficiency, the onset of saturation must naturally be avoided. What must also be avoided is sputtering. So far, the understanding of the mechanism of sputtering is limited, so further research on this topic is required. Next year, simulations will be performed in the group of prof. T.E. Cocolios, in order to estimate whether self-sputtering will have a significant effect in a particular collection. Finally, an important conclusion specific to the production of ^{155}Tb for medical applications, is that – with the current configuration at MEDICIS – chemical purification of the samples is always required to get rid of the isobaric contaminant ^{139}Ce^{16}O.

Based on these general conclusions, a revised protocol for Tb collections at MEDICIS is put forward:

- First of all, it is important to perform measurements with the Kromek GR1 CZT detector both immediately before and after any collection. The former allows to determine the background radiation, including any sputtered radioisotopes from previous collections. The latter provides information on the sputtering that occurred during the collection itself.

- Secondly, two quantities should be monitored continuously throughout the whole collection: the ion current and the collected activity. Both are affected by changes in target temperature, saturation of the ion source etc., making them suitable indicators for the progress of the collection. In particular, tracking the collected activity with the Kromek GR1 detector can be helpful to decide when to stop the collection (e.g. when the activity stagnates, or when the sample becomes too impure).

- Finally, it is worthwhile to carefully document all collections in operation reports [48]. The importance of data mining is especially illustrated by the ^{155}Tb collection from October 2021, where it proved very difficult to determine what caused the lack of ^{155}Tb during that collection with the limited information available.

As closing remark on this chapter, it is important to look back on the role of the Kromek GR1 CZT detector at MEDICIS. Although high precision γ-spectrometry is performed with a HPGe detector after each collection, the CZT detector has proven itself very valuable. Thanks to its compact size, it can be positioned right in front of the collection chamber, thereby allowing to track the activity that is being collected in live time.

Part III

Case Study 2: Waste Management at PARTICLE

Chapter 5

Radioactive Waste in Hadrontherapy

In the second case study of the use of Kromek CZT detectors for nuclear applications in medicine, a Kromek GR05 detector is employed in the context of waste management at the proton therapy facility PARTICLE in Leuven. Besides intentional nuclear reactions, such as for the production of medical radioisotopes (cf. part II), nuclear reactions also occur as undesired side effects in various circumstances. In proton therapy facilities, radioactivity is generated in construction materials of the beam-line by proton-induced reactions with protons that scatter out of the therapeutic beam. This leads to the production of radioactive waste, which must be handled carefully. To determine how to treat specific pieces of waste, one has to which radioisotopes are produced in them and what their respective activities and half-lives are. To that end, the simulation software FLUKA and a Kromek GR05 CZT detector are used throughout the following chapters. The aim is to guide waste management of cyclotron parts from the PARTICLE facility. In chapter 6, a few straightforward FLUKA simulations are considered, to get an idea of which radioisotopes to expect. Chapter 7 presents an extensive spectroscopic study of 12 proton-activated cyclotron parts. However, before turning to those analyses, the present chapter provides some background information. Section 5.1 gives a general introduction to the main concepts of proton therapy and the overarching class of hadrontherapy as cancer treatment. Thereafter, in section 5.2, the implementation of proton therapy at the PARTICLE facility is described. Finally, section 5.3 provides all the necessary information on the production and management of radioactive waste in the context of hadrontherapy.

5.1 Introduction to Hadrontherapy

Hadrontherapy is a form of external beam radiation therapy, where a tumour is irradiated with protons or heavy charged particles (such as carbon ions) [49, 50]. As in conventional radiotherapy with photons, the incoming particles deposit energy in the tissues they traverse. The energy deposition causes damage to the DNA of the irradiated cells, finally leading to cell death. The main difference between hadrontherapy and conventional radiotherapy lies in the distribution of the dose (i.e. the average energy absorbed per unit mass) throughout the tissue. For protons and heavy ions, the dose-depth profile exhibits a sharp peak, called the “Bragg peak”, whereas for photons it follows a much broader

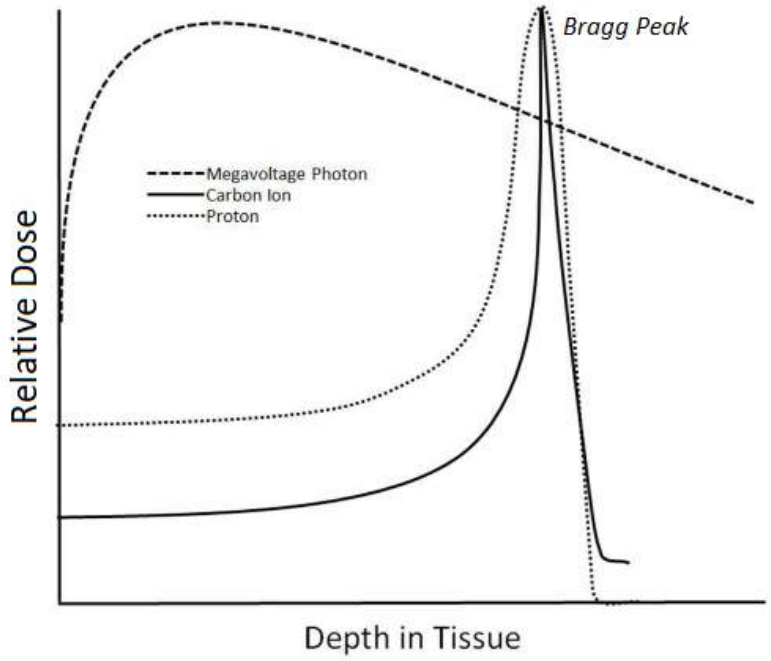

Figure 5.1: Dose-depth distribution for protons, carbon ions and high-energy photons. Image adapted from Ref. [50].

curve. This is illustrated in Fig. 5.1. The depth at which the Bragg peak occurs depends on the energy of the incident particles, so the peak dose can be administered to the tumour by adjusting the energy to correspond to the tumour position. As such, the Bragg peak represents a major advantage of hadrontherapy over conventional radiotherapy, because it limits the dose – and thus radiation damage – delivered to healthy tissue lying in front of and behind the tumour [49, 50]. In the case of protons, the dose drops to zero almost immediately after the Bragg peak, thereby eliminating dose deposition behind the tumour all together. For heavy ions, this does not hold, because they can undergo fragmentation after interactions in the tissue. The lighter ions generated in these reactions have a larger range, and thus cause a so-called "dose-tail" beyond the Bragg peak [50, 51]. On the other hand, the relative dose in front of the tumour is diminished when using heavy ions instead of protons, as the Bragg peak becomes narrower. This effect can be explained by the fact that scattering in tissues becomes less pronounced with increasing mass of the incoming particles ($\propto 1/\sqrt{m}$) [49]. Overall, the benefits of the Bragg peak in terms of sparing healthy tissue surrounding a tumour make hadrontherapy particularly valuable in treatments of young patients and of tumours that are located close to sensitive organs [52].

To generate beams of protons or heavy ions, a hadrontherapy facility requires a particle accelerator. Mostly synchrotrons or cyclotrons are used, although linear accelerators (linac's) are possible as well. In a synchrotron, the particles can be accelerated up to variable energies. Cyclotrons, on the other hand, always accelerate them up to the maximum energy for which they are designed [49]. Therefore, an intricate energy selection system is essential in these cases, to establish the appropriate beam energy for treatment. The energy selection system generally consists of a variable energy degrader followed by a collimator and divergence slits to restore the initial beam quality [53, 54]. After passing through these components, the particle beam is guided to the treatment delivery unit or

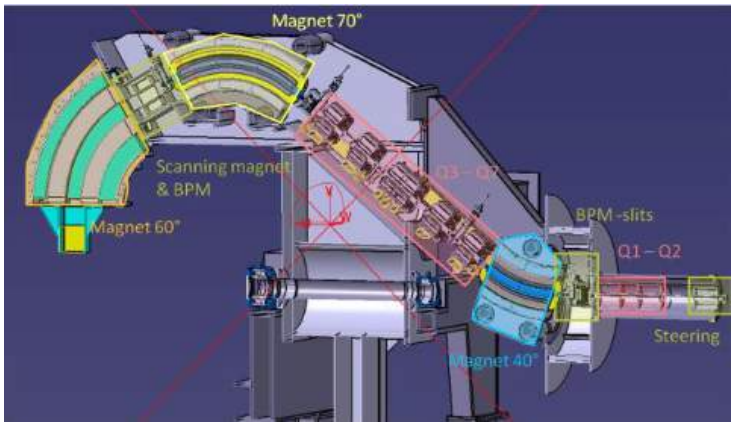

Figure 5.2: Diagram of the gantry that directs the particle beam to the patient. Ref. [54].

"gantry" by beam transport channels. A schematic drawing of the gantry is shown in Fig. 5.2. It is a large structure containing steering and scanning magnets and a nozzle to precisely aim the beam at the patient. To match the dose distribution delivered by hadrontherapy to the shape and volume of the tumour in question, two types of techniques can be implemented in the gantry: passive scattering and active scanning [50, 53]. In the first case, the particle beam is shaped laterally by a collimator and distally by a range modulator. The range modulator effectively generates a "spread out Bragg peak" (SOBP) that covers the complete thickness of the tumour at once. In active scanning the tumour volume is irradiated spot-by-spot with a very narrow beam, called a "pencil beam". Different depth layers of the tumour are selected by varying the energy of the incident particles, and each layer is scanned over by steering the pencil beam with scanning magnets [53]. By adjusting the beam intensity per irradiated spot, the dose distribution throughout the tumour can be tailored, allowing intensity-modulated proton therapy (IMPT). Finally, the gantry can rotate around the patient, such that irradiation from different angles is possible [49, 54]. To ensure that the beam is delivered reliably to the tumour site at each angle, accurate positioning of the patient is crucial. Therefore, hadrontherapy facilities are well-equipped with various imaging technologies in addition to the therapeutic device [49, 52].

5.2 The PARTICLE Facility at UZ Leuven

At the moment of writing, there are 116 hadrontherapy facilities in clinical operation worldwide [55]. One of them is the proton therapy facility PARTICLE (Particle Therapy Interuniversity Centre Leuven) at the University Hospitals Leuven. The facility is operational since the summer of 2020 and is currently[1] the only hadrontherapy facility in Belgium [52]. Located on the Health Sciences campus Gasthuisberg, PARTICLE forms a fully integrated part of the radiotherapy-oncology department of UZ Leuven, and optimal cooperation with the medical imaging research centre, the nuclear medicine department and other (supporting) services is established [53, 57].

[1] A second Belgian proton therapy centre is commissioned to be built in the University Hospital of Charleroi (Hospital Marie Curie) [56].

(a) Layout of the Proteus®ONE setup. Ref. [53].

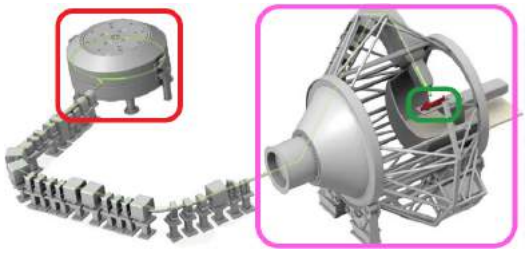

(b) Chain of components making up the proton therapy system. Ref. [58].

Figure 5.3: Overall design of the proton therapy bunker (a) and schematic overview of the main components of the therapy device (b) used at PARTICLE. The colours indicate the accelerator (red), energy selection system (yellow), gantry (pink) and patient (green).

The proton treatments at PARTICLE are performed using the Proteus®ONE system supplied by IBA (Ion Beam Applications). The design of the treatment room is shown in Fig. 5.3, alongside a schematic of its main components (i.e. proton accelerator, energy selection system, beam transport channels and the gantry). Proteus®ONE presents a compact single-room proton therapy technology, equipped with state-of-the-art modalities for proton beam delivery as well as in-room imaging [59]. For example, a "cone beam computed tomography" (CBCT) device is integrated into the Proteus®ONE framework, to improve patient position verification and monitoring. In combination with the advanced X-ray imaging modalities, that allows for image-guided proton therapy (IGPT) [53, 59]. Furthermore, the gantry is designed for active pencil beam scanning. Thanks to the compact size of the entire Proteus®ONE unit, it can be quite easily embedded in existing clinics, making proton therapy more accessible. At PARTICLE, two independent units were installed alongside each other. One is for clinical use, the other for research [53].

As proton accelerator, PARTICLE employs a synchrocyclotron of type S2C2 [54, 59]. Since the analyses in chapters 6 and 7 focus on proton-activated parts of the synchrocyclotron, this part of the Proteus®ONE apparatus is described here. Fig. 5.4b gives a technical drawing of the device. The working of a synchrocyclotron is very sim-

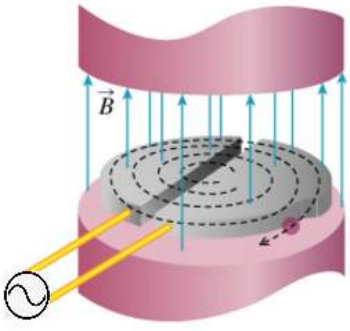

(a) Schematic representation of a cyclotron. Adapted from Ref. [60].

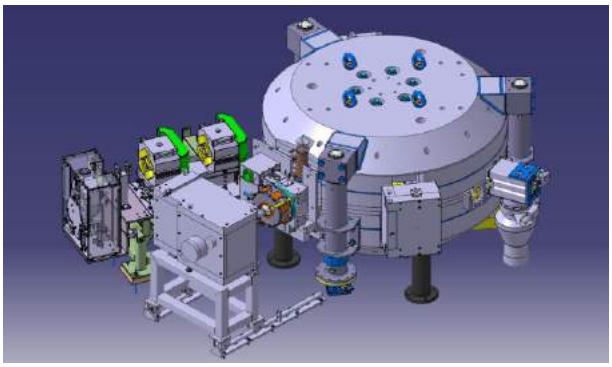

(b) Design of the S2C2 superconducting synchrocyclotron. Scale: ∅ ≈ 2.5 m. Ref. [54].

Figure 5.4: Illustration of the working principle of a (synchro-)cyclotron (a) and blueprint of the S2C2 synchrocyclotron used at PARTICLE (b).

ilar to that of a standard cyclotron, illustrated in Fig. 5.4a. The device is circular and consists of a (superconducting) electromagnet and two hollow D-shaped electrodes. At the centre, there is an ion source that generates protons from neutral hydrogen molecules and subsequently injects them into the accelerator. The paths of the protons inside the electrodes are bent by the homogeneous magnetic field which is generated by the electromagnet. The two electrodes are subjected to an alternating voltage, such that the protons are accelerated by the electric field in the gap between the electrodes. As the protons gain energy each time they pass the gap, the radius of their orbit increases. This leads to a spiral motion toward the outer edge of the cyclotron. There, the protons are extracted at a fixed maximum energy. At PARTICLE, that maximum is 230 MeV [54, 59]. For such high proton energies, relativistic effects become important. In the synchrocyclotron, they are compensated for by gradually decreasing the frequency of the alternating voltage between the two electrodes in the accelerator. Note that this is what distinguishes the synchrocyclotron from a standard cyclotron. The decreasing frequency means that the synchrocyclotron must work in cycles, so only pulsed proton beams can be delivered for therapy. For the device used at PARTICLE, the pulse rate is 1000 Hz [54]. Other specifics of the S2C2 synchrocyclotron can be found in Ref. [54].

5.3 Waste Production & Management

In any hadrontherapy facility, radioactive waste is generated by interactions of the energetic particle beam with construction materials. Some materials are irradiated directly, such as the energy degrader and beam-stopping elements. Construction materials that are not in the beam path can be irradiated indirectly by particles that scatter out of the beam. This can happen at any point during the production and transport of the particle beam. In all cases, the incident particles induce nuclear reactions in the construction materials, leading to a variety of radioisotopes being produced. Which radioisotopes are generated in a specific case depends on the composition of the irradiated material as well as the type and energy of the incident particle. Construction materials which are directly irradiated interact with the full beam at maximal intensity and energy. For indirect irradiation, in contrast, both quantities are considerably lower as a result of scattering. Hence, the radioactivity generated under such circumstances is expected to be lower. Nevertheless, there is still a significant amount of radioactivity produced, so virtually all construction materials should be considered radioactive waste, when they are taken out of the installation.

Any form of radioactive waste must be handled very carefully, in order to guarantee the safety of the public against the risks of ionising radiation. Accordingly, there are many regulations that in detail prescribe the management of radioactive waste. The International Atomic Energy Agency (IAEA) puts forward a recommended classification system that divides radioactive waste into three categories, namely low-, medium- and high-level waste, based on the half-life and activity of the radioisotopes present in it [61]. Waste processing and long-term management procedures are to be determined for each category separately on a national level. Additionally, there are “clearance levels”, which define a total activity or activity concentration below which a piece of waste may be exempted from regulatory control and disposed of or recycled [62, 63]. In Belgium, clearance levels

were fixed for an extensive list of radioisotopes in the royal decree ARBIS (Algemeen Reglement op de Bescherming van de bevolking en de werknemers tegen het gevaar van Ioniserende Stralingen) of July 20, 2001 (see Ref. [63]). For solid waste containing a mixture of radioisotopes,

$$\sum_j \frac{a_j}{C_j} \leq 1 \tag{5.1}$$

must hold for clearance, where a_j represents the activity concentration of radioisotope j in the sample, and C_j is the clearance level corresponding to that radioisotope [63]. All radioactive waste above the appropriate clearance levels is subject to the supervision of the governmental agency FANC (Federaal Agentschap voor Nucleaire Controle) and the institution NIRAS (Nationale Instelling voor Radioactief Afval en verrijkte Splijtstoffen) [61, 64]. NIRAS is responsible for the management of all radioactive waste in Belgium, be it spent fuel from nuclear power plants, medical waste or any other type. With respect to medical waste, NIRAS allows some (short-lived) radioactive waste to be kept in storage at the hospitals themselves [65]. However, this makes it harder to keep track of all radioactive waste. In that light, NIRAS is required to make an inventory of all sites containing radioactive materials every five years [61].

Given that the classification system as well as the clearance levels are based on the activity and/or half-life of the radioactive waste, the first crucial step in radioactive waste management is to determine these characteristics for the waste at hand. This is achieved using the Kromek GR05 CZT detector: by performing γ-spectrometry on the waste materials, one can identify as well as quantify the radioisotopes that are present. Apart from γ-spectrometry, FLUKA simulations can be valuable as well: by modelling the particle beam and its environment, it becomes possible to numerically predict which radioisotopes are created in which amounts in the construction materials. Both approaches are put into practice throughout the following chapters for the purpose of waste management of cyclotron parts from the PARTICLE facility.

Chapter 6

FLUKA Simulations

This chapter discusses a few elementary simulations of the irradiation of bulk materials by a 230 MeV proton beam. The aim is to get a qualitative idea of which radioisotopes are expected to be found in the synchrocyclotron parts from the PARTICLE facility. Materials that are commonly used in accelerators were considered, namely aluminium, AlMgSi, stainless steel and copper. Al, AlMgSi and stainless steel form parts of the scaffolding, whereas Cu is typically used as a conductor (for both electricity and heat). The thickness of all samples was taken to be 2 cm. This value was chosen, because it is of the same order of magnitude as the thicknesses of the cyclotron parts from PARTICLE (except for the cooling cylinders) (see later). Regarding the proton beam characteristics, the beam current was set to 1 nA. This is the average current of the beam at PARTICLE, as reported by the radio-protection team from UZ Leuven. The radioisotopes and their respective activities generated in the samples were evaluated with FLUKA 1 hour, 1 day, 1 month, 6 months and 1 year after the end of the irradiation. Besides FLUKA simulations, also SRIM (Stopping and Range of Ions in Matter) simulations were performed, in order to calculate the energy loss of the proton beam inside the bulk materials [66]. This was done because the energy range of the protons inside the samples limits the nuclear reactions that can occur (see section 1.2.1). The SRIM simulations were carried out by M. Heines.

6.1 Aluminium & AlMgSi

The first material considered is aluminium. FLUKA and SRIM simulations were performed for pure Al as well as AlMgSi consisting of 99 wt% Al, 0.5 wt% Mg and 0.5 wt% Si [67]. Given the low fractions of magnesium and silicon in AlMgSi, the outcomes were expected to be very similar. The results of the SRIM simulations for the energy loss of 230 MeV protons inside 2 cm pure Al and AlMgSi are illustrated in Fig. 6.1. For both materials, the energy distribution of the protons after passing through the sample approaches a Gaussian centred around approximately 212 MeV. Consequently, the energy range within which nuclear reactions can occur inside the samples is rather limited. The reactions were simulated by FLUKA, yielding the generated radioisotopes and their respective activities for both samples. The results are given in Fig. 6.2 for pure Al and Fig. 6.3 for AlMgSi. As expected, the same radioisotopes are found in Al

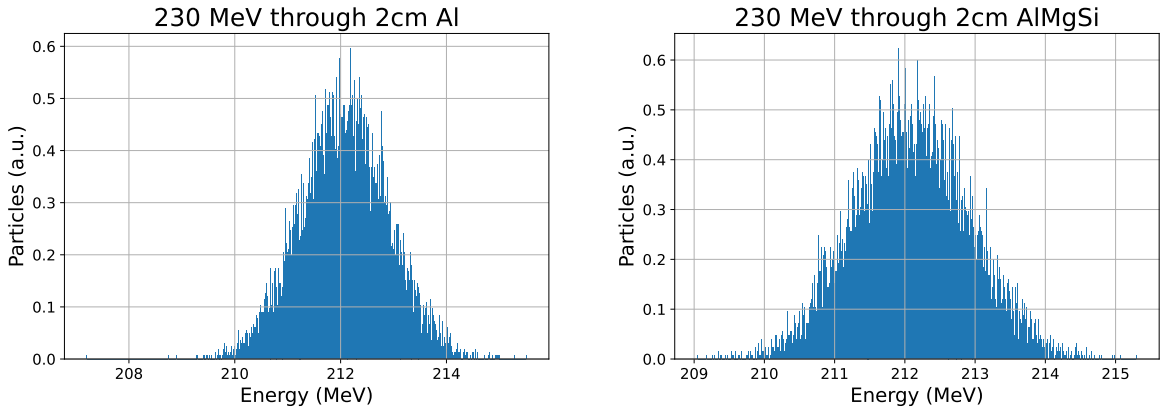

(a) Pure Al sample. *(b) AlMgSi sample.*

Figure 6.1: Energy distribution of the 230 MeV *proton beam after passing through* 2 cm *of Al (a) and AlMgSi (b).*

and AlMgSi. The activities are overall slightly higher in AlMgSi, due to the additional production pathways via proton-induced reactions on Mg or Si. For both materials, it is observed that ^{22}Na ($T_{1/2} = 2.6018(22)$ y [24]) is the radioisotope with the highest activity in the long term. In contrast, shortly after the irradiation, other isotopes (such as ^{24}Na ($T_{1/2} = 14.997(12)$ h [24])) reach activities much higher than that of ^{22}Na. Hence, the most active radioisotope in the sample changes in time. That has to do with the distinct half-lives of all the generated nuclei. In general, many different radioisotopes are produced, but only the long-lived ones can maintain high activities in the sample for a very long time. In the context of waste management, it is essential to know which radionuclei dominate at different timescales, in order to select the appropriate disposal procedure. For Al and AlMgSi, it seems that ^{22}Na will be the most important isotope to take into account toward long-term waste management. Whilst there are even longer-lived radioisotopes such as ^{3}H ($T_{1/2} = 12.32(2)$ y [24]) and ^{26}Al ($T_{1/2} = 7.17(24) \times 10^5$ y [24]), they are

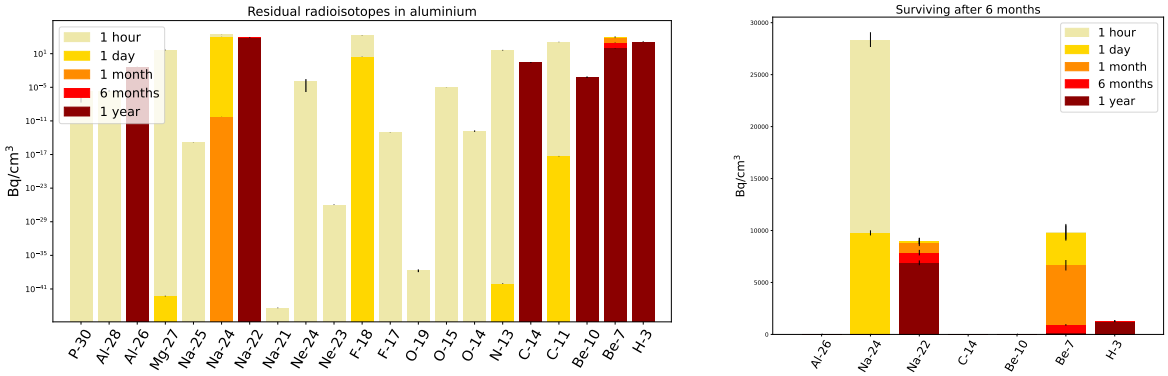

(a) Residual activities after 1 hour, 1 day, 1 month, 6 months and 1 year in logarithmic scale. *(b) Activities of the most long-lived isotopes in linear scale.*

Figure 6.2: Predicted residual activities [Bq/cm^3] *of generated radioisotopes in Al after irradiation by a* 230 MeV *proton beam. Note that the left graph is in logarithmic scale, whereas the right graph shows the residual activities of those radioisotopes that survive up to 6 months or longer in linear scale, to highlight the absolute differences.*

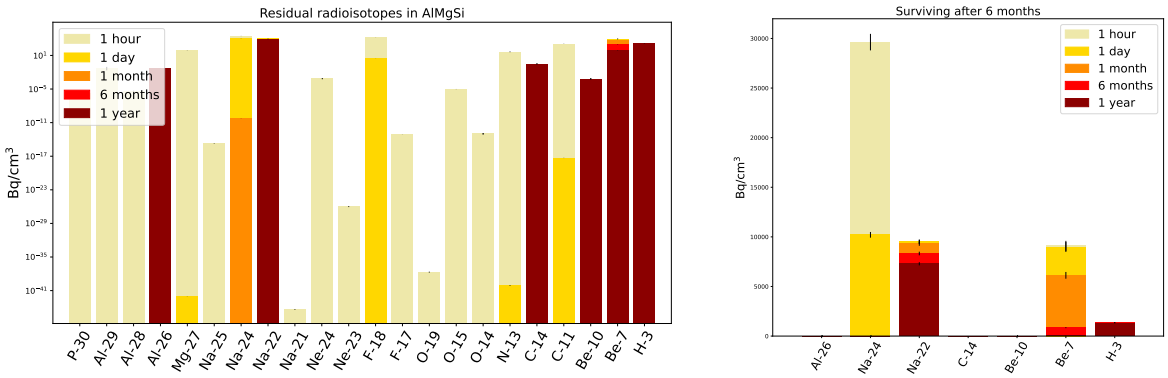

(a) Residual activities in logarithmic scale. *(b) Most long-lived in linear scale.*

Figure 6.3: Predicted residual activities [Bq/cm^3] *of generated radioisotopes in AlMgSi after irradiation by a* 230 MeV *proton beam. Again, the right graph shows the radioisotopes that survive up to 6 months or longer in linear scale, to highlight the absolute differences.*

present in much smaller amounts and accordingly pose less risks in regards to radiation protection. Nevertheless, they must still be taken into consideration (e.g. in checking whether the total activity satisfies the clearance condition).

To gain insight into the results from FLUKA, it is important to consider a few potential reaction mechanisms that produce the predicted radioisotopes. Not only does this clarify how the predicted nuclei are generated in the sample, it also helps to understand why certain other nuclei are not observed even though they are expected to be produced in the same types of reactions. Fig. 6.4 illustrates four plausible reaction pathways in Al and AlMgSi on the nuclear chart. All reactions start from the absorption of a proton by stable isotopes of Al (^{27}Al), Mg (^{24}Mg, ^{25}Mg, ^{26}Mg) or Si (^{28}Si, ^{29}Si, ^{30}Si). Nuclei with atomic numbers only a few units away from that of the initial element are presumably generated by reactions such as (p, n), (p, d) with d signifying a deuteron (i.e. 1 proton and 1 neutron combined), (p, α) and similar. Starting from stable ^{27}Al, for example, possible reactions include $^{27}\mathrm{Al}(p, n)^{27}\mathrm{Si}$, $^{27}\mathrm{Al}(p, d)^{26}\mathrm{Al}$ and $^{27}\mathrm{Al}(p, \alpha)^{24}\mathrm{Mg}$. Of the product

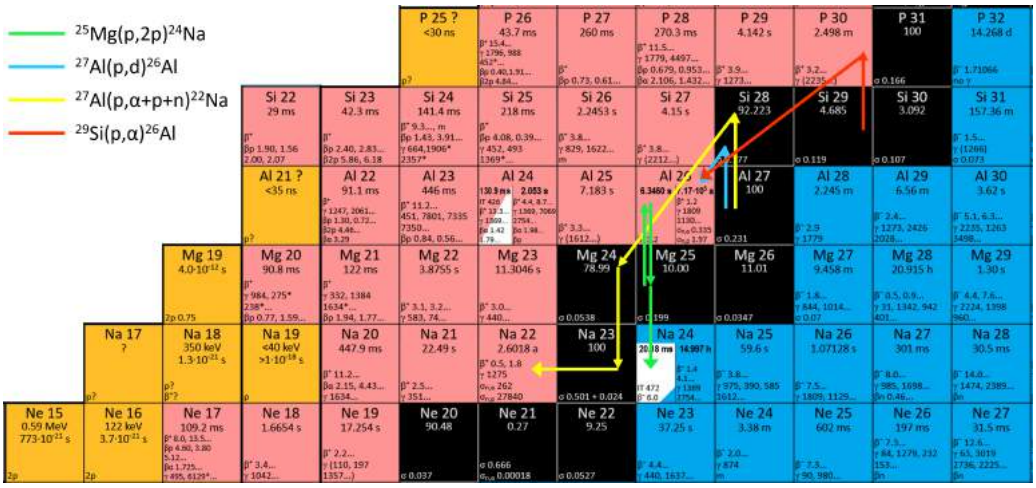

Figure 6.4: Illustration of four proton-induced reactions that generate radioisotopes predicted by FLUKA starting from stable Al, Mg and Si isotopes. Nuclear chart from Ref. [3].

nuclei, only ^{26}Al is predicted by FLUKA to contribute to the long-term radioactivity in the sample. Looking at the nuclear chart, that makes sense since ^{24}Mg is stable and ^{27}Si has a half-life of only 4.15(4) s [24], so it completely disappears 1 hour after the irradiation. As another example, consider (p, α) reactions on the stable Mg isotopes: ^{24}Mg$(p, \alpha)^{21}$Na, ^{25}Mg$(p, \alpha)^{22}$Na and ^{26}Mg$(p, \alpha)^{23}$Na. In this case, of the product nuclei only ^{22}Na appears in Fig. 6.2 and Fig. 6.3, because ^{23}Na is stable and ^{21}Na has a half-life of only 22.49(4) s [24]. More than one proton, neutron, deuteron or α-particle, or a combination of them may also be released. This is observed, for example, in the reaction ^{27}Al$(p, \alpha + p + n)^{22}$Na [12]. Note that the cross section data for that specific reaction was given in Fig. 1.3 of section 1.2.1 on proton-induced reactions. Finally, besides elementary particles and the stable deuteron and α-particle (i.e. ^{4}He nucleus), also light radionuclei can be emitted. Examples include ^{27}Al$(p, ^7\text{Be})^{21}$Ne and ^{28}Si$(p, ^3\text{H})^{26}$Si [12]. These types of reactions are responsible for the production of ^{7}Be ($T_{1/2} = 53.22(6)$ d [24]) and ^{3}H ($T_{1/2} = 12.32(2)$ y [24]) predicted by FLUKA. Whether the heavier product nuclei of the reactions contribute to the radioactivity in the samples depends on their respective half-lives. For the two given examples, neither ^{21}Ne nor ^{26}Si contributes in the long term, because the former is stable and the latter has a short half-life of 2.2453(7) s [24].

6.2 Stainless Steel

Besides Al and AlMgSi, stainless steel is also commonly used in the construction of accelerators. Therefore, FLUKA and SRIM simulations were performed for this material as well. Stainless steel is an alloy consisting predominantly of iron and chromium, enriched with other metals (such as nickel) to improve mechanical properties [68]. Depending on chemical composition, several types of stainless steel with distinct physical properties are distinguished. For the simulations in this thesis, the atomic content was taken to be 74 % Fe, 18 % Cr and 8 % Ni [68]. The outcome of the SRIM simulation for the energy loss of 230 MeV protons in 2 cm stainless steel is illustrated in Fig. 6.5. The energy distribution of the protons after passing through the sample approaches a Gaussian centred around 180 MeV. Thus, the average energy loss is significantly larger than in Al or AlMgSi, which

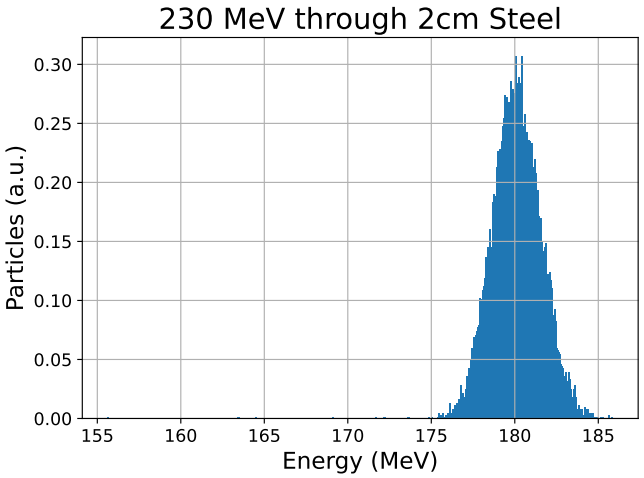

Figure 6.5: Energy distribution of 230 MeV *protons after passing through* 2 cm *of stainless steel.*

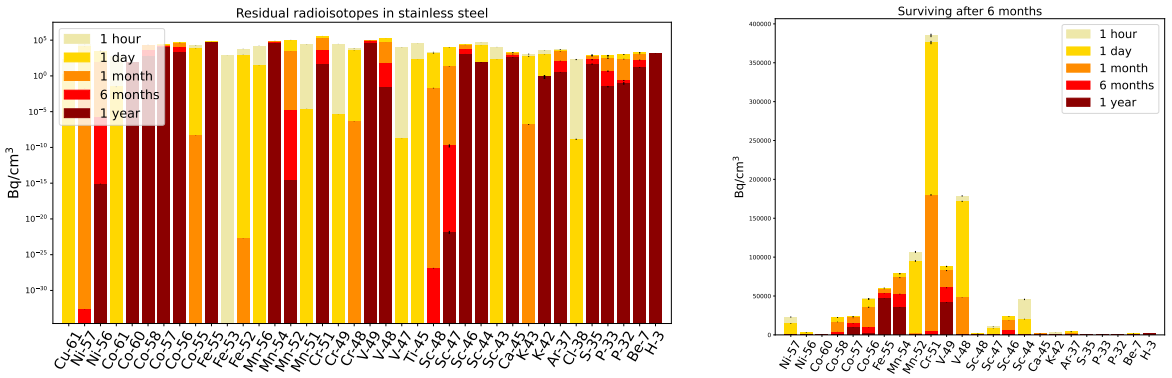

(a) Residual activities in logarithmic scale. *(b) Most long-lived in linear scale.*

Figure 6.6: Predicted residual activities [Bq/cm^3] *of generated radioisotopes in stainless steel after irradiation by a* 230 MeV *proton beam.*

can be explained by the higher masses – and therefore larger stopping powers – of the elements Fe, Cr and Ni compared to Al, Mg and Si. The greater energy loss in stainless steel implies that there is a wider range of proton energies at which nuclear reactions can occur in the sample. The radioisotopes that are produced in the numerous reactions that take place, are determined by the FLUKA simulation of the irradiation process. The results are given in Fig. 6.6. Firstly, it is observed that there are substantially more and heavier radioisotopes in stainless steel, in comparison to Al and AlMgSi. This follows from the fact that stainless steel is made up of heavier elements, such that the proton-induced reactions generate heavier products. The radioisotopes with the highest residual activities after 6 months to 1 year since the irradiation, are ^{55}Fe ($T_{1/2} = 2.744(9)$ y [24]), ^{49}V ($T_{1/2} = 330(15)$ d [24]), ^{54}Mn ($T_{1/2} = 312.20(20)$ d [24]) and ^{57}Co ($T_{1/2} = 271.74(6)$ d [24]). At shorter timescales, ^{51}Cr ($T_{1/2} = 27.704(4)$ d [24]) assumes the role of the most active radioisotope, but due its shorter half-life, it decays to a minor activity in the long term.

Figure 6.7: Illustration of six reaction pathways that generate radioisotopes predicted by FLUKA starting from stable Fe, Cr and Ni isotopes. Nuclear chart from Ref. [3].

The reactions that produce the radioisotopes predicted by FLUKA in stainless steel are expected to be of the same nature as in Al and AlMgSi (i.e. (p, n), (p, α), $(p, \alpha + n)$, $(p, {}^{3}\mathrm{H})$, $(p, {}^{7}\mathrm{Be})$ etc.). Fig. 6.7 illustrates a few examples on the nuclear chart. The number of particles that can be emitted in a single reaction is limited by the energy of the protons inside the sample (see section 1.2.1). In that regard, it makes sense that the FLUKA results in Fig. 6.6 show no radioisotopes between ^{32}P and ^{7}Be: the proton energies are neither high enough for the emission of the considerable amount of nucleons and/or α-particles necessary to reach these isotopes, nor to eject the isotopes themselves in a break-up reaction (like ^{3}H and ^{7}Be). Above ^{32}P, the proton-induced reactions generate a large variety of radioisotopes, even within given elements. Consider, for example, the multitude of cobalt isotopes predicted by FLUKA. From ^{55}Co to ^{61}Co, all isotopes can be produced by (p, Xn) reactions on stable isotopes of Fe (^{54}Fe, ^{56}Fe, ^{57}Fe, ^{58}Fe), and $(p, \alpha + Xn)$ or $(p, 2p)$ reactions on stable Ni isotopes (^{58}Ni, ^{60}Ni, ^{61}Ni, ^{62}Ni, ^{64}Ni). Three possible reactions are shown in Fig. 6.7. Isotopes lighter than ^{55}Co or heavier than ^{61}Co are also generated by these types of reactions, but they do not appear in the FLUKA results in Fig. 6.6, because of their half-lives on the order of a few ms to minutes [24]. Note that ^{59}Co is also not present in Fig. 6.6, because it is stable.

6.3 Copper

The third and last material that was investigated with simulations is copper. As mentioned earlier, Cu is often used in accelerators, as it is a good conductor of both electricity and heat. Considering a sample of 2 cm thickness, the energy distribution of a 230 MeV proton beam after passing through the sample was determined by SRIM to peak between 175 MeV and 180 MeV. The outcome of the simulation is shown in Fig. 6.8. The protons lose more energy in Cu than in stainless steel, which can be explained by the higher mass – and larger stopping power – of Cu compared to Cr, Fe and Ni. As in stainless steel, a large variety of radioisotopes is produced upon proton irradiation. That can be seen from the results of the FLUKA simulation in Fig. 6.9. Again, the nuclear reactions producing the predicted radioisotopes are expected to be mostly of the

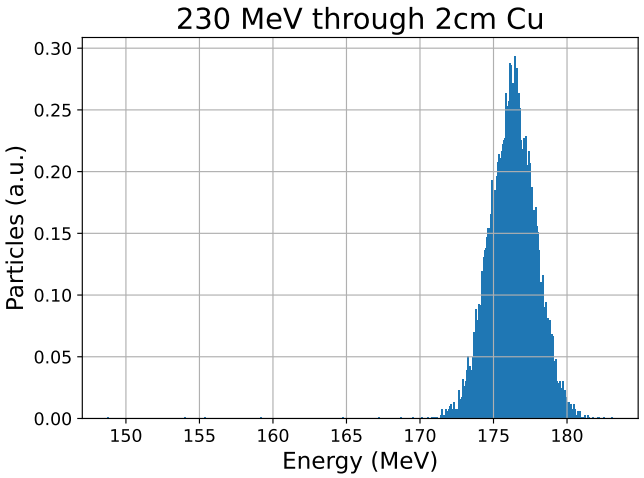

Figure 6.8: Energy distribution of the 230 MeV *proton beam after passing through* 2 cm *of Cu.*

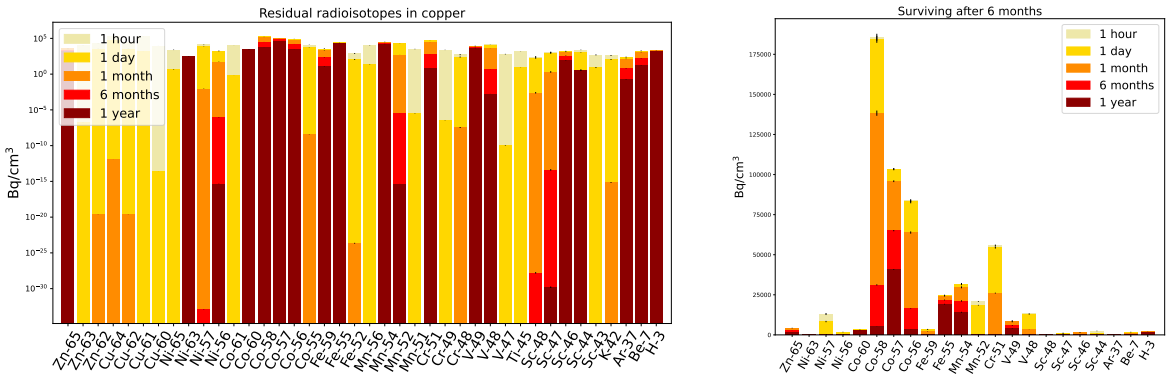

(a) Residual activities in logarithmic scale. *(b) Most long-lived in linear scale.*

Figure 6.9: Predicted residual activities [Bq/cm^3] *of generated radioisotopes in Cu after irradiation by a* 230 MeV *proton beam.*

types (p, n), (p, α), $(p, \alpha + p + n)$ and so forth. Because Cu is heavier than stainless steel, heavier nuclei are produced in these proton-induced reactions. More specifically, Fig. 6.9 shows the presence of Zn radioisotopes and more Cu radioisotopes compared to steel. ^{65}Zn ($T_{1/2}$ = 243.93(9) d [24]) is particularly important, because it remains present in the sample in non-negligible amounts even 1 year after the irradiation. This radioisotope is most likely produced via ^{65}Cu$(p, n)^{65}$Zn, as illustrated in Fig. 6.10. On the other end of the spectrum, the lightest generated radioisotope aside from ^{3}H and ^{7}Be has shifted up from ^{32}P in steel to ^{37}Ar in Cu. Other than that, mostly the same radioisotopes occur in both materials, albeit in very different amounts. The different residual activities are a consequence of the unique cross sections of the proton-induced reactions in stainless steel and Cu, which were evaluated by the FLUKA simulations. In Cu, ^{57}Co ($T_{1/2}$ = 271.74(6) d [24]) is the radioisotope with the highest activity in the long term, followed by ^{55}Fe ($T_{1/2}$ = 2.744(9) y [24]) and ^{54}Mn ($T_{1/2}$ = 312.20(20) d [24]).

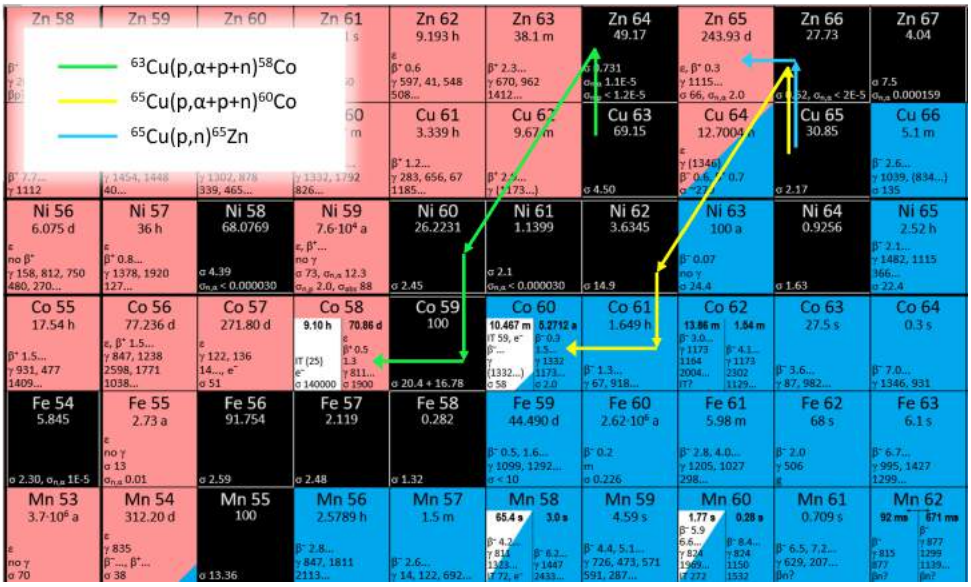

Figure 6.10: Illustration of three reaction pathways that generate radioisotopes predicted by FLUKA starting from stable Cu isotopes. Nuclear chart from Ref. [3].

In the short-term, the Co radioisotopes ^{58}Co ($T_{1/2}$ = 70.86(6) d [24]), ^{57}Co and ^{56}Co ($T_{1/2}$ = 77.236(26) d [24]) dominate. The production of the cobalt isotopes in Cu happens via $(p, \alpha + p + Xn)$ reactions with $X = 1, 2, 3$ on the stable isotopes of Cu (^{63}Cu, ^{65}Cu). Two such reactions are illustrated in Fig. 6.10.

6.4 Conclusion

The goal of the FLUKA simulations of bulk samples discussed in this chapter was to identify which radioisotopes are most likely to be observed during the spectroscopic study of cyclotron parts of the PARTICLE facility (see next chapter). Four commonly used construction materials were investigated, namely Al, AlMgSi, stainless steel and Cu. For each material, the generated radioisotopes and their residual activities were evaluated by FLUKA at regular time intervals after irradiation by a 230 MeV proton beam. As the samples from PARTICLE were subjected to measurements with a CZT detector several months after they were taken out of the accelerator, we review here the results of the FLUKA simulations for 6 months and 1 year after the end of the irradiation. For Al and AlMgSi, ^{22}Na is identified as the dominant radioisotope after 6 months to 1 year after the proton irradiation. In stainless steel and Cu, a wider variety of radioisotopes remain present in significant activities. For both, mostly the same radioisotopes are expected, but in different relative amounts. In stainless steel, ^{55}Fe is the most active radioisotope in the long term, followed by ^{49}V, ^{54}Mn and ^{57}Co. In Cu, on the other hand, the residual activity of ^{57}Co is significantly higher, making this radioisotope the one with the highest activity in the long term. The other three have lower activities in Cu (especially ^{49}V), but do remain present in the relevant timescale for disposal. Besides these radioisotopes, the cobalt isotopes ^{56}Co, ^{58}Co and ^{60}Co have significantly higher residual activities in Cu, and ^{65}Zn is produced in substantial amounts as well.

It is important to point out that the simulations in this chapter present model cases for direct irradiation of materials of known composition by a 230 MeV proton beam. Hence, they provide only qualitative information with respect to the cyclotron parts from PARTICLE, namely which radioisotopes to expect for different types of materials. The absolute (and relative) activities of the generated radioisotopes in the samples depend on the specific irradiation conditions (e.g. position with respect to the beam, duration of the irradiation...). If one wants to accurately predict these quantities for various parts of the accelerator, a FLUKA simulation of the entire synchrocyclotron and its operation at PARTICLE must be made. That was beyond the scope of this thesis.

To conclude this chapter, Fig. 6.11 provides an overview of the most relevant radioisotopes and their relative proportions in each of the four materials that were discussed. Only those isotopes that were detected during the spectroscopic study of the cyclotron parts from PARTICLE are shown individually, to give an idea of which fraction of the total radioactivity could be ultimately detected for each material.

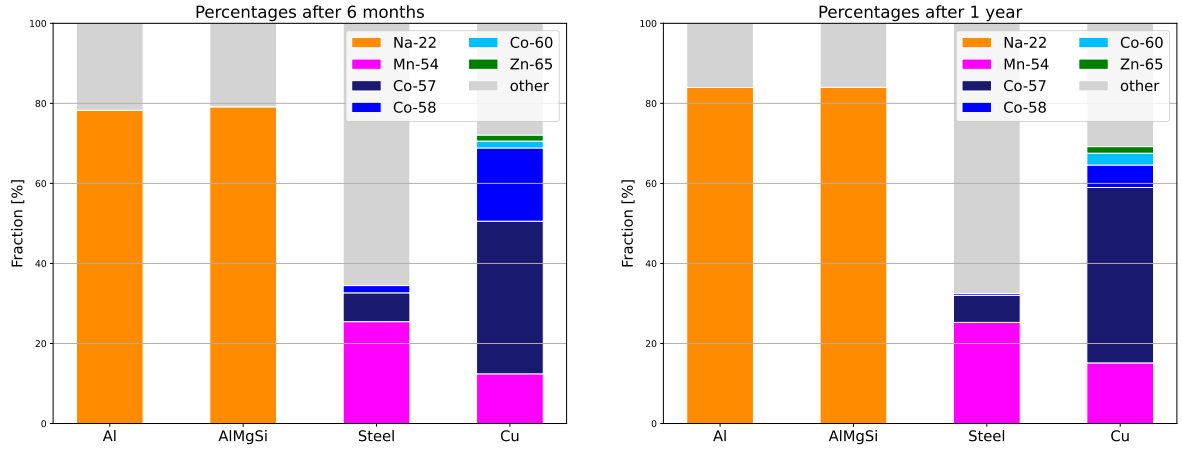

(a) Bar chart for 6 months after irradiation. *(b) Bar chart for 1 year after irradiation.*

Figure 6.11: Fractions of the detected radioisotopes, as determined by FLUKA for Al, AlMgSi, Cu and stainless steel at 6 months (a) and 1 year (b) after irradiation by 230 MeV *protons.*

Chapter 7

Spectroscopic Study of Proton-Activated Materials

Complementary to the FLUKA simulations, a spectroscopic study was performed on 12 proton-activated materials from the proton therapy centre PARTICLE in Leuven. The samples served as various parts of the synchrocyclotron (e.g. beam-stopping element, cooling cylinder etc.), and were thus irradiated by protons of up to 230 MeV (see section 5.2). In order to identify which radioisotopes were present in the different samples and what their respective activities were, γ-ray spectra were acquired for all samples with a Kromek GR05 CZT detector at the Institute for Nuclear and Radiation Physics (IKS) in Leuven. In addition to this experiment, other measurements (e.g. of the dose rate on contact for each of the 12 objects) were performed by R. Driesen. The results and conclusions of his work can be found in Ref. [1]. Here, only the measurements with the Kromek GR05 CZT detector are discussed. The first section of this chapter describes the experimental setup and procedures that were used. In section 7.2, the acquired γ-spectra and the activities calculated from them are given. These results are then discussed in section 7.3. Finally, section 7.4 presents a conclusion on the 12 proton-activated cyclotron parts in the context of waste management.

Before the experiment was started, a comprehensive risk assessment was made. This document, along with the advice provided by the Health, Safety & Environment (HSE) department, is included in appendix C. Appendix D provides an overview of the 12 objects that were studied. Two of them were irradiated directly by the 230 MeV proton beam, whereas the others were not positioned in the beam path and thus only irradiated by scattered protons. Throughout this chapter, the different samples are referred to by unique identification numbers consisting of three letters, a two-digit number and optionally A/B.

7.1 Experimental Setup & Procedure

The setup that was used for the experiment is shown in Fig. 7.1. The Kromek GR05 detector was mounted in front of the sample under investigation. It could be moved over a rail, allowing to change the distance between detector and sample. To provide shielding against radiation from the sample, a lead wall was built in front of the setup. Lead bricks

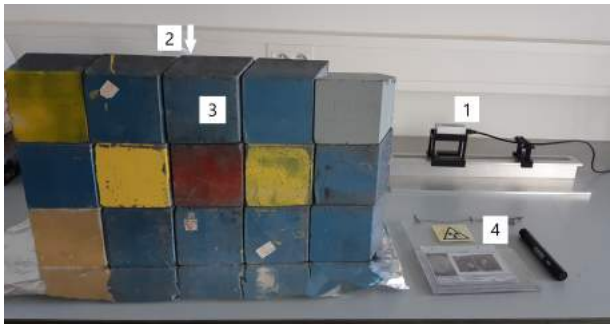

(a) Front view of the setup. The samples were placed behind the lead shielding one by one.

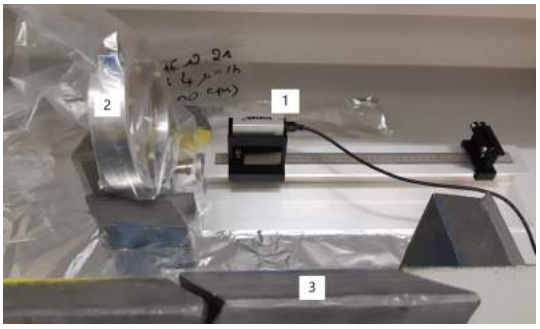

(b) Specific arrangement used for sample PTK42 (see appendix D).

Figure 7.1: Pictures of the experimental setup used for the spectroscopic study. Picture (a) gives the front view of the setup, picture (b) shows the overhead view for a specific case. The different components are indicated: (1) Kromek GR05 CZT detector, (2) sample under study, (3) lead shielding, (4) identification card for the sample in the setup.

were also used to stabilise the sample in the setup. To avoid contamination of the table, the surface of the table was covered by aluminium foil. Furthermore, each sample was put in a sealed plastic bag individually for the same reason.

Whenever a new sample was brought to the setup for measurements, its count rate was measured first with a contamination monitor. The monitor was held over different parts of the sample to determine whether and where there was a hotspot of activity on the object[1]. The CZT detector was then positioned in front of the identified hotspot as close as possible. This was done to ensure the highest possible signal-to-noise ratio for the measurements. Another purpose of the count rate measurement was to guide the decision regarding the duration of the measurements, in order to get good statistics on the acquired spectra. If the measured count rate for a sample was approximately equal to or just above that for the background in the lab (of the order of 10 cps), acquisitions of 10 h were typically taken[2]. On the other hand, for the samples with the highest count rates (up to 900 cps), the acquisition time was limited to 4 h. This time window was chosen, because the count rate on the KSpect acquisition software was much lower than on the contamination monitor, due to the arrangement and efficiency of the CZT detector. Multiple measurements were performed per sample to improve statistics and to be able to follow the decay of the peaks in the spectra over time. Finally, a background spectrum was acquired without any sample in the setup. In order to get good statistics on the background, the measurement was left running for several days. For the analysis, the background was renormalised against the acquisition time of each sample spectrum, before subtracting it.

A thorough characterisation of the Kromek GR05 detector was performed by K. Spoormans for her master's thesis in 2021 (see Ref. [39]). The energy calibration gave the following linear relationship between channel number and energy:

$$E\ [\text{keV}] = 0.7534(9) \times \text{channel} - 0.98(45). \tag{7.1}$$

[1]In a few cases, the hotspot was already marked on the sample by the team from UZ Leuven that was also working on the 12 cyclotron parts (see Ref. [1]). This is shown in appendix D.

[2]Long measurements were possible using a program that automatically starts, stops and saves acquisitions. The code was written by C. Bernerd.

As for the energy resolution and the intrinsic efficiency of the detector, the data were respectively fitted by

$$R(E)\ [\%] = \exp\big(14(8) - 5(4)\cdot\ln E + 0.7(8)\cdot(\ln E)^2 - 0.03(5)\cdot(\ln E)^3\big), \tag{7.2}$$

$$\epsilon_{intr}(E)\ [\%] = \exp\big(-42(7) + 26(4)\cdot\ln E - 4.6(8)\cdot(\ln E)^2 + 0.24(5)\cdot(\ln E)^3\big). \tag{7.3}$$

The intrinsic efficiency reaches a maximal value of about 85 % around 80 keV [39].

7.2 Results

The γ-spectra that were acquired for the 12 synchrocyclotron parts during the experiment are shown in Fig. 7.2. For four samples, namely PTK27A, PTK27B, PTK46A and PTK46B, the γ-spectra overlap with the background, meaning that no radioactivity was detected by the Kromek GR05 detector. For the other samples, the observed peaks in the spectra were assigned using InterSpec, as explained in section 2.4. During the peak assignment, it was important to be aware of and identify the typical features of γ-spectra discussed in section 2.2. For example, most of the peaks are accompanied by a noticeable Compton continuum, due to scattering interactions of the emitted photons in the detector. When there are several intense peaks (such as in Fig. 7.2a, Fig. 7.2b and Fig. 7.2c), the Compton continua add up, such that the obtained spectrum is higher than the background, with the effect increasing towards low energies. Another common feature of γ-spectra that is observed in several of the spectra, is a backscatter peak between 200 keV to 250 keV. The backscatter peaks display considerable tails on the the high energy side

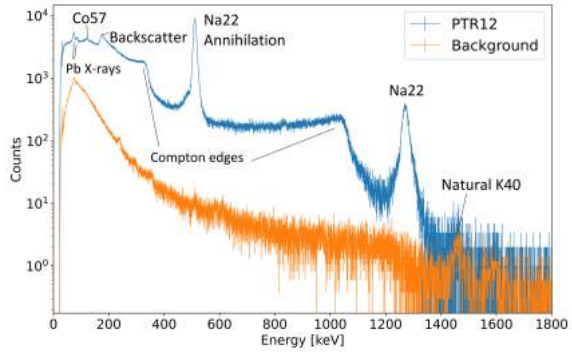

(a) Spectrum for PTR12.

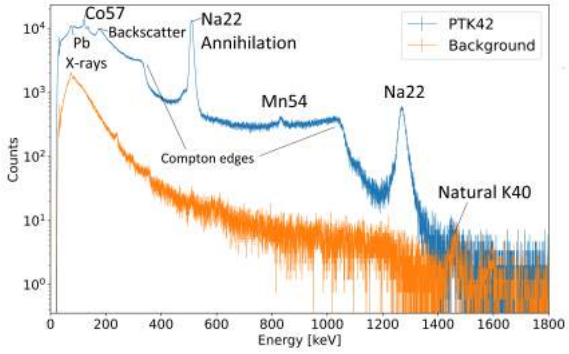

(b) Spectrum for PTK42.

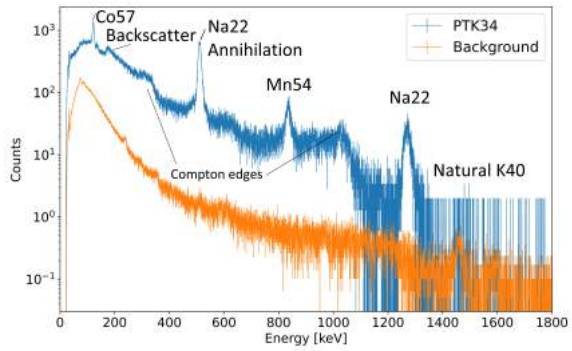

(c) Spectrum for PTK34.

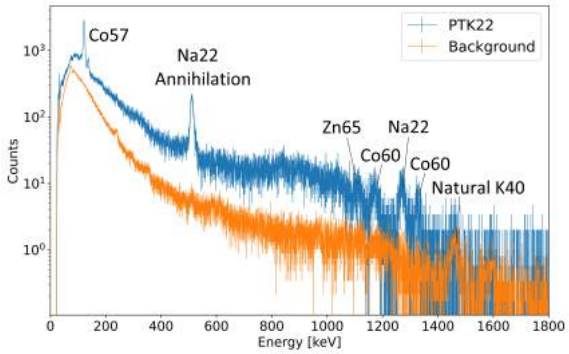

(d) Spectrum for PTK22.

Figure 7.2: Spectra obtained for the 12 cyclotron parts together with the background.

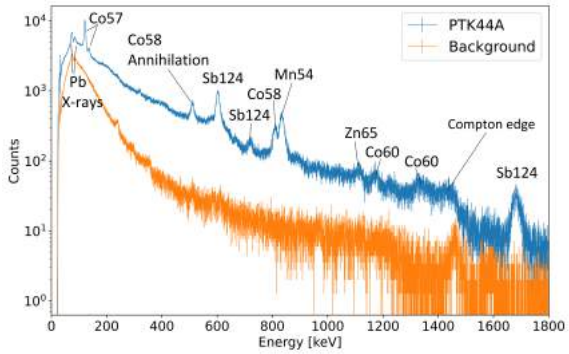

(e) Spectrum for PTK44A.

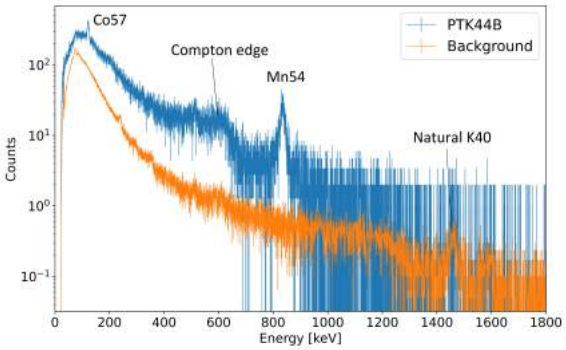

(f) Spectrum for PTK44B.

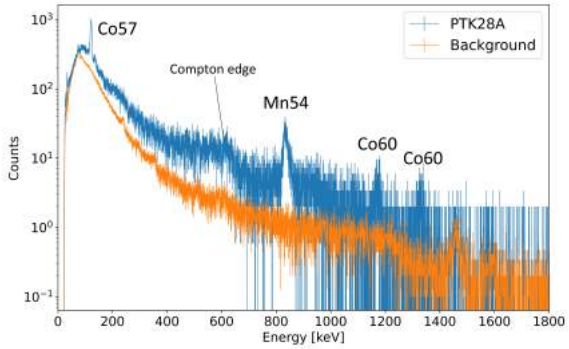

(g) Spectrum for PTK28A.

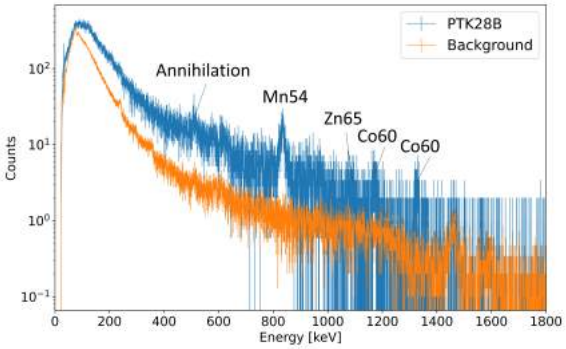

(h) Spectrum for PTK28B.

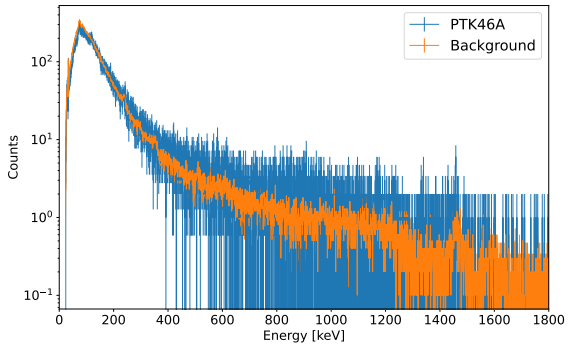

(i) Spectrum for PTK46A.

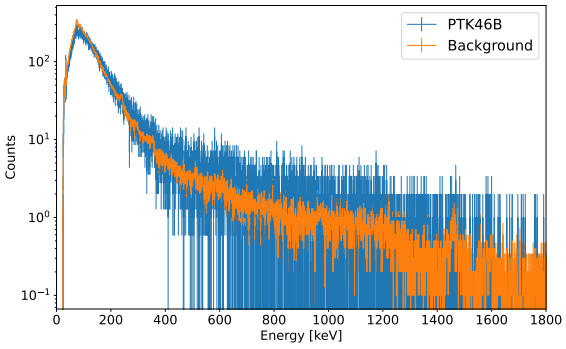

(j) Spectrum for PTK46B.

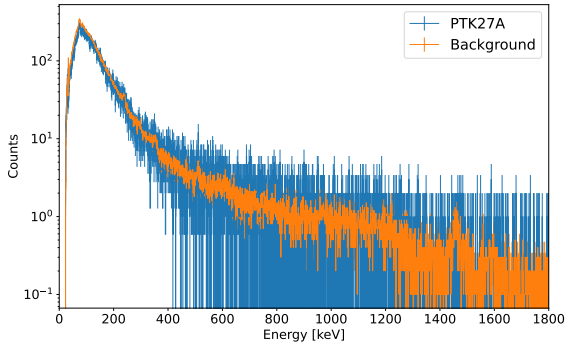

(k) Spectrum for PTK27A.

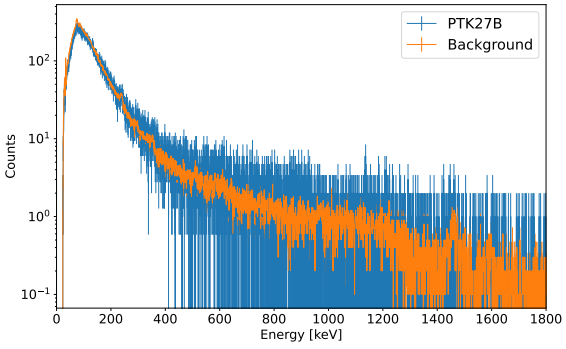

(l) Spectrum for PTK27B.

Figure 7.2: Spectra obtained for the 12 cyclotron parts together with the background (cont.).

of the spectra, because of the different angles at which the photons are scattered. Finally, X-rays from the lead surrounding the experimental setup are observed in all spectra – although most prominently in the spectra of PTR12 and PTK44A. The reason that the Pb X-rays are not equally visible in all spectra is that different amounts of lead bricks were used to stabilise the materials in the setup, depending on the geometry of each sample. All three features are indicated on the spectra in Fig. 7.2. The radioisotopes that were assigned to the peaks in the spectra are denoted as well. ^{57}Co and ^{54}Mn are observed the most. The other radioisotopes which are identified from the γ-spectra are ^{22}Na, ^{58}Co, ^{60}Co, ^{65}Zn and ^{124}Sb. Finally, ^{40}K is observed as well. This is a naturally occurring radioisotope, which explains why it was also detected in the background spectrum. In fact, the ^{40}K peak is best visible in the background spectrum, due to the higher statistics of the background acquisition. The overlap of the ^{40}K peaks in the background and the spectra of the samples indicates that it is only natural ^{40}K from the environment that is observed. In other words, the ^{40}K signal does not stem from the samples themselves. An overview of all other identified radioisotopes and their most relevant properties (i.e. half-life, γ-energies etc.) is given in Tab. 7.1. Note that ^{22}Na, ^{54}Mn, ^{58}Co and ^{65}Zn all emit 511 keV photons (following β^+-decay, see section 1.1.2). Hence, the annihilation peaks in the spectra are usually due to contributions of multiple radioisotopes.

For the eight cyclotron parts in which radioactivity was detected by the Kromek GR05 detector, the activity was calculated for the observed radioisotopes. This was done following the methodology described in section 2.4. First, the measured background was subtracted

Table 7.1: Information on the radioisotopes that were identified in the γ-spectra of the 12 cyclotron parts. Data taken from Ref. [24]. Only the energies and intensities of the γ-rays relevant for this experiment (i.e. those observed in the spectra) are included.

Isotope	Half-life	γ-energies [keV]	γ-intensities [%]
^{22}Na	2.6018(22) y	511 1274.537(7)	179.91(18) 99.940(14)
^{54}Mn	312.20(20) d	511 834.848(3)	$< 0.000\,001\,14$ 99.976(1)
^{57}Co	271.74(6) d	122.060 65(12) 136.4736(3)	85.60(17) 10.68(8)
^{58}Co	70.86(6) d	511 810.7593(20)	29.8(4) 99.45(1)
^{60}Co	5.2711(8) y	1173.228(3) 1332.492(4)	99.85(3) 99.9826(6)
^{65}Zn	243.93(9) d	511 1115.539(2)	2.842(14) 50.04(10)
^{124}Sb	60.20(3) d	602.7260(23) 720.094(5)* 1690.971(4)	97.8(3) 14.39(5) 47.57(18)

* The given value is the weighted mean of three closely spaced γ-rays. The corresponding intensity is the total intensity for the three.

from each spectrum. The SNIP algorithm was applied to the difference, in order to estimate and subsequently subtract the Compton background. Then, the remaining peaks were fitted. In contrast to what was done in chapter 4 for the Tb activities, Voigt profiles instead of Gaussians were used for fitting in this case. Those models better approximate the relatively broad tails of the peaks in the spectra. The fits were integrated within a 3σ interval around the central energy, to get the number of counts ($N(E)$) for each peak. The resulting count rates (i.e. $N(E)/t$ with t the livetime of the acquisition) for all observed peaks are given in Tab. 7.2. As explained in the methodology in section 2.4, the activity can then be determined by

$$A = \frac{N(E)}{I(E) \times \epsilon_{abs}(E) \times t}, \tag{7.4}$$

with $I(E)$ the intensity of the radiation contributing to the peak and $\epsilon_{abs}(E)$ the absolute detection efficiency of the setup [4]. The intensities of the relevant γ-rays are given in Tab. 7.1. To get the absolute efficiency for the particular arrangements that were used, the intrinsic efficiency of the detector (given in Eq. 7.3) was corrected for the solid angle (Ω) of the detector in each setup [4]:

$$\epsilon_{abs} = \epsilon_{intr} \frac{\Omega}{4\pi}. \tag{7.5}$$

The solid angle was calculated according to the flat sphere approximation:

$$\Omega \cong \frac{D}{d^2}, \tag{7.6}$$

where D represents the area of the front detector plane and d the distance between the detector and the sample [4]. As the Kromek GR05 CZT detector has dimensions of $0.5\,\text{cm} \times 0.5\,\text{cm} \times 0.5\,\text{cm}$ (see section 2.3), $D = 0.25\,\text{cm}^2$. The sample-detector distance (d) differed between measurements and is given in Tab. 7.2 for each sample. The calculated activities for the various radionuclei in each object are given in Tab. 7.3. For isotopes for which more than one peak was identified, the weighted mean was taken of the activities calculated from the individual peaks. To avoid underestimates of the uncertainties on the weighted mean values, the calculated uncertainties were multiplied by $\sqrt{\chi^2_{red}}$. In this manner, the χ^2_{red}-value was forced to be 1 for the final result. However, this formula could not always be applied, because of systematic errors. The weighted mean activities for which the original uncertainty was kept are indicated in Tab. 7.3.

In the activity calculations, the observed annihilation peaks were attributed to a single radioisotope for all cases but one (PTK44A). In the spectrum of PTR12, only one radioisotope that emits 511 keV photons in its decay is observed, namely ^{22}Na. So, the annihilation peak is entirely due to ^{22}Na. In contrast, for the other spectra exhibiting an annihilation peak, two to three (for PTK44A) radioisotopes contribute to the peak. The extents to which they contribute differ, however, depending on the respective activities of the radioisotopes and the intensities of their 511 keV γ-rays (given in Tab. 7.1). To justify neglecting the contribution of certain radioisotopes to the annihilation peak, the expected number of counts in the annihilation peak was calculated for the different radioisotopes and compared to the observed counts. The calculation of the expected counts for a given radioisotope relies on the relation of this number to the measured number of counts in another peak of the same radioisotope. Considering the other peak to be at energy E_0,

Table 7.2: Count rates for all peaks in the spectra given in Fig. 7.2.

	Date	Distance [cm]	Count Rate [cps]											
			^{57}Co 122 keV	^{57}Co 136 keV	Annihilation 511 keV	^{124}Sb 603 keV	^{124}Sb 720 keV	^{58}Co 811 keV	^{54}Mn 835 keV	^{65}Zn 1116 keV	^{60}Co 1173 keV	^{22}Na 1275 keV	^{60}Co 1332 keV	^{124}Sb 1691 keV
PTR12	01/03/2022	5.4(3)	0.075(3)		1.362(11)							0.1194(14)		
PTK42	20/02/2022	3.5(3)	0.216(5)	0.086(5)	1.039(9)				0.0083(7)			0.0987(9)		
PTK34	22/12/2021	1.0(2)	0.392(9)	0.046(6)	0.604(7)				0.085(3)			0.050(2)		
PTK22	08/01/2022	4.0(3)	0.316(5)	0.028(3)	0.0584(15)					0.0034(3)	0.0049(3)	0.0043(3)	0.0018(2)	
PTK44A	04/02/2022	2.5(2)	0.159(2)	0.0171(14)	0.0109(11)	0.0415(7)	0.0031(5)	0.0089(3)	0.0213(5)	0.006 68(15) †	0.005 46(14) †		0.0043(4)	0.002 99(15)
PTK44B	04/02/2022	1.0(2)	0.083(6)						0.035(3)					
PTK28A	04/03/2022	1.2(2)	0.160(4)	0.018(2)					0.0187(8)		0.0019(2)			
PTK28B	02/03/2022	1.5(3)							0.0131(8)		0.001 10(15)			
PTK46A	22/03/2022	1.3(3)	No peaks observed											
PTK46B	25/03/2022	1.7(3)												
PTK27A	14/03/2022	1.3(2)												
PTK27B	10/03/2022	1.2(2)												

† These values are the results of adding the observed counts within the interval of the peak instead of integrating under the fit, because the quality of the fit was not good enough.

Table 7.3: Activities of the identified radioisotopes in each of the cyclotron parts, calculated from the count rates given in Tab. 7.2.

	Date	Activity [Bq]						
		^{22}Na	^{54}Mn	^{57}Co	^{58}Co	^{60}Co	^{65}Zn	^{124}Sb
PTR12	01/03/2022	$35(5) \times 10^3$		189(25)				
PTK42	20/02/2022	$11(2) \times 10^3$	478(95)	267(149)				
PTK34	22/12/2021	517(149) †	403(163)	35(10) †				
PTK22	08/01/2022	765(90) †		392(48) †		446(126)	973(172)	
PTK44A	04/02/2022		630(107)	86(11) †	246(33) †	347(44) †	754(128)	624(67) †
PTK44B	04/02/2022		165(68)	7(3)				
PTK28A	04/03/2022		128(43)	20(5) †		27(10)		
PTK28B	02/03/2022		139(57)			25(11)		

† In these cases, the uncertainty on the weighted mean activity was not multiplied by $\sqrt{\chi^2_{red}}$, because that led to smaller uncertainties than the original, most likely due to systematic errors.

the relation can be written as

$$N(511\,\text{keV}) = N(E_0)\,\frac{I(511\,\text{keV}) \times \epsilon_{abs}(511\,\text{keV})}{I(E_0) \times \epsilon_{abs}(E_0)}. \tag{7.7}$$

This expression follows from evaluating Eq. 7.4 at two different energies. Let us first apply the formula to ^{22}Na and ^{54}Mn for PTK34. For ^{22}Na, $E_0 = 1274.537(7)\,\text{keV}$, and the observed count rate at that energy is given in Tab. 7.2. Taking the intensities of the γ-rays at E_0 and 511 keV from Tab. 7.1 and evaluating the absolute efficiency at both energies according to Eq. 7.5, the expected count rate in the annihilation peak was found to be $0.8(4)\,\text{cps}$ for ^{22}Na. Similarly, for ^{54}Mn and $E_0 = 834.848(3)\,\text{keV}$, the expected count rate at 511 keV was determined to be $3.3(19) \times 10^{-9}\,\text{cps}$. So, the contribution of ^{54}Mn to the annihilation peak is negligible with respect to that of ^{22}Na for PTK34. Note that this could be anticipated from the intensities of the 511 keV γ-rays in the decay of the radioisotopes: for ^{22}Na the intensity is 179.91(18) %, whereas for ^{54}Mn it is known to be no higher than 0.000 001 14 % (see Tab. 7.1). Based on the same argument, the annihilation peak was entirely attributed to ^{22}Na in the activity calculations for sample PTK42 as well – especially since the ^{54}Mn peak around 834.848(3) keV and thus the activity of the radioisotope are much smaller than for PTK34. Looking at sample PTK22, the contributions of ^{22}Na and ^{65}Zn to the annihilation peak must be quantified. Since the intensity of the 511 keV γ-ray in the decay of ^{65}Zn is 2.842(14) %, the effect of this radioisotope is expected to be larger than for ^{54}Mn. Calculating the expected count rates contributing to the annihilation peak for ^{22}Na (with $E_0 = 1274.537(7)\,\text{keV}$) and ^{65}Zn (with $E_0 = 1115.539(2)\,\text{keV}$) according to Eq. 7.7, gives $0.066(15)\,\text{cps}$ and $0.0012(3)\,\text{cps}$ respectively. ^{65}Zn indeed contributes significantly more to the annihilation peak than ^{54}Mn for the previous samples, but the expected count rate does remain an order of magnitude

smaller than that for ^{22}Na. Compared to the total measured count rate of 0.0584(15) cps for the annihilation peak of PTK22, the expected count rate for ^{65}Zn represents only 2 %. In the activity calculations for PTK22, this fraction was neglected and the 511 keV peak was considered to be entirely due to ^{22}Na. Finally, let us consider the origin of the annihilation peak observed for PTK44A. In this object, three radioisotopes are identified that emit 511 keV photons upon decay, namely ^{54}Mn, ^{65}Zn and ^{58}Co. For each of them, the expected contribution to the observed annihilation peak was determined by Eq. 7.7 (with E_0 = 810.7593(20) keV for ^{58}Co). The resulting count rates are $8(2) \times 10^{-10}$ cps for ^{54}Mn, 0.0025(6) cps for ^{65}Zn, and 0.008(2) cps for ^{58}Co. So, for PTK44A both ^{65}Zn and ^{58}Co contribute significantly to the annihilation peak, but the contribution of ^{54}Mn is negligible. For the activity calculations for PTK44A, the calculated expected count rate by ^{65}Zn in the annihilation peak was subtracted from the total measured count rate of 0.0109(11) cps. The remainder was then assumed to be purely due to ^{58}Co and was used to calculate the ^{58}Co activity according to Eq. 7.4. The result was in agreement with the ^{58}Co activity determined from the peak around 810.7593(20) keV. The weighted mean of both values is given in Tab. 7.3. The activity of ^{65}Zn in PTK44A was calculated strictly from the peak around 1115.539(2) keV.

An important remark with respect to the activities presented in this section, is that they were calculated from the acquired γ-spectra without any corrections for the geometry or volume of the samples. Consequently, the obtained activities actually represent activities of a point source at distance d from the detector. The true activities in the synchrocyclotron parts may be higher. The fact that the samples have a finite volume implies that radiation coming from radioisotopes deep inside the material is attenuated or even absorbed within the sample itself, leading to only a fraction of the emitted radiation reaching the detector. This issue is referred to as "self-absorption". Furthermore, the absolute efficiency is different for each point on the object, which also affects the activity calculation. To account for all of these effects and to determine the true activities inside the cyclotron parts, full numerical integration and simulations with software such as GEANT4 would be required. That was beyond the scope of this thesis, so all discussions in the next section are based on the activities as calculated above. However, this means that caution is required in drawing any definitive conclusions and that all calculated quantities should be considered as first approximations.

7.3 Discussion

The discussion of the γ-spectra and the corresponding activities presented in the previous section is split into three separate parts. Section 7.3.1 focuses on the possible proton-induced reaction mechanisms responsible for the production of the observed radioisotopes. A comparison is made with the results of the FLUKA simulations in chapter 6. In section 7.3.2, upper limits to the activities of the most expected radioisotopes are determined for the four cyclotron parts for which no radioactivity was measured by the Kromek GR05 CZT detector. Finally, the conditions for clearance of the different proton-activated samples are evaluated in section 7.3.3.

7.3.1 Production Pathways

In follow up to the discussions of the FLUKA simulations presented in chapter 6, it is important to understand how the radioisotopes observed during the experiment were generated. An overview of all identified radioisotopes and their respective activities per sample is given in Tab. 7.3 in the previous section. ^{54}Mn and ^{57}Co are present in nearly all samples, ^{22}Na and ^{60}Co each in half of them, ^{65}Zn only in PTK22 and PTK44A, and ^{58}Co and ^{124}Sb exclusively in PTK44A. Most of these radioisotopes were predicted by the FLUKA simulations for common construction materials in accelerators (i.e. Al/AlMgSi, Cu and stainless steel). Therefore, the proton-induced reactions discussed in chapter 6 are expected to be largely responsible for their production.

Any ^{22}Na in the synchrocyclotron parts is expected to be produced via $^{27}\mathrm{Al}(p, \alpha + p + n)^{22}\mathrm{Na}$ or $^{25}\mathrm{Mg}(p, \alpha)^{22}\mathrm{Na}$, in accordance with the FLUKA simulations for Al and AlMgSi. This is the case for PTR12 and PTK42, which are known to consist (partially) of AlMgSi (see appendix D). ^{22}Na is also observed for PTK22, which is made up of Cu (see appendix D). Since the FLUKA simulation for proton irradiation of pure Cu does not predict any ^{22}Na to be produced, the presence of this radioisotope in PTK22 is most likely due to an Al impurity in the material. The ^{57}Co, ^{60}Co and ^{65}Zn that are observed in PTK22 were expected based on the FLUKA simulation for Cu. In general, ^{65}Zn is always expected to be produced by $^{65}\mathrm{Cu}(p, n)^{65}\mathrm{Zn}$ in Cu containing samples. The Co radioisotopes, in contrast, can be generated by a multitude of proton-induced reactions on stable Fe, Ni or Cu isotopes. They are discussed in more detail later in this section. Here, we just note that, for PTR12, the observed ^{57}Co – which is not predicted by FLUKA to be generated upon proton irradiation of AlMgSi – points to an impurity of Fe, Ni or Cu in the AlMgSi composition. In PTK42, the observed ^{57}Co as well as ^{54}Mn stem from reactions with the stainless steel that is also incorporated in this object (see appendix D).[3]

The only observed radioisotope that is not predicted by FLUKA for any of the considered construction materials is ^{124}Sb, which is observed in PTK44A. Looking at the nuclear chart, ^{124}Sb is most likely produced from tin via $^{124}\mathrm{Sn}(p, n)^{124}\mathrm{Sb}$. This is illustrated in Fig. 7.3. Sn is a metal that is often used in corrosion resistant coating layers [69], so it is plausible that it is present to some extent in the cyclotron parts. Since there are many stable isotopes of Sn – several of which have significantly higher abundances than ^{124}Sn – other Sb radioisotopes besides ^{124}Sb are expected to be produced by (p, n) reactions as well. However, these are not observed in the γ-spectrum of PTK44A. That can be explained by their relatively short half-lives. The longest half-life of the other Sb radioisotopes that can be produced is 5.76(2) d for ^{120}Sb [3]. Consequently, all these radioisotopes decayed to negligible activities by the time the γ-spectrometry measurements with the Kromek GR05 detector were performed for PTK44A, leaving only ^{124}Sb.

Apart from checking which of the observed radioisotopes are predicted by FLUKA – to gain insight into the nuclear reactions that produced them – it is also relevant to look at which of the radioisotopes predicted by FLUKA are not observed in the experiment.

[3]The discussion here is limited to PTR12, PTK42 and PTK22, because these are the only samples for which the composition is known. Nevertheless, the other cyclotron parts are also expected to be made at least partly of AlMgSi, Cu or steel, so the general reaction mechanisms are assumed to apply to all.

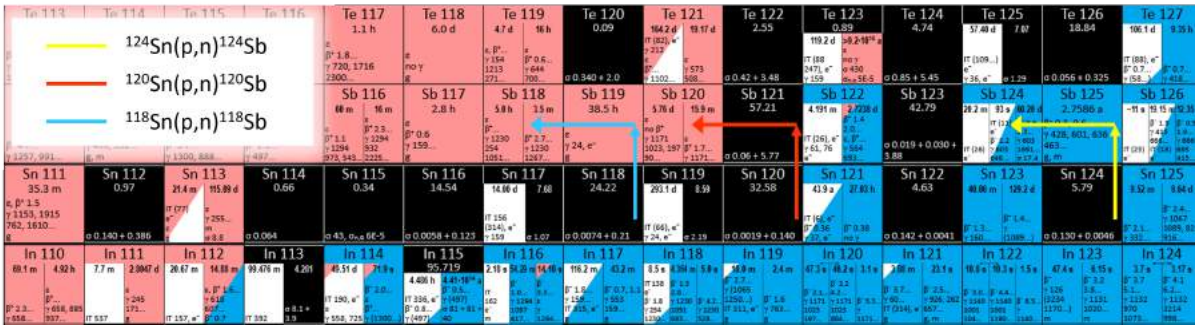

Figure 7.3: Illustration of the production of ^{124}Sb *and other Sb radioisotopes via* (p, n) *reactions on stable isotopes of Sn. Nuclear chart from Ref. [3].*

Given that the samples from PARTICLE were taken out of the synchrocyclotron at least several months before the experiment was conducted, the results should be compared to the FLUKA predictions for 6 months to 1 year after the end of the proton irradiation. As it turns out, there are several radioisotopes which are predicted to be present in significant amounts, but are not observed in any of the acquired γ-spectra. Consider for example ^{49}V ($T_{1/2} = 330(15)$ d [24]). This radioisotope is predicted to be one of the most active radioisotopes in stainless steel in the long term. The fact that it is not observed in the γ-spectra of the cyclotron parts is a consequence of its decay properties: ^{49}V decays directly to the ground state of stable ^{49}Ti (by EC), so no γ-rays are emitted [24]. Hence, ^{49}V is undetectable by any γ-ray detector, such as the Kromek GR05 CZT detector used for this experiment. The same holds for ^{3}H ($T_{1/2} = 12.32(2)$ y [24]), which is predicted for all simulated materials due to break-up reactions of the type $(p, {}^{3}\mathrm{H})$: ^{3}H decays directly to the ground state of stable ^{3}He (via β^--decay) without emitting any γ-rays [24]. For ^{55}Fe ($T_{1/2} = 2.744(9)$ y [24]), this reasoning does not apply however. ^{55}Fe is predicted by FLUKA to be among the most active radioisotopes after 6 months to 1 year in both stainless steel and Cu, and it emits a single γ-ray at 126.0(1) keV in its decay. So, in principle it should be detectable. Nevertheless, the intensity of the γ-ray is only 0.000 000 128(2) % [24], meaning that very large activities of ^{55}Fe would have to be present for the signal to be visible in the spectra. On top of that, the peak would lie in between the two ^{57}Co peaks (at 122.060 65(12) keV and 136.4736(3) keV), so it would be difficult to distinguish. Finally, let us consider ^{56}Co ($T_{1/2} = 77.236(26)$ d [24]). This radioisotope is also predicted to be present in stainless steel and Cu in the long term, albeit in considerably lower amounts than ^{49}V and ^{55}Fe. ^{56}Co emits multiple γ's in its decay, the most intense one occurring at 846.770(2) keV with intensity 99.9399(23) % [24]. So, if present, ^{56}Co should be visible in the γ-spectra. The fact that it is not observed thus indicates that there must be very little ^{56}Co left in the samples.

The absence of ^{56}Co in the samples is important to take into account when studying the possible proton-induced reaction mechanisms for the observed Co radioisotopes. In particular, the nuclear reactions should explain the activity ratios of the different Co radioisotopes in each of the samples. The results in Tab. 7.3 show that ^{57}Co is virtually always present to some extent, ^{60}Co in half of the samples, and ^{58}Co only in one case. Consider first which Co radioisotopes would be expected from proton-induced reactions on stable Fe isotopes. As illustrated in Fig. 6.7 in the previous chapter, Co radioiso-

topes are produced from Fe by (p, Xn) reactions with $X = 1, 2, 3$. Given the relative abundance of 91.754 % for ^{56}Fe [3], the reaction $^{56}\mathrm{Fe}(p, n)^{56}\mathrm{Co}$ seems the most likely to occur. So, more ^{56}Co is expected to be present shortly after proton irradiation of Fe than any of the other Co radioisotopes. However, because of the shorter half-life of ^{56}Co, namely 77.236(26) d [24], the ratios change in time and ^{57}Co eventually becomes the most abundant Co radioisotope in the long term. This is also visible in Fig. 6.6b. Note that ^{60}Co cannot be produced in any way by proton-induced reactions on stable Fe isotopes. Therefore, it seems very likely that, in the samples for which only ^{57}Co is observed in the γ-spectra, the Co production stems from (p, n) reactions on stable Fe isotopes.
On the other hand, in the samples where ^{60}Co is observed as well, there must be proton-induced reactions on Ni and/or Cu. Of all the possible proton-induced reactions for these elements discussed in chapter 6, the $(p, 2p)$ reactions on stable Ni isotopes are particularly interesting to consider. These reactions generate ^{57}Co and ^{60}Co via $^{58}\mathrm{Ni}(p, 2p)^{57}\mathrm{Co}$ and $^{61}\mathrm{Ni}(p, 2p)^{60}\mathrm{Co}$. The other long-lived Co radioisotopes ^{56}Co and ^{58}Co cannot be produced by this type of reaction, since ^{57}Ni and ^{59}Ni are unstable. Hence, the $(p, 2p)$ reactions on Ni could perhaps explain the presence of ^{57}Co and ^{60}Co without any other Co radioisotopes in some of the cyclotron parts.
Nevertheless, this cannot be the entire story. In particular, PTK22 is known to consist of Cu (see appendix D), so the ^{57}Co and ^{60}Co activities in this object should be produced by proton-induced reactions on Cu instead of Ni. Although it is possible that there are impurities of Ni in the material, the Co radioisotopes generated from Cu should dominate in the sample. Based on the FLUKA results in Fig. 6.9b, this means that there should be ^{56}Co and ^{58}Co in addition to ^{57}Co and ^{60}Co. The most likely explanation for not observing these radioisotopes seems to be that PTK22 was taken out of the accelerator more than a year ago. As can be seen in Fig. 6.9b, the ^{56}Co and ^{58}Co activities decay fast compared to those of ^{57}Co and ^{60}Co, due to their half-lives of 77.236(26) d and 70.86(6) d, respectively [24]. Furthermore, ^{57}Co decays faster than ^{60}Co, given their respective half-lives of 271.74(6) d and 5.2711(8) y. So, extrapolating the results of the FLUKA simulation for Cu, it is expected that eventually the ^{57}Co activity will drop below that of ^{60}Co, as is observed for PTK22.
Finally, for PTK44A, matters are even more complicated. This sample contains ^{58}Co in addition to ^{57}Co and ^{60}Co, so it cannot have been taken out of the accelerator year(s) ago. This is also confirmed by the presence of ^{124}Sb, which has a half-life of 60.20(3) d. On the other hand, ^{56}Co is not observed and the ^{57}Co activity is much lower than that of ^{60}Co. One option is that the observed Co radioisotopes stem predominantly from $(p, \alpha+p+Xn)$ reactions on stable Cu isotopes: ^{58}Co and ^{60}Co are generated via $^{63}\mathrm{Cu}(p, \alpha + p + n)^{58}\mathrm{Co}$ and $^{65}\mathrm{Cu}(p, \alpha + p + n)^{60}\mathrm{Co}$, whereas for ^{56}Co and ^{57}Co more neutrons need to be ejected. This might imply less production of ^{56}Co and ^{57}Co, leading to lower initial activities for radioisotopes to begin with.

Overall, it proves to be very difficult to determine the precise origin of the Co radioisotopes in the different cyclotron parts, because the ratios in which they are present depend on many factors. Firstly, there is dependence on the composition of the irradiated material and the cross sections of the possible proton-induced reactions in that material. As reaction cross sections are additionally energy dependent (see section 1.2.1), the positioning of the sample in the accelerator also plays a role: depending on how much the protons need to be scattered to reach the sample, the incident energy will be different. Finally,

the ratios depend on how much time has passed since the end of the irradiation. This has to do with the radioactive decay of the different radioisotopes, each according to its own well-defined half-life. Given that most of these parameters are unknown for the samples from PARTICLE, their influence on the presence of the different Co radioisotopes – and others – could not be quantified.

7.3.2 Minimal Detectable Activities

For four synchrocyclotron parts, no peaks were observed in the γ-spectra acquired by the Kromek GR05 detector (see Fig. 7.2). However, this does not necessarily mean that there is no radioactivity in these objects. Instead, any present radioactivity could be so low that it is effectively undetectable under the current experimental conditions. To quantify an upper limit, the "minimal detectable activity" (MDA) was estimated for the radioisotopes that are most likely to be present. Since the four objects in question, i.e. PTK46A/B and PTK27A/B, are similar in composition to PTK44A/B and PTK28A/B (see appendix D), mostly the same radioisotopes are expected to be produced in them upon irradiation by protons. For PTK44A/B and PTK28A/B, the most common radioisotopes that were observed are ^{54}Mn, ^{57}Co and ^{60}Co. Therefore, the MDA's of these radioisotopes in PTK46A/B and PTK27A/B are determined in this section.

The general idea behind the MDA's is that a minimal number of counts must be recorded by the Kromek GR05 detector for a distinguishable peak to appear in the γ-spectrum. That has to do with the signal-to-noise ratio: a signal must exceed the noise to a considerable extent to become distinctly visible. Consider, by way of illustration, the γ-spectrum for PTK28B in Fig. 7.2h. For ^{65}Zn, the signal-to-noise ratio is approximately 1, making it difficult to conclude whether there is truly a ^{65}Zn peak or whether the apparent signal is merely a fluctuation in the background. The ^{60}Co signals are somewhat better distinguishable and for ^{54}Mn there is an undeniable peak, owing to higher signal-to-noise ratios. Based on these considerations, the threshold for a signal to be perceptible is taken to be $3\sqrt{b}$, with $\sqrt{b}$ the Poisson fluctuation of the background level (b) (i.e. the noise). In other words, the height of any signal must be larger than $3\sqrt{b}$ for it to be noticeable in the spectrum. Imagine now a sample containing some radioisotope of activity A that emits γ-rays at energy E_0 with intensity $I(E_0)$. By rewriting Eq. 7.4, it can be deduced that the number of counts recorded by the detector would be

$$N(E_0) = A \times I(E_0) \times \epsilon_{abs}(E_0) \times t \tag{7.8}$$

for a measurement of livetime t – without accounting for volume effects for samples of considerable size. Due to the limited energy resolution of the detector (given in Eq. 7.2), the recorded counts ($N(E_0)$) are not all observed at exactly E_0 in the acquired spectrum; rather, they are spread over a peak around (approximately) E_0. For simplicity, we assume the peak to be a Gaussian of the form

$$g(E) = \frac{G}{\sigma\sqrt{2\pi}} \exp\left\{\frac{-(E-E_0)^2}{2\sigma^2}\right\}, \tag{7.9}$$

where G denotes the total integral of the function. To be distinguishable in the spectrum, the height $G/\sigma\sqrt{2\pi}$ of the peak must be larger than the threshold of $3\sqrt{b}$. This can be rewritten in terms of $N(E_0)$ and E_0 in the following way. Consistent with the rest of this

thesis, the recorded counts ($N(E_0)$) are considered to be equal to the integral of the peak within a 2σ interval around its centre. This represents 95.45 % of the total integral (G), based on the empirical 68-95-99.7 rule for Gaussian distributions in statistics. So,

$$G = \frac{N(E_0)}{0.9545}. \tag{7.10}$$

Furthermore, the standard deviation (σ) of the peak is determined by the energy resolution of the Kromek GR05 detector (given in Eq. 7.2), according to

$$R(E_0) = \frac{\text{FWHM}}{E_0} = \frac{2\sqrt{2\ln 2}\sigma}{E_0} \tag{7.11}$$

Here, the second equality only holds for Gaussians and FWHM signifies the full width at half maximum of the peak [4]. Combining the expressions for σ and G to get the height $G/\sigma\sqrt{2\pi}$ of the Gaussian peak and demanding this to be larger than the threshold of $3\sqrt{b}$, the condition for the signal to be visible in the spectrum becomes

$$\frac{N(E_0)}{0.9545}\ \frac{2\sqrt{\ln 2}}{\sqrt{\pi} \times R(E_0) \times E_0} \geq 3\sqrt{b}. \tag{7.12}$$

Finally, substituting $N(E_0)$ by Eq. 7.8 and solving for the activity, the MDA is defined as

$$A \geq 1.43175\ \frac{\sqrt{b} \times R(E_0) \times E_0}{I(E_0) \times \epsilon_{abs}(E_0) \times t}. \tag{7.13}$$

The absolute detection efficiency ($\epsilon_{abs}(E_0)$) in this expression is determined by Eq. 7.5 and Eq. 7.6, and depends on the distance between the sample and the detector. So, the MDA will vary for different experimental arrangements. Furthermore, the MDA depends on the livetime (t) of the measurement, on the radioisotope (through $I(E_0)$, see Tab. 7.1), and on energy (through E_0 as well as b, since the background is energy-dependent as a result of the intrinsic efficiency of the detector and Compton effects).

The results of applying Eq. 7.13 for ^{54}Mn, ^{57}Co and ^{60}Co in PTK46A/B and PTK27A/B are given in Tab. 7.4. The calculated MDA for ^{57}Co in PTK28B is included as well. PTK28B is the only object of the eight with measurable radioactivity for which no ^{57}Co peaks were observed. Therefore, it seemed valuable to determine an upper limit to the activity of ^{57}Co in this sample as well. Note that ^{54}Mn and ^{60}Co were observed in the spectrum of PTK28B and their corresponding activities are given in Tab. 7.3, so for these radioisotopes no upper limits needed to be estimated. The MDA's in Tab. 7.4 show that very little amounts of ^{57}Co are expected in the samples. For ^{54}Mn and ^{60}Co, the upper limits allow for higher activities to be present. Compared to the activities observed for PTK44A/B and PTK28A/B (see Tab. 7.3), the upper limits for ^{54}Mn lie significantly lower: the observed activities are of the order of 100 Bq, whereas the MDA's for PTK46A/B and PTK27A/B limit the ^{54}Mn activities in these objects to maximally a few 10 Bq. In contrast, the calculated MDA's for ^{60}Co, in principle, allow activities of the same order of magnitude as in PTK44A/B and PTK28A/B. Nevertheless, it is important to stress that this is not necessarily the case. In fact, the notable absence of peaks in the spectra of PTK46A/B and PTK27A/B (see Fig. 7.2) for similar sample-detector distances suggests lower ^{60}Co activities in these samples. In this regard, it is

Table 7.4: Minimal detectable activities (MDA) for ^{54}Mn, ^{57}Co and ^{60}Co. The energies quoted under the radioisotopes signify the E_0 of the γ-rays for which Eq. 7.13 was evaluated.

	MDA [Bq]		
	^{54}Mn 834.848(3) keV	^{57}Co 122.060 65(12) keV	^{60}Co 1173.228(3) keV
PTK28B		1.51	
PTK46A	29	0.45	65
PTK46B	37	0.64	42
PTK27A	26	0.37	63
PTK27B	22	0.38	69

important to keep in mind that the MDA's strictly serve as upper limits and all activities below them remain possible. To make more accurate statements about the activities in PTK46A/B and PTK27A/B – or to lower the values for the upper limits from those in Tab. 7.4 – measurements with a detector of higher sensitivity than the Kromek GR05 CZT detector or in an environment with a lower background (e.g. in a fully closed lead castle) would have to be performed.

7.3.3 Clearance Levels

To determine which of the proton-activated synchrocyclotron parts can be disposed of and which need to undergo radioactive waste processing and decay-in-storage, the condition for clearance is evaluated here for the eight samples in which radioactivity was detected by the Kromek GR05 detector.

As mentioned in section 5.3, for solid samples containing a mixture of radionuclei, the condition for clearance is

$$\sum_j \frac{a_j}{C_j} \leq 1, \tag{7.14}$$

where j iterates over all present radionuclei, and a_j and C_j represent respectively the activity concentration and clearance level (defined in the royal decree ARBIS, see Ref. [63]) corresponding to each individual species. The clearance levels for the radioisotopes that were identified in the γ-spectra of the synchrocyclotron parts are given in Tab. 7.5. To

Table 7.5: Clearance levels for the radionuclei that were observed in the synchrocyclotron parts, as defined in ARBIS (see Ref. [63]).

Radioisotope	^{22}Na	^{54}Mn	^{57}Co	^{58}Co	^{60}Co	^{65}Zn	^{124}Sb
Clearance Level [kBq/kg]	0.1	0.1	1	1	0.1	0.1	1

determine the activity concentrations (a_j) for all radioisotopes per sample, the calculated activities (given in Tab. 7.3) were each divided by the weight of the respective sample. The weights are given in Tab. 7.6, alongside the final outcomes for the sum in the clearance condition in Eq. 7.14. Besides for the activities in Tab. 7.3, the sum was also evaluated for the activities propagated to within five years. Given that NIRAS is required to make an inventory of all sites containing radioactive materials every five years (see section 5.3), this allows to evaluate how much the values can change by the next inventory. The propagated activities are given in Tab. 7.7, the results for the clearance condition in Tab. 7.6.

Consider first the present-day results for Eq. 7.14. The clearance condition is fulfilled for three out of the eight objects, namely PTK44B and PTK28A/B. For all others, the calculated sum is larger than 1. A maximal value of 691(101) is obtained for PTR12. This result follows from the high activity of ^{22}Na (i.e. 35(5) kBq, see Tab. 7.3) observed in the relatively light object PTR12 (weighing 0.5 kg). The activity concentration of ^{22}Na in PTR12 was determined to be 69(10) kBq/kg. This lies far above the clearance level of 0.1 kBq/kg for ^{22}Na, and therefore contributes significantly to the sum in Eq. 7.14. In contrast, the activity concentration of the ^{57}Co that is also present in PTR12 is much lower, namely 379(49) Bq/kg, and lies below the clearance level of 1 kBq/kg for ^{57}Co. Therefore, the high result for PTR12 in Tab. 7.6 is almost entirely due to the high ^{22}Na activity. The same holds for PTK42. In this sample, also a high activity of ^{22}Na was observed (i.e. 11(2) kBq, see Tab. 7.3), which contributes significantly to the sum in Eq. 7.14. The reason for the high activities measured for PTR12 and PTK42 is that these samples were irradiated directly by the 230 MeV proton beam at PARTICLE. In contrast, the other samples were not positioned in the beam path and were only irradiated

Table 7.6: Results of the sum in the clearance condition (Eq. 7.14) for the synchrocyclotron parts in which radioactivity was detected. Values above 1 are indicated in red, values below 1 (i.e. satisfying the clearance condition) in green. The weights of the objects are given as well.

	Weight [kg]	$\sum_j a_j/C_j$	
		Now	In 5 years
PTR12	0.5	691(101)	182(27)
PTK42	1.5	79(14)	20(4)
PTK34	0.5	18(4)	2.9(8)
PTK22	1	22(2)	4.4(7)
PTK44A	3	6.1(6)	0.65(8)
PTK44B	10	0.17(7)	0.0029(12)
PTK28A	3	0.53(15)	0.05(2)
PTK28B	10	0.16(6)	0.015(6)

Table 7.7: Propagated activities in 5 years for the identified radioisotopes in the cyclotron parts.

	Activity in 5 years [Bq]						
	^{22}Na	^{54}Mn	^{57}Co	^{58}Co	^{60}Co	^{65}Zn	^{124}Sb
PTR12	$9.1(13) \times 10^3$		1.8(3)				
PTK42	$3.0(6) \times 10^3$	8.3(19)	2.5(14)				
PTK34	137(39)	7(3)	0.34(10)				
PTK22	202(13)		3.7(5)		231(65)	5.4(15)	
PTK44A		11(2)	0.82(12)	$4(6) \times 10^{-6}$	180(23)	4.2(11)	$5(8) \times 10^{-7}$
PTK44B		2.9(12)	0.07(3)				
PTK28A		2.2(8)	0.19(5)		14(5)		
PTK28B		2.4(10)			13(5)		

by scattered protons, leading to lower activities being generated. For PTK42, the activity concentration of ^{22}Na was found to be 7.5(14) kBq/kg. This is considerably smaller than in PTR12, because PTK42 weighs three times as much. The final result for the clearance condition – after adding the terms due to ^{54}Mn and ^{57}Co in PTK42 – is correspondingly much smaller than that for PTR12 as well, namely 79(14).

Given that PTK44B and PTK28A/B satisfy the clearance condition, it is expected that PTK46A/B and PTK27A/B – for which no radioactivity was measured by the Kromek GR05 detector – satisfy it too. The fact that no peaks were observed in the γ-spectra of these samples for similar experimental conditions, means that the activities of any present radioisotopes are lower than in the other objects. This was quantified by the MDA's presented in the previous section. The weights of PTK46A/B and PTK27A/B are the same as those of PTK44A/B and PTK28A/B, so the lower activities also mean lower activity concentrations and consequently smaller contributions to the sum in Eq. 7.14. Since this sum was already smaller than 1 for PTK44B and PTK28A/B, it must be for PTK46A/B and PTK27A/B as well.

After five years time, PTK44A satisfies the clearance condition too, as can be seen from Tab. 7.6. The remaining four cyclotron parts (i.e. PTR12, PTK42, PTK34 and PTK22) still have values (significantly) above 1, although they have decreased compared to the present-day results due to radioactive decay of the radioisotopes in the samples. The residual activities of the different radioisotopes per sample after five years – propagated from the activities in Tab. 7.3 – are explicitly given in Tab. 7.7. For all samples, ^{22}Na and/or ^{60}Co are left as the most active radioisotopes, because of their long half-lives of 2.6018(22) y and 5.2711(8) y, respectively. All other radioisotopes remain present only in small amounts in comparison. In particular, the ^{58}Co and ^{124}Sb activities have decayed to negligible values in PTK44A. For the four samples that do not satisfy the clearance

condition yet, it means that the decay of the ^{22}Na and/or ^{60}Co activities determines when the clearance condition will be satisfied.

In general, the decay in time of the sum in the clearance condition in Eq. 7.14 is governed by the half-lives and relative amounts of the different radioisotopes in the sample. For the synchrocyclotron parts with initial values larger than 1, the decay is plotted against time in Fig. 7.4 to get an indication of the timescales at which the clearance condition becomes fulfilled for each of them. As already mentioned, for PTK44A the clearance condition becomes satisfied within the next five years. For the PTK34, it takes almost nine years; for PTK22, 13 years; for PTK42, 16 years; and for PTR12 almost 25 years. So, the longest timescales are observed for the two samples that were directly irradiated by the 230 MeV proton beam. Note, however, that the timescale for PTK22 is rather comparable to that for PTK42, even though this sample was indirectly irradiated. This is due to the fact that there is ^{60}Co produced in PTK22 – in contrast to PTR12 and PTK42. The long half-life of ^{60}Co is responsible for the less steep decay of the result for the clearance condition in PTK22, observed in Fig. 7.4.

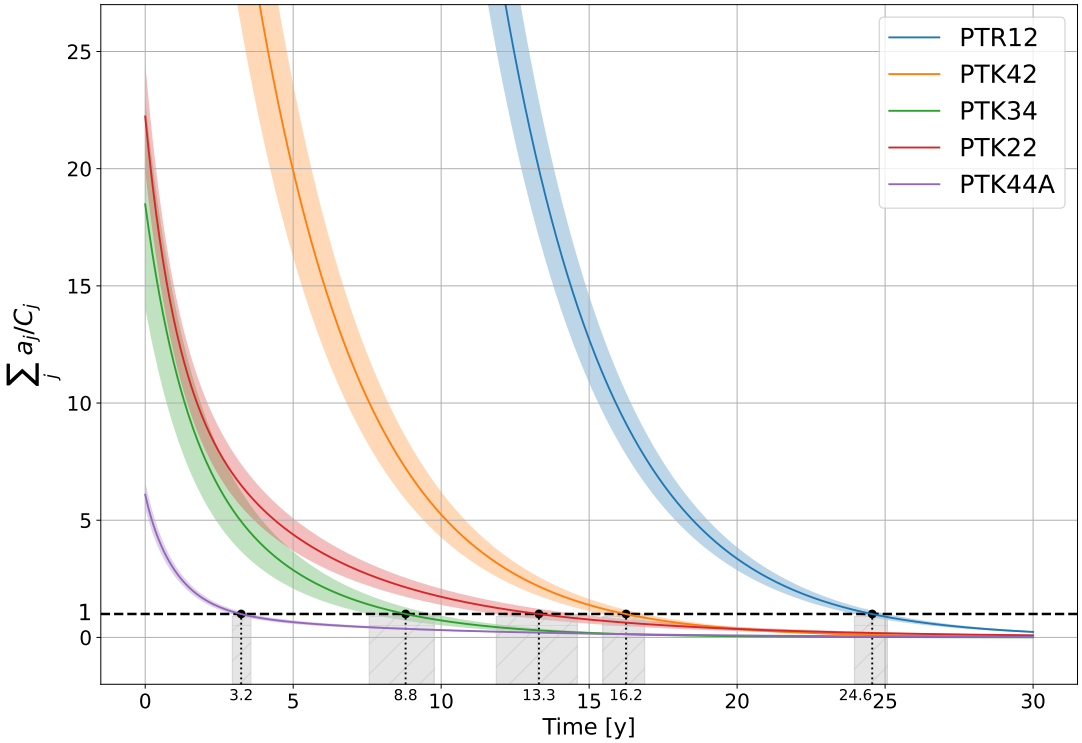

Figure 7.4: Decay in time of the results of the clearance formula for the objects with initial results exceeding 1. The times at which the respective values become lower than 1 and the objects can be cleared, are indicated by black dotted lines on the graph.

As final remark on the results for the clearance condition presented in this section, it is important to recall that all activities in Tab. 7.3 are only first approximations to the true activities in the synchrocyclotron parts. As mentioned at the end of section 7.2, the activity calculations were performed without correcting for volume effects of the objects (i.e. as if the objects were point sources at distance d from the detector). This implies that the true activities in the samples might be higher than the calculated ones presented in this thesis. Consequently, the results for the clearance condition in Eq. 7.14 might also

be higher and it might take longer before they decay to values below 1. The values in Tab. 7.6 and the expected timescales at which the different cyclotron parts satisfy the clearance condition are therefore to be interpreted as lower limits.

7.4 Conclusion & Outlook

In the context of waste management of proton-activated construction materials from the proton therapy facility PARTICLE, a spectroscopic study with a Kromek GR05 CZT detector was performed on 12 objects that used to serve as parts of the synchrocyclotron. Three main aspects were investigated in the experiment: which radioisotopes are present in the samples, in what activities they are present, and whether the condition for clearance is satisfied for the samples.

From the obtained γ-spectra, ^{22}Na, ^{54}Mn, ^{57}Co, ^{58}Co, ^{60}Co, ^{65}Zn and ^{124}Sb were identified. Most of these radioisotopes were expected to be observed based on the FLUKA simulations for common construction materials in accelerators. Only ^{124}Sb was not predicted by FLUKA. This radioisotope is presumably generated from ^{124}Sn via (p, n) reactions. For the other radioisotopes, the reaction mechanisms discussed in chapter 6 remain the most likely. First approximations to the activities of all observed radioisotopes were determined by assuming all samples to be point sources. The relative activities of different radioisotopes were observed to vary strongly across all samples. Multiple factors are responsible for this, including possible differences in material composition, positioning in the synchrocyclotron, incident proton energy, duration of the irradiation (i.e. years of service in the accelerator and operation of the accelerator during that time), and time passed since the last irradiation. The highest activities were obtained in the two objects which were directly irradiated by the 230 MeV proton beam (i.e. PTR12 and PTK42). For four samples, namely PTK46A/B and PTK27A/B, no peaks were observed in the γ-spectra acquired by the Kromek GR05 detector. For these cyclotron parts, minimal detectable activities (MDA's) were determined as upper limits to the activities for the most likely radioisotopes to be present. Finally, for the cyclotron parts that did have distinct peaks in their γ-spectra, the condition for clearance was evaluated. The results showed that the clearance condition is satisfied for PTK44B and PTK28A/B, so these objects can be disposed of or recycled. Since PTK46A/B and PTK27A/B definitely contain lower activities, they should also meet the clearance condition. In contrast, for PTR12, PTK42, PTK34, PTK22 and PTK44A the clearance condition is not satisfied, so these objects must undergo decay-in-storage and/or waste processing depending on the activities and half-lives of the present radioisotopes. The timescales at which the clearance condition becomes satisfied for these samples was shown to depend on the initial activities and the half-lives and relative amounts of the different radioisotopes in the sample. PTK44A meets the clearance condition after about three years. For the other samples, the timescales range up to almost 25 years for PTR12. Note that the number of different radioisotopes in principle does not play a role in evaluating the clearance condition. What is important are the activities of the radioisotopes and how they compare to the corresponding clearance levels defined in ARBIS.

As the activities and related quantities presented in this chapter are only first approximations to the true values, there is room for further research. For example, GEANT4

simulations could be performed to carry out the full numerical integration needed to account for volume effects of the considerably sized synchrocyclotron parts. Alternatively, one might consider the possibilities of using a γ-ray detector with a larger detection surface than the compact Kromek GR05 detector. Since the Kromek GR05 detector had to placed very close to the samples to detect any signals – given the relatively low count rates in most samples – only part of the sample was visible to the detector. A larger detector would allow to detect signals from the whole sample. Nevertheless, GEANT4 simulations would still be necessary in the activity calculations to account for self-absorption in the finite thickness of the sample. In general, which detector is used and how many corrections are taken into account during activity calculations all depends on which information is desired and how accurate the results should be. For example, if one simply wishes to know which radioisotopes are present inside a sample and what their relative activities are – such that one can determine the decay in time of the overall radioactivity – the Kromek GR05 detector is a suitable candidate, as shown in this thesis.

Part IV

General Conclusion

Conclusion on the use of a compact CZT γ-ray detector for nuclear applications in medicine

The two case studies for the use of Kromek GR CZT detectors discussed in this thesis illustrate the potential of these compact γ-ray detectors for nuclear applications in medicine. Firstly, the two distinct situations show that the detectors have a wide range of applicability. In particular, they can be used to detect high activity radiation ($\propto$ MBq) from radioisotopes that are produced for applications in nuclear medicine, as well as lower activity radiation ($\propto$ Bq $-$ kBq) from radioisotopes generated by interactions of ionising radiation with construction materials of clinical accelerators. Secondly, the compact size of the Kromek GR detectors and the fact that CZT detectors can operate at room temperature – in contrast to high-resolution HPGe detectors, for example – allows the detectors to be used in remote places which might be inaccessible to other detection systems. This is particularly useful in the context of radioisotope production for medical applications: the detector can be positioned right in front of the collection box where the radioisotope of interest is implanted, making it possible to follow the implanted activities in real time and thereby track the progress of the collection. Furthermore, the fact that the Kromek GR detectors are portable and only need a USB connection to a computer to work, makes it possible to perform measurements virtually anywhere. This can be useful in the context of radioactive waste management in hospitals: large activated construction materials could be measured on-site. On the other hand, for large objects with relatively low activity, the compact size of the Kromek GR detectors seems to be less convenient with respect to activity calculations. Due to the low activity, the detector must be placed close to the sample, such that only part of the object is effectively visible to the detector. Nevertheless, the Kromek GR detectors do allow identification of the radioisotopes that were generated in the object, and a first approximation or lower limit to their activities can be determined form the acquired γ-spectra.

In conclusion, the compact CZT detectors of Kromek's GR family represent practical, portable γ-ray detectors with great potential for qualitative measurements in the monitoring of radioisotope production for medical applications as well as in the management of clinical radioactive waste.

Bibliography

[1] Ruben Driesen. 'Activatie problematiek bij protontherapie'. MA thesis. KU Leuven, 2022.

[2] Kenneth S. Krane. *Introductory Nuclear Physics*. John Wiley & Sons, Inc., 1988.

[3] *Karlsruhe Nuclear Chart Online (KNCO++)*. Nucleonica. URL: https://www.nucleonica.com/.

[4] Glenn F. Knoll. *Radiation Detection and Measurement*. 4th Edition. John Wiley & Sons, Inc., 2010.

[5] Jacques Balosso et al. 'Radioisotope Production'. In: *Nuclear Physics for Medicine*. Nuclear Physics European Collaboration Committee (NuPECC). 2014. Chap. III.

[6] J. Zeman. *Reaktorová fyzika I*. ČVUT, 1999.

[7] Riccardo Raabe. 'Making Radioactive Ion Beams - Detecting Reaction Products'. In: *The European Physical Journal Plus* 131.362 (2016). DOI: 10.1140/epjp/i2016-16362-5.

[8] Piet Van Duppen. 'Isotope Separation On Line and Post Acceleration'. In: *The Euroschool Lectures on Physics with Exotic Beams, Vol. II*. Ed. by Jim Al-Khalili and Ernst Roeckl. Springer Berlin Heiderberg, 2006, pp. 37–77. DOI: 10.1007/3-540-33787-3_2.

[9] J. Benlliure. 'Spallation Reactions in Applied and Fundamental Research'. In: *The Euroschool Lectures on Physics with Exotic Beams, Vol. II*. Ed. by Jim Al-Khalili and Ernst Roeckl. Springer Berlin Heidelberg, 2006, pp. 191–238. DOI: 10.1007/3-540-33787-3_5.

[10] Gary J. Russell. 'Spallation Physics - An Overview'. In: ICANS-XI International Collaboration on Advanced Neutron Sources (Tsukuba, Japan, 22nd–26th Oct. 1990).

[11] B. Blank et al. 'Evaluation of fusion-evaporation cross-section calculations'. In: *Nuclear Instruments and Methods in Physics Research Section B: Beam Interactions with Materials and Atoms* 416 (2018), pp. 41–49. DOI: https://doi.org/10.1016/j.nimb.2017.12.003.

[12] *Experimental Nuclear Reaction Data (EXFOR)*. Database version of 31-05-2022. Brookhaven National Laboratory - National Nuclear Data Center (NNDC) and IAEA - Nuclear Data Section. URL: https://www-nds.iaea.org/exfor/.

[13] A Ferrari et al. *FLUKA: A multi-particle transport code (program version 2005).* CERN Yellow Reports: Monographs. Geneva: CERN, 2005. DOI: 10.5170/CERN-2005-010.

[14] T.T. Böhlen et al. 'The FLUKA Code: Developments and Challenges for High Energy and Medical Applications'. In: *Nuclear Data Sheets* 120 (2014), pp. 211–214. DOI: https://doi.org/10.1016/j.nds.2014.07.049.

[15] Malvin H. Kalos and Paula A. Whitlock. *Monte Carlo Methods.* Wiley-VCH, 2008.

[16] Pinelopi Christodoulou. 'An in situ gamma-spectrometry system for the characterization of non-conventional radionuclides for medical research.' MA thesis. Complutense Unsiversity of Madrid and CERN-MEDICIS, 2020. URL: https://cds.cern.ch/record/2732064.

[17] T.E Schlesinger et al. 'Cadmium zinc telluride and its use as a nuclear radiation detector material'. In: *Materials Science and Engineering: R: Reports* 32.4 (2001), pp. 103–189. DOI: https://doi.org/10.1016/S0927-796X(01)00027-4.

[18] Stefano Del Sordo et al. 'Progress in the Development of CdTe and CdZnTe Semiconductor Radiation Detectors for Astrophysical and Medical Applications'. In: *Sensors* 9.5 (2009), pp. 3491–3526. DOI: 10.3390/s90503491.

[19] Miguel Boratto. 'Semiconducting and Insulating oxides applied to electronic devices'. PhD thesis. 2018. DOI: 10.13140/RG.2.2.30070.29762.

[20] C. Kittel. *Introduction to Solid State Physics.* 6th Edition. John Wiley & Sons, Inc., 1986.

[21] Kromek. *About CZT: cadmium zinc telluride.* URL: https://www.kromek.com/cadmium-zinc-telluride-czt/ (visited on 05/06/2022).

[22] *InterSpec.* URL: https://github.com/sandialabs/InterSpec (visited on 24/05/2022).

[23] *Laboratoire National Henri Becquerel.* URL: http://www.lnhb.fr/nuclear-data/nuclear-data-table/.

[24] *Live Chart of Nuclides.* IAEA - Nuclear Data Section and NNDC, Brookhaven National Laboratory. URL: https://nds.iaea.org/relnsd/vcharthtml/VChartHTML.html.

[25] C.G. Ryan et al. 'SNIP, a statistics-sensitive background treatment for the quantitative analysis of PIXE spectra in geoscience applications'. In: *Nuclear Instruments and Methods in Physics Research Section B: Beam Interactions with Materials and Atoms* 34.3 (1988), pp. 396–402. DOI: https://doi.org/10.1016/0168-583X(88)90063-8.

[26] Cristina Müller et al. 'A Unique Matched Quadruplet of Terbium Radioisotopes for PET and SPECT and for - and –Radionuclide Therapy: An In Vivo Proof-of-Concept Study with a New Receptor-Targeted Folate Derivative'. In: *Journal of nuclear medicine : official publication, Society of Nuclear Medicine* 53 (2012). DOI: 10.2967/jnumed.112.107540.

[27] Nabanita Naskar and Susanta Lahiri. 'Theranostic Terbium Radioisotopes: Challenges in Production for Clinical Application'. In: *Frontiers in Medicine* 8 (2021). DOI: 10.3389/fmed.2021.675014.

[28] Cristina Müller et al. 'Alpha-PET with terbium-149: evidence and perspectives for radiotheragnostics'. In: *EJNMMI Radiopharmacy and Chemistry* 1.1 (2016). DOI: 10.1186/s41181-016-0008-2.

[29] Francesca Borgna et al. *Terbium-149 for targeted alpha therapy*. Tech. rep. CERN, 2021. URL: https://cds.cern.ch/record/2748660.

[30] Thomas Elias Cocolios. 'Tb-IRMA-V: Terbium ISOL Radioisotopes for Medical Applications in Flanders'. In: (2019). URL: https://cds.cern.ch/record/2666579.

[31] Reihnard Heinke and Cyril Bernerd. 'MELISSA laser lab: operation 2021'. In: MELISSA Collaboration Board (21st Nov. 2022).

[32] Vadim Maratovich Gadelshin et al. 'Terbium Medical Radioisotope Production: Laser Resonance Ionization Scheme Development'. In: *Frontiers in Medicine* 8 (2021). DOI: 10.3389/fmed.2021.727557.

[33] Vadim Maratovich Gadelshin et al. 'First laser ions at the CERN-MEDICIS facility'. In: *Hyperfine Interact.* 241 (2020), 55. 9 p. DOI: 10.1007/s10751-020-01718-y.

[34] Charlotte Duchemin et al. 'CERN-MEDICIS: A Unique Facility for the Production of Non-Conventional Radionuclides for the Medical Research'. In: *JACoW IPAC* 2020 (2021), THVIR13. 5 p. DOI: 10.18429/JACoW-IPAC2020-THVIR13.

[35] Charlotte Duchemin et al. 'CERN-MEDICIS: A Review Since Commissioning in 2017'. In: *Frontiers in Medicine* 8 (2021). DOI: 10.3389/fmed.2021.693682.

[36] Bertrand Dewit. 'Towards the first collection of 44Sc at CERN MEDICIS'. MA thesis. KU Leuven, 2017. URL: https://cds.cern.ch/record/2286388.

[37] V.M. Gadelshin et al. 'MELISSA: Laser ion source setup at CERN-MEDICIS facility. Blueprint'. In: *Nuclear Instruments and Methods in Physics Research Section B: Beam Interactions with Materials and Atoms* 463 (2020), pp. 460–463. DOI: https://doi.org/10.1016/j.nimb.2019.04.024.

[38] Yisel Martinez Palenzuela et al. 'The CERN-MEDICIS Isotope Separator Beamline'. In: *Frontiers in Medicine* 8 (2021). DOI: 10.3389/fmed.2021.689281.

[39] Kaat Spoormans. 'Radiolanthanide purification at CERN MEDICIS. An investigation of a novel radiation detection system'. MA thesis. KU Leuven, 2021. URL: http://cds.cern.ch/record/2773908.

[40] Katerina Chrysalidis, Reinhard Heinke and Shane Wilkins. *Report on laser ion throughput measurements with the MEDICIS laser ion source MELISSA*. 2020. DOI: 10.5281/zenodo.4248733.

[41] Reihnard Heinke. 'ISOLDE's high purity laser ion source LIST. Upgrades and Prospects for Run 3'. In: 76th Students' Coffee Meeting (21st Jan. 2021).

[42] Peter Sigmund. 'Theory of Sputtering. I. Sputtering Yield of Amorphous and Polycrystalline Targets'. In: *Phys. Rev.* 184 (2 1969), pp. 383–416. DOI: 10.1103/PhysRev.184.383.

[43] Hideaki Adachi and Kiyotaka Wasa. 'Thin Films and Nanomaterials'. In: *Handbook of Sputtering Technology*. Ed. by Kiyotaka Wasa, Isaku Kanno and Hidetoshi Kotera. 2nd Edition. William Andrew Publishing, 2012, pp. 3–39. DOI: https://doi.org/10.1016/B978-1-4377-3483-6.00001-2.

[44] *Quality Control in the Production of Radiopharmaceuticals*. TECDOC Series 1856. International Atomic Energy Agency, 2018. URL: https://www.iaea.org/publications/13422/quality-control-in-the-production-of-radiopharmaceuticals.

[45] Nic Gillings et al. 'EANM guideline on the validation of analytical methods for radiopharmaceuticals'. In: *EJNMMI Radiopharmacy and Chemistry* 5.7 (2020). DOI: 10.1186/s41181-019-0086-z.

[46] H. Verhoeven et al. 'Measurement of spallation cross sections for the production of terbium radioisotopes for medical applications from tantalum targets'. In: *Nuclear Instruments and Methods in Physics Research Section B: Beam Interactions with Materials and Atoms* 463 (2020), pp. 327–329. DOI: https://doi.org/10.1016/j.nimb.2019.04.071.

[47] *About MYRRHA*. URL: https://myrrha.be/about-myrrha (visited on 26/07/2022).

[48] Thierry Stora. 'MEDICIS scheme of operation in 2022'. In: 9th MEDICIS Collaboration Board (27th Apr. 2022).

[49] G. I. Klenov and V. S. Khoroshkov. 'Hadron therapy: history, status, prospects'. In: *Physics-Uspekhi* 59.8 (2016), pp. 807–825. DOI: 10.3367/ufne.2016.06.037823.

[50] Timothy D. Malouff et al. 'Carbon Ion Therapy: A Modern Review of an Emerging Technology'. In: *Frontiers in Oncology* 10 (2020). DOI: 10.3389/fonc.2020.00082.

[51] Marco Durante and Jürgen Debus. 'Heavy Charged Particles: Does Improved Precision and Higher Biological Effectiveness Translate to Better Outcome in Patients?' In: *Seminars in Radiation Oncology* 28.2 (2018), pp. 160–167. DOI: https://doi.org/10.1016/j.semradonc.2017.11.004.

[52] *Protoncentrum - UZ Leuven*. URL: https://www.particle.be (visited on 28/07/2022).

[53] Tom Depuydt. 'Proton therapy technology in the clinic'. In: 4th International Symposium on the System of Radiological Protection (ICRP) in conjunction with the 2nd European Radiological Protection Research Week (ERPW) (Paris, France, 10th–12th Oct. 2017).

[54] Wiel Kleeven. 'The Superconducting Synchrocyclotron Project S2C2'. In: *Accelerators for industrials and medical applications*. Joint Universities Accelerator School (JUAS) (European Scientific Institue, Archamps, 6th Jan.–13th Mar. 2014).

[55] Particle Therapy Co-Operative Group. *Particle therapy centres in clinical operation*. July 2022. URL: https://www.ptcog.ch/index.php/facilities-in-operation (visited on 30/07/2022).

[56] Malik Hadrich. 'Un nouveau pas vers le premier centre wallon de protonthérapie à Charleroi'. In: *7sur7* (26th Jan. 2021). URL: https://www.7sur7.be/belgique/un-nouveau-pas-vers-le-premier-centre-wallon-de-protontherapie-a-charleroi~a044ecd1/?referrer=https%5C%3A//www.google.be/.

[57] Proton Therapy IBA. *My experience with IBA - Prof. Dr. Karin Haustermans, Medical Director Protontherapy, ParTICLe*. YouTube. 2018. URL: https://www.youtube.com/watch?v=8Ogkj3Z6xj4 (visited on 01/05/2022).

[58] *An Overview of Proton Therapy.* URL: https://www.sccaprotontherapy.com/proton-therapy (visited on 02/05/2022).

[59] *Proteus®One. Think big, scale smart.* URL: https://www.iba-worldwide.com/pt/proton-therapy/proton-therapy-solutions/proteus-one (visited on 28/07/2022).

[60] *Chegg. Question: In a cyclotron, a magnetic field confines charged particles to circular paths while an oscillating electric field accelerates them.* URL: https://www.chegg.com/homework-help/questions-and-answers/cyclotron-magnetic-field-confines-charged-particles-circular-paths-oscillating-electric-fi-q14943185 (visited on 30/04/2022).

[61] Federal Agency for Nuclear Control. *Fifth meeting of the Contracting Parties to the Joint Convention on the Safety of Spent Fuel Management and on the Safety of Radioactive Waste Management.* 2014.

[62] Philippe Guetat et al. *Clearance levels for radionuclides in solid materials Application of exemption principles - Interim report for comment.* Tech. rep. Jan. 1996.

[63] *Koninklijk besluit van 20 juli 2001 houdende algemeen reglement op de bescherming van de bevolking, van de werknemers en het leefmilieu tegen het gevaar van de ioniserende stralingen (ARBIS). Bijlage IB Radioactieve afvalstoffen: voorwaarden en niveaus voor vrijgave bij onbeperkte hoeveelheden.* 20th July 2001. URL: https://www.jurion.fanc.fgov.be/jurdb-consult/plainWettekstServlet?wettekstId=11670&lang=nl.

[64] *NIRAS en haar partners.* URL: https://www.niras.be/niras-en-haar-partners (visited on 02/08/2022).

[65] NIRAS. *Ophaalcampagne radioactief afval bij ziekenhuizen - voorjaar 2014. NIRAS en ziekenhuizen maken samen werk van veilig beheer van radioactief afval.* 2014.

[66] James Ziegler. *Interactions of Ions with Matter.* URL: http://www.srim.org/.

[67] Nedal Aluminium BV. *Alloy Data Sheet EN-AW 6060 [AlMgSi].* 2017. URL: https://www.nedal.com/wp-content/uploads/2017/11/Nedal-alloy-Datasheet-EN-AW-6060.pdf.

[68] *Composition of Stainless Steels.* URL: https://material-properties.org/what-is-composition-of-stainless-steels-definition/ (visited on 07/08/2022).

[69] Royal Society of Chemistry. *Tin - Element information, properties and uses.* URL: https://www.rsc.org/periodic-table/element/50/tin (visited on 15/08/2022).

Appendix A

Poster on the ISOL Production of Tb at MEDICIS

To convey knowledge about the ongoing research on the production at MEDICIS of neutron-deficient Tb radioisotopes for medical applications, a poster was made that summarises some of the key concepts and developments. The poster was presented at the 8th International Symposium on Medical Radioisotopes (ISMERAD) in Antwerp on May 6, 2022. It is included on the following page.

The box titled "Collection Efficiencies" gives the efficiencies that were obtained for Tb collections from externally irradiated gadolinium targets at 30 MeV at ARRONAX, as well as from tantalum targets irradiated at 1.4 GeV at CERN. The latter represent the July and August ^{155}Tb collections discussed in chapter 4. The results show that the collection efficiency is higher for external irradiation of Gd at lower energy than for irradiation of Ta at high energy at CERN. As more than one parameter differs between these two situations, systematic research must be done for all of them to determine how the collection efficiency behaves as function of the individual parameters and how it can be optimised. That holds for proton energy, target material, target temperature, type of ion source (plasma ion source, surface ion source and/or laser ion source), total duration of the whole collection (i.e. from target irradiation until implantation, including transport time) and so on. Chapter 4 addresses a few of these parameters.

ISOL production of Tb isotopes for medical applications at CERN MEDICIS

W. Goossens[1], W. Wojtaczka[1], T. E. Cocolios[1], C. Bernerd[1,2], L. Popescu[3], T. Stora[2]
[1]KU Leuven, [2]CERN, [3]SCK-CEN
willemijn.goossens@student.kuleuven.be

The Terbium Quadruplet

Within the terbium radionuclide family, there are four isotopes of clinical interest. The members of the quadruplet have complementary decay characteristics, allowing them to be used for both therapy and diagnostics. The advantage of working with isotopes of the same element is that their chemistry is the same. This means that the pharmacokinetics and biodistribution will remain the same for all isotopes. The radiochemistry could thus be investigated for one isotope and later applied to all. [1]

- ^{149}Tb ($T_{1/2}$ = 4,118 h): targeted alpha therapy (TAT) + PET
- ^{152}Tb ($T_{1/2}$ = 17,5 h): PET
- ^{155}Tb ($T_{1/2}$ = 5,32 d): SPECT
- ^{161}Tb ($T_{1/2}$ = 6,89 d): electron therapy + SPECT

Production Routes

- ^{161}Tb: ^{160}Gd(n,γ)^{161}Gd → ^{161}Tb reaction at nuclear reactor (BR2, Belgium) [2]
- Others: proton-induced reactions on heavy targets (e.g. Ta, Gd) + ISOL at MEDICIS (Switzerland)

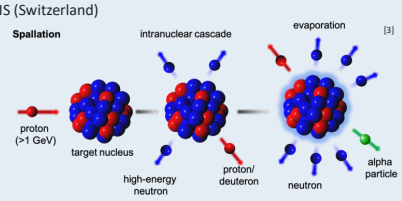

MEDICIS (CERN) = Medical Isotopes Collected from ISOLDE

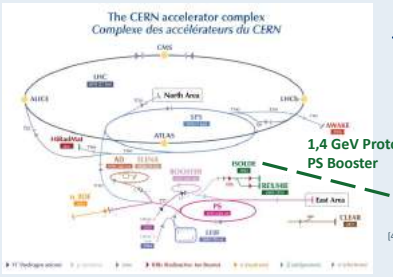

1,4 GeV Protons
PS Booster

Target Irradiation

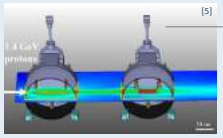

ISOLDE target MEDICIS target

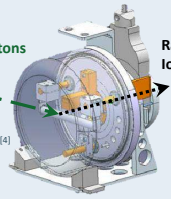

Radioactive Ion Beam

MEDICIS target station
- Radioisotope extraction & separation via ISOL
- Chemical separation
- Radiochemistry

Target transport
- Rail system
- Robot arm

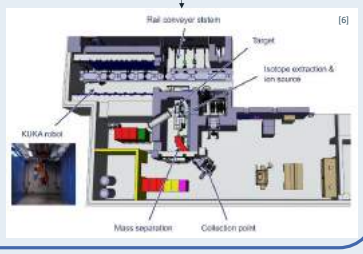

Isotope Separation On-Line (ISOL) at MEDICIS

- Proton beam impinges on heavy target
- Radioisotopes diffuse out of irradiated target under high temperatures
- Ion source: surface ionisation + element specific laser ionisation
- Magnetic mass separation

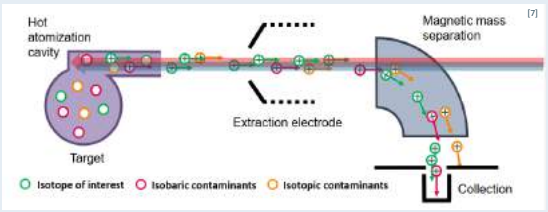

Target Irradiation

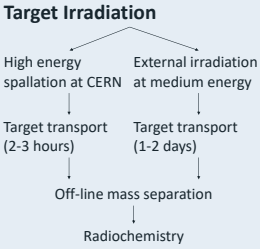

Laser Ionisation

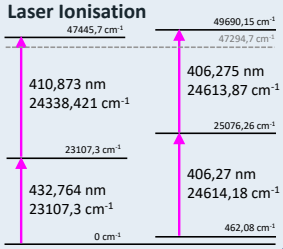

Collection Efficiencies

Overall efficiency:

$$\epsilon_{tot} = \epsilon_{diff} \times \epsilon_{eff} \times \epsilon_{ion} \times \epsilon_{sep} \times \epsilon_{trans} \times \epsilon_{decay}$$

1st Run (2018): External → 30 MeV protons on Gd target (at ARRONAX, Nantes)

$$\epsilon_{tot} = 1,2\%$$ [5]

2nd Run (2020): External → 30 MeV protons on Gd target (at ARRONAX, Nantes)

$$\epsilon_{tot} = 0,4\% - 11\%$$ [8]

3rd Run (2021): Internal → 1,4 GeV protons on Ta target

$$\epsilon_{tot} = 0,03\% - 0,1\%$$

- FLUKA simulation: 5,00 GBq ^{155}Tb produced in target
- Spectroscopy after collection: 4,72 MBq ^{155}Tb collected

Optimisation

- Proton energy
- Target material
- Ion source
- Preconditioning of target
- Target temperature for effusion
- Suppression of contaminants

⇒ Systematic research of all parameters ongoing
⇒ Operation review of MEDICIS[10]

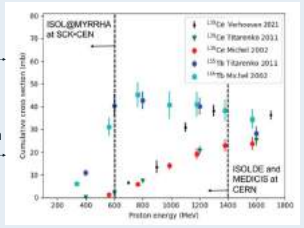

Cross sections for Ta(p,x)^{155}Tb and contaminant Ta(p,x)^{139}Ce
Figure adapted from [5]

Conclusion & Outlook

- Highest efficiencies for external irradiation at medium energy
- Optimisation for high energy spallation at CERN MEDICIS ongoing[10]: Target irradiation conditions, preheating of target, …
- Research towards ISOL@MYRRHA: 100 or 600 MeV protons
  → Principle already demonstrated at CERN MEDICIS
  → Less contaminant in ^{155}Tb collections expected

References

[1] C. Müller et al. "A unique matched quadruplet of terbium radioisotopes for PET and SPECT and for α- and β-radionuclide therapy: An in vivo proof-of-concept study with a new receptor-targeted folate derivative." Journal of nuclear medicine 53.12 (2012): 1951-1959.
[2] V.M. Gadelshin et al. "First laser ions at the CERN-MEDICIS facility." Hyperfine Interactions 241.55 (2020).
[3] ELENA: European Low Energy accelerator-based Neutron facilities Association, https://elena-neutron.iff.kfa-juelich.de/neutron-facilities
[4] T. Stora. "Radioactive Ion Sources." CAS – CERN Accelerator School: Ion Sources 007 (2013): 331-349.
[5] C. Duchemin et al., "CERN-MEDICIS: A Unique Facility for the Production of Non-Conventional Radionuclides for the Medical Research." Proc. IPAC'20 (2020): 75-79. doi:10.18429/JACoW-IPAC2020-THVIR
[6] B. Dewit. "Towards the first collection of 44Sc at CERN MEDICIS." *Master thesis* (2017).
[7] R. Heinke, C. Bernerd. "MELISSA laser lab: operation 2021." In presentation to the MELISSA collaboration board (2021).
[8] K. Spoormans. "Radiolanthanide purification at CERN MEDICIS." *Master thesis* (2021).
[9] H. Verhoeven et al. "Measurement of spallation cross sections for the production of terbium radioisotopes for medical applications from tantalum targets." Nuclear Inst. And Methods in Physics Research B 463 (2020): 327-329.
[10] T.Stora. "MEDICIS scheme of operation in 2022." 9th MEDICIS Board, CERN, 27 Apr 2022.

Appendix B

Ion Source Saturation: LIST

Associated to the discussion on ion source saturation in section 4.2.3, this appendix provides another example of a case where saturation was perceived. Fig. B.2 shows an excerpt of the GPS (General Purpose Separator) e-log at ISOLDE from May 24, 2022. The snippet describes the observation that, depending on the number of charges present, there is suppression of ionisation efficiency by the lasers in the high purity Laser Ion Source and Trap (LIST). The working of LIST relies on the inclusion of a RF quadrupole trap, which suppresses surface ionised species and thus promotes pure laser ionisation [41]. Fig. B.1 gives a schematic representation. The device can operate in two modes: Ion Guide (IG) mode, which is very similar to standard RILIS, and LIST mode, where the RF quadrupole trap is activated. The observation described in the e-log in Fig. B.2 tells us that the current of laser ionised ions is reduced significantly for high total beam currents in IG mode. In other words, the ion source becomes saturated when high ion currents pass through it. In LIST mode, however, saturation is avoided, thanks to the suppression of surface ions and a lower resulting beam current.

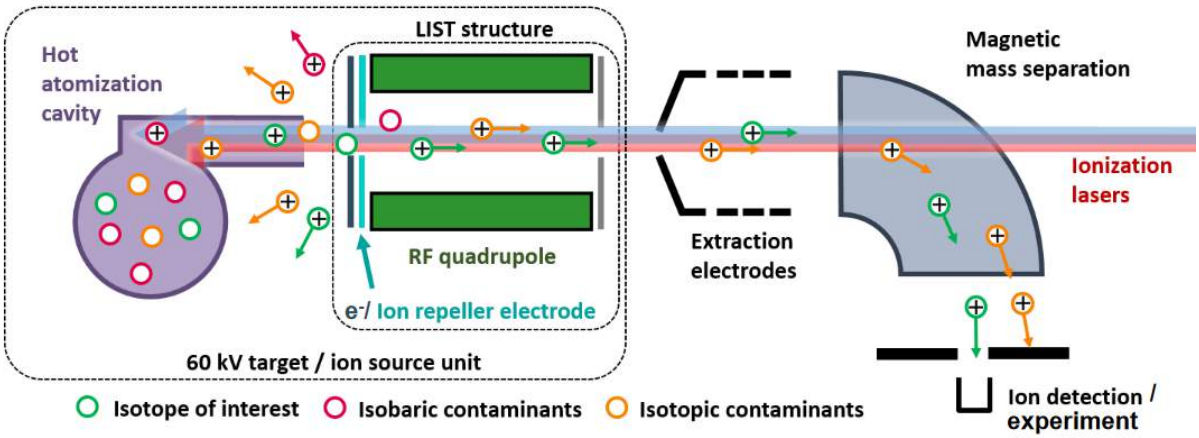

Figure B.1: Schematic representation of LIST included as ion source in the ISOL method. The separation of the isotope of interest from isobaric and isotopic contaminants throughout the different steps of the method is highlighted. Compare to Fig. 3.2 for a regular RILIS ion source. Picture from Ref. [41].

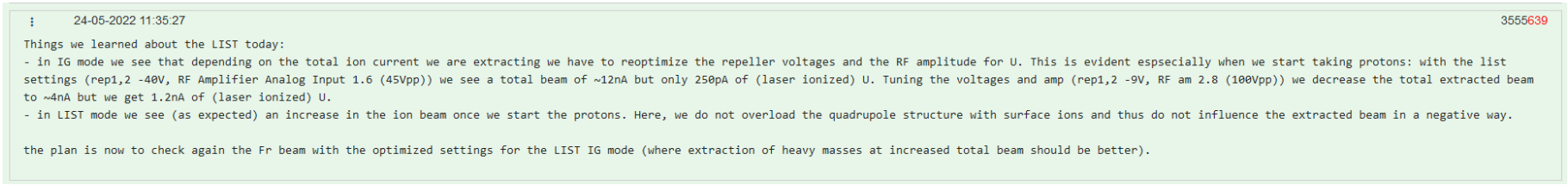

24-05-2022 11:35:27 3555639

Things we learned about the LIST today:
- in IG mode we see that depending on the total ion current we are extracting we have to reoptimize the repeller voltages and the RF amplitude for U. This is evident espsecially when we start taking protons: with the list settings (rep1,2 -40V, RF Amplifier Analog Input 1.6 (45Vpp)) we see a total beam of ~12nA but only 250pA of (laser ionized) U. Tuning the voltages and amp (rep1,2 -9V, RF am 2.8 (100Vpp)) we decrease the total extracted beam to ~4nA but we get 1.2nA of (laser ionized) U.
- in LIST mode we see (as expected) an increase in the ion beam once we start the protons. Here, we do not overload the quadrupole structure with surface ions and thus do not influence the extracted beam in a negative way.

the plan is now to check again the Fr beam with the optimized settings for the LIST IG mode (where extraction of heavy masses at increased total beam should be better).

Figure B.2: Entry in the e-log containing remarks on the saturation of the LIST ion source.

Appendix C

Risk Assessment for Spectroscopic Study of Cyclotron Parts

The spectroscopic study of proton-activated parts of the cyclotron from the proton therapy center PARTICLE in Leuven was not a standard type of experiment commonly performed at the IKS department. Hence, a thorough risk analysis had to be made before the experiment could start. This document was submitted to the Health, Safety and Environment (HSE) department for approval and advice. The reader may find the risk assessment together with the advice from HSE on the following pages.

DIENSTEN ALGEMEEN BEHEER
DIRECTIE STAFDIENSTEN ALGEMEEN BEHEER
DIENST VGM
WILLEM DE CROYLAAN 58 BUS 5530
3001 LEUVEN, BELGIË

APPLICATION FORM SPECIFIC RISK ANALYSIS FOR AN EXPERIMENT WITH OPEN RADIOACTIVE SOURCES

Use this guide to prepare a specific risk assessment for experiments with biological materials.
Complete this form in consultation with your HSE Network Contact Radioprotection (RP)[1].

1. Identification of the unit (users)

Applicant/contact person:	Willemijn Goossens	Unit:	IKS
Phone:	+32 498 38 01 16	Warehouse code[2]:	GZU
E-mail address:	willemijn.goossens@student.kuleuven.be	Manager[3]:	Riccardo Raabe
		Promotor:	Thomas Elias Cocolios

Persons who will initially perform the activity		
Name – first name	**u-/s-number/…**	**Staff group**
Goossens - Willemijn	r0694078	☐ KU ■ Student KU ☐ UZ ☐ VIB ☐ External: Fill in.
Wojtaczka - Wiktoria	u0140238	■ KU ☐ Student KU ☐ UZ ☐ VIB ☐ External: Fill in.
De Witte - Hilde	u0034658	■ KU ☐ Student KU ☐ UZ ☐ VIB ☐ External: Fill in.
Fill in.	Fill in.	☐ KU ☐ Student KU ☐ UZ ☐ VIB ☐ External: Fill in.
Fill in.	Fill in.	☐ KU ☐ Student KU ☐ UZ ☐ VIB ☐ External: Fill in.
Fill in.	Fill in.	☐ KU ☐ Student KU ☐ UZ ☐ VIB ☐ External: Fill in.
Fill in.	Fill in.	☐ KU ☐ Student KU ☐ UZ ☐ VIB ☐ External: Fill in.
Fill in.	Fill in.	☐ KU ☐ Student KU ☐ UZ ☐ VIB ☐ External: Fill in.

2. Identification of the experiment

2.1. **Title** (name) (max. 40 characters): Spectroscopic study of proton activated materials from the proton therapy center PARTICLE

2.2. **This risk analysis shall include:**

■ a new experiment,

☐ a change/extension of an existing experiment,

- This change/extension concerns (please indicate and describe further in the form):
  - ☐ Premises where the experiment takes place
  - ☐ Agents or devices that generate ionizing radiation
  - ☐ Extension
  - ☐ Other risks: Describe briefly.
- File or reference number previously submitted risk analysis (if known): Fill in.

2.3. **Desired start date** 6/12/2021 **Scheduled finish date:** 31/05/2022

[1] *You can find the members of your local HSE Network via KU Loket > VGM & Ruimtes > Mijn VGM > Mijn VGM-antenne*
[2] *If you do not know the warehouse code, please contact your HSE Network*
[3] *This is the hierarchically responsible person according to the official organization chart.*

3. Identification of agents

3.1. **Description of the radioactive sources used: products and quantities**

- Radionuclides used: Co-60 and other unknown species to be identified
- Products: Activated material from the proton therapy center PARTICLE
- Activity per experiment per radionuclide (MBq): Up to 0.29MBq per sample for a total of about 0.34MBq
- Purchased activity per radionuclide (MBq): Fill in.

4. Description of the experiment and the risk analysis

4.1. **Description of the actions, techniques and location:**

Number sub-experiment	Description of sub-experiment – actions and techniques (e.g., preparing the samples, carrying out the measurements, storing samples, measurements, …)
1	Measurements with CZT detector
2	Measurements with Germanium detector
3	Storing samples
4	Fill in.
5	Fill in.

Number sub-experiment	Building	Room	Containment level	Specifications room
1.	200D	00.89	Fill in.	■ own unit ☐ space allocated to another unit: Fill in.
2.	200D	00.89	Fill in.	■ own unit ☐ space allocated to another unit: Fill in.
3.	200D	00.80a/ 00.88	Fill in.	■ own unit ☐ space allocated to another unit: Fill in.
4.	Fill in.	Fill in.	Fill in.	☐ own unit ☐ space allocated to another unit: Fill in.
5.	Fill in.	Fill in.	Fill in.	☐ own unit ☐ space allocated to another unit: Fill in.

Type experiment:

☐ Binding experiment (adding radioactive material, incubation, separation, measurement)
☐ Commercial experiment (with standard protocol: RIA…)
☐ Radioactive marking (with 125I, 131I, …)
■ Other (specify): Activation Spectrometry

4.2. **Frequency experiment execution:**

☐ Daily
■ Weekly
☐ Monthly
☐ Less than monthly

4.3. **Add more information essential for performing the risk analysis (e.g., description, photos, reaction scheme) or refer to an appendix:**

The experiment will deal with various materials of unknown radioactive composition. The materials have been irradiated at the proton therapy centre PARTICLE at UZ Leuven and will all be submitted to a spectroscopic analysis to identify which radioactive isotopes are present.

Sub experiment 1: Measurements with a portable CZT detector (Kromek GR05)

Pictures of CZT setup similar to what will be used in this experiment:
The materials will be put on the table, in front of the CZT detector. To avoid contamination of the table, we shall put each of the samples in a sealed plastic bag.
The whole setup will be surrounded by a lead shielding.

The measurements shall take place in room 00.89. There are currently no other activities there, so there will be no exposure of people not involved in this experiment.

We will use signs to indicate that we are working with radioactive materials. Each sample will also be marked individually with activity cards. On these cards we shall indicate the number of counts per second until the present isotopes and their activity are identified. We shall update the cards as soon as more information is available from the analysis of the measurements.

Sub experiment 2: Measurements with a Germanium detector (Canberra)

For samples where more sensitivity is required, we will do additional measurements with a Germanium detector. This detector then replaces the CZT detector in the previous setup. The rest of the setup remains the same.

These measurements will also take place in room 00.89, which is already adapted to experiments with cooled Germanium detectors.

Sub experiment 3: Storage of the samples

The materials are stored in 3 barrels. Each sample will be put in a sealed plastic bag individually. We will number the plastic bags according to the codes in the table below. This table gives an overview of all samples with their measured dose rate, count rate, dose, and estimated Co-60 equivalent activity. It also indicates which samples are put in which barrel. The barrels are generally kept in room 00.80a. Only the barrel that is currently needed for experiments will temporarily be stored in room 00.88.

Prioriteit	Code	Omschrijving materiaal	Samenstelling	Gemeten dosistempo bij contact [µSv/h]	Gemeten teltempo bij contact [cps]	Datum meting	Geschatte Co-60 eq [Bq]	Welke transport-container	Opmerkingen
1	PTK34	Metalen plaatje aan plexiplaat degrader	?	< 1	15	26-11-2021	5,0E+02	# 1	
2	PTK22	koperen onderdeel (bestaat uit 3 Cu deel)	Cu	< 1	57	26-11-2021	2,3E+03	# 1	
3	PTK42	IC Cyclo (s/n 2017_84_ICCYCLO-06)	AlMgSi1; Stainless steel; Viton; Alumina; Ertacetal; Aluminium; Polyamide	4	860	26-11-2021	2,9E+05	# 1	Hotspot is binnenste window.
4	PTK12	Vacuum test plug	AlMgSi	2	750	29-11-2021	1,2E+04	# 1	Hotspot is aangeduid met een kruisje
5	PTK28A	Cooling cilinder	?	< 1	23	26-11-2021	2,7E+03	# 2	
6	PTK28B	Cooling cilinder	?	< 1	20	26-11-2021	2,6E+03	# 2	
7	PTK46A	Cooling cilinder	?	< 1	27	26-11-2021	2,4E+03	# 3	
8	PTK46B	Cooling cilinder	?	< 1	15	26-11-2021	2,0E+03	# 3	
9	PTK44A	Cooling cilinder	?	< 1	150	26-11-2021	1,6E+04	# 3	
10	PTK44B	Cooling cilinder	?	< 1	40	26-11-2021	5,2E+03	# 3	
11	PTK27A	Cooling cilinder	?	< 1	15	26-11-2021	1,6E+03	# 2	
12	PTK27B	Cooling cilinder	?	< 1	15	26-11-2021	2,0E+03	# 2	

Pictures of the barrels and some of the samples:

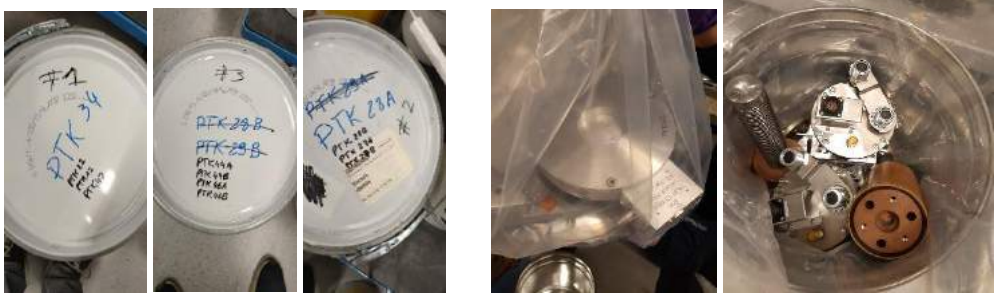

4.4. **Risks associated with the experiment:**

Risks associated with the use of ionizing radiation:

☐ Risk of inhalation / inhalation (powders / aerosols / volatile substances)
☐ Chance of splashing
☐ Chance of contamination of measuring equipment / devices
☐ Reuse glassware
■ Transport of radioactive material:
  ■ inside building or building complex: Describe the measures: Wearing appropriate protective equipment. 2-person activity: one for the transport and one for guiding/opening doors with clean hands.
  ☐ between KU Leuven buildings (not on public roads): Describe the measures: Fill in.
  ■ external transport (on public road)
☐ Other: Fill in.

Other risks associated with the experiment

☐ Incineration, freezing (☐ high or low temperatures, ■ cryogenic substances, …)
☐ Implosion, explosion (☐ high pressures, ☐ low pressures, ☐ negative pressure, …)
☐ Fire (☐ ovens, ☐ heating coils, ☐ Bunsen burner, ☐ oil baths …)
☐ Non-ionizing radiation (☐ NMR, ☐ lasers, ☐ UV lamps, ...)
☐ Electrocution (☐ naked contacts, ☐ humid environment, ☐ high powers, ...)
☐ Secluded employment remote room or place.
  Describe the conditions (e.g. with 2 present, dead man's alarm,…): Fill in.
☐ Risk of falling (☐ installations at a height, ☐ in height, ☐ difficult to reach, ...)
☐ Chemical risk: (products: ☐ flammable, ☐ toxic, ☐ carcinogenic,
  ☐ teratogenic, ☐ mutagen, …)
  Specify (name, CAS-nr., concentration, used quantity): Fill in.
☐ Biological risk (☐ pathogenic µ-organisms (specify): Fill in., ☐ GGO (specify host-vector-insert): Fill in.,
  ☐ cells (specify type and origin: Fill in., ☐ blood (specify origin): Fill in., ☐ lab animals (specify species, wild-type/knock-out, ...): Fill in., …)
☐ Gasses: Fill in.
☐ There is a chance that in the event of a serious incident, an independent alarm can **NOT** be given (e.g. use of highly toxic vapors or gases, risk of explosion, presence of suffocating gas, ...)
☐ Other: Fill in.

5. Precautions to be applied

If not all precautions can be applied, the HSE Department advises not to start the activities.

5.1. Collective protective equipment

Number sub-experiment[4]:	1	2	3	4	5
Environmental Dosimetry	■	■	■	□	□
Safety screen:					
- Plexi screen	□	□	□	□	□
- Lead shielding (wall of lead blocks, lead glass, …)	■	■	□	□	□
- Other: Fill in.	□	□	□	□	□
Closed system	□	□	□	□	□
Fume cupboard	□	□	□	□	□
Ventilated cupboard	□	□	□	□	□
Reactor cabinet	□	□	□	□	□
Local extractor	□	□	□	□	□
Spatial extractor	□	□	□	□	□
Drip tray underneath the installation / liquid waste	□	□	□	□	□
Signage (pictograms)	□	□	□	□	□
Other: Fill in.	□	□	□	□	□

5.2. Personal protective equipment[5]

Number sub-experiment[4]:	1	2	3	4	5
General protection:					
- Lab apron / work clothes	■	■	■	□	□
- Disposable overshoes	□	□	□	□	□
- Personal Dosimeter[6] (to be worn at chest height)	■	■	■	□	□
- Ring Dosimeter[7]	□	□	□	□	□
- Disposable hygiene hair net	□	□	□	□	□
- Disposable overall	□	□	□	□	□
- Disposable lab coat	□	□	□	□	□
- Other: Fill in.	□	□	□	□	□
Eye and face protection:					
- Safety glasses	□	■	□	□	□
- Global vision safety glasses	□	□	□	□	□
- Face shield	□	□	□	□	□
- Other: Fill in.	□	□	□	□	□
Respiratory protection:					
- Disposable dust mask P1	□	□	□	□	□
- Disposable dust mask P3	□	□	□	□	□

[4] *Number of the sub-experiment as indicated in section 4.1.*

[5] *Guidelines on obtaining Personal Protective Equipment (PPE's): via your HSE Network or the website of the HSE Department.*

[6+7] *More info on dosimeters can be found on the website of the HSE Department.*

- Disposable hygiene mask / surgical mask	☐	☐	☐	☐	☐
- Other: Fill in.	☐	☐	☐	☐	☐
Gloves:					
- Disposable nitrile EN 374	■	■	■	☐	☐
- Disposable vinyl EN 374	☐	☐	☐	☐	☐
- Nitrile EN 374	☐	☐	☐	☐	☐
- Cryogenic gloves	☐	■	☐	☐	☐
- Other: Fill in.	☐	☐	☐	☐	☐
Hearing protection:					
- Disposable earplugs	☐	☐	☐	☐	☐
- Banded earplugs	☐	☐	☐	☐	☐
- Ear muffs	☐	☐	☐	☐	☐
- Other: Fill in.	☐	☐	☐	☐	☐

5.3. **Specific preventative measures:**

■ Check for radioactive contamination:
- ■ immediate measuring by means of a contamination monitor (vb. Geiger-Müller, NaI, …)
- ☐ indirect measuring by means of rub/wash samples for liquid scintillation counts

☐ Check operation of the contamination monitor (battery voltage and background signal)
☐ Presence of decontamination material
☐ Check operation of fume cupboard
☐ Check glassware for cracks
☐ Other: Fill in.

5.4. **Work practices**

■ Apply the Code of Good Lab Practice
■ Follow the Course Radiation Protection (Basic Training)
- ☐ Provide internal training and guidance

☐ Organization of Purchase and acquisition of radioactive substances via SAP
■ Apply precautions when working with radioactive materials
☐ Organization of selective collection waste - radioactive waste

6. Disposal of waste – radioactive waste

6.1. **Indicate the expected waste fractions:**

Waste fraction + container *- Only 1 radionuclide is collected per container (with the exception of ^{3}H and ^{14}C).*		**Container present**
Disposable waste $t_{1/2}$ > 180 days and ^{3}H-^{14}C-waste	☐ Solid flammable: black plastic barrel 30 l	☐
	☐ Solid non-combustible: metal bucket 30 l	☐
	☐ Liquid scintillation counting vials: blue plastic barrel 30 l	☐
	☐ Liquid aqueous and liquid organic: plastic jerrycan 10 l (Collect aqueous waste separately from organic waste.)	☐
	☐ Injection needles: needle container and full needle containers in metal bucket 30 l	☐

	☐ Animal cadaver of mice and rats: in two separately hermetically sealed polyethylene zip bags and then: - *disposable* in white plastic bucket - *^{3}H and ^{14}C*: in black plastic container 30 l (The unit provides the polyethylene zip bags.)	☐ ☐
Perishable waste $t_{1/2}$ < 180 days	☐ Solid (flammable, non-flammable, filled needle containers): red plastic barrel 50 l	☐
	☐ Liquid scintillation counting vials: blue plastic barrel 30 l	☐
	☐ Liquid aqueous and liquid organic: plastic jerrycan 10 l (Collect aqueous waste separately from organic waste.)	☐
	☐ Animal cadaver of mice and rats: in two separately hermetically sealed transparent plastic bags and then in a black plastic barrel 30 l. (The unit provides the polyethylene zip bags.)	☐ ☐
Special waste	☐ Special waste → The container and the cost price are specifically determined by the HSE Department.	

7. Measures in special situations

7.1. **In case of failure and reactivation of utilities (incl. deviation from specifications):**

Utilities	Consequence(s) of failures	Is this a HSE problem: yes/no?	If yes, describe the measures
Electricity	Fill in.	Choose Yes/No	Fill in.
Ventilation	Fill in.	Choose Yes/No	Fill in.
Gas supply	Fill in.	Choose Yes/No	Fill in.
(Cooling)water	Fill in.	Choose Yes/No	Fill in.
Compressed air	Fill in.	Choose Yes/No	Fill in.
Inert atmosphere	Fill in.	Choose Yes/No	Fill in.
Vacuum	Fill in.	Choose Yes/No	Fill in.
Other: Fill in.	Fill in.	Choose Yes/No	Fill in.

Utilities	Consequence(s) when reactivating	Is this a HSE problem: yes/no?	If yes, describe the measures
Electricity	Fill in.	Choose Yes/No	Fill in.
Other: Fill in.	Fill in.	Choose Yes/No	Fill in.

7.2. **Can the experiment continue if the setup is left unattended (= continuous tests)?**

☐ Not applicable: the setup is never left unattended.
■ Yes.
In this case, the procedure "Continuous activities - unsupervised" is applied.
☐ No, additional measures are necessary.
Describe the additional measures: Fill in.
In addition, the procedure "Continuous activities - unsupervised" is applied.

7.3. **Is working outside normal working hours allowed?**

■ No.
☐ Yes. Describe which additional measures have been taken for this (e.g.: ventilation, presence second person, dead man's alarm,…): Fill in.

7.4. **Describe your procedure for a quick shutdown or the measures you will take when the building is evacuated:**

All potential risks should be contained and identified, so that no specific action is required.

7.5. **Describe the guidelines in case of a spill incident:**

N/A

8. Conclusion / Comments / Questions

Write down any additional comments or questions here

What is the most appropriate info to put on the activity cards (see description) until we have identified the present isotopes and activity for each sample?

Send the completed application / risk analysis form to your HSE Network Coordinator, your supervisor and the HSE Department.

9. Advice HSE Department

This space is reserved for advice from the HSE Department:

Administrative information

Division and its radioprotection file:	Nuclear and Radiation Physics – G.1.01.2
Description of the risk assessment:	**Spectroscopic study of proton activated materials from the proton therapy center PARTICLE**
Date of notification:	10/12/2021
HSE advisor:	An Wollebrants
HSE Department reference number:	**20210651**

We will also make this advice available on the HSE portal of the Department of Physics and Astronomy on the following location: Dienst VGM > Risicoanalyses > Specifieke RA Radioprotectie.

Advice of the HSE Department

The experiment can be carried out in compliance with the precautionary measures that are described in the risk assessment and in the following advice.

- For sending back the activated materials to UZ Leuven, it is necessary to contact the HSE Department. We will advise you on the packaging, labelling, … and we will carry out the transport as we did when the samples were send to you from UZ Leuven.
- *"What is the most appropriate info to put on the activity cards (see description) until we have identified the present isotopes and activity for each sample?"* We suggest to mention the yellow marked information in the table provided by UZ Leuven: sample code, measured dose rate in contact (µSv/h), date of measurement, estimated equivalent Co-60 activity (Bq).

Prioriteit	Code	Omschrijving materiaal	Samenstelling	Gemeten dosistempo bij contact [µSv/h]	Gemeten teltempo bij contact [cps]	Datum meting	Geschatte Co-60 eq [Bq]	tra co
1	PTK34	Metalen plaatje aan plexiplaat degrader	?	< 1	35	26-11-2021	5,0E+02	
2	PTK22	koperen onderdeel (bestaat uit 1 Cu deel)	Cu	< 1	57	26-11-2021	2,3E+03	
3	PTK42	IC Cyclo (s/n 2017_04_ICCYCLO-06)	AlMgSi1; Stainless steel; Viton; Alumina; Ertacetal; Aluminium; Polyamide	4	860	26-11-2021	2,9E+05	
4	PTR12	Vacuum test plug	AlMgSi	2	750	29-11-2021	1,2E+04	
5	PTK28A	Cooling cilinder	?	< 1	25	26-11-2021	2,7E+03	
6	PTK28B	Cooling cilinder	?	< 1	20	26-11-2021	2,6E+03	
7	PTK46A	Cooling cilinder	?	< 1	22	26-11-2021	2,4E+03	
8	PTK46B	Cooling cilinder	?	< 1	15	26-11-2021	2,0E+03	
9	PTK44A	Cooling cilinder	?	< 1	150	26-11-2021	1,6E+04	
10	PTK44B	Cooling cilinder	?	< 1	40	26-11-2021	5,2E+03	
11	PTK27A	Cooling cilinder	?	< 1	15	26-11-2021	1,6E+03	
12	PTK27B	Cooling cilinder	?	< 1	15	26-11-2021	2,0E+03	

Appendix D

Overview of Samples from PARTICLE

Fig. D.1 on the next page presents pictures of the different cyclotron parts from PARTICLE, on which the spectroscopic study in chapter 7 was performed. In total, there were 12 samples, each of them labelled by a code consisting of three letters followed by a two-digit number. Pictures are given for 6 out of the 12 samples. The remaining six are pairwise identical in appearance to the cooling cylinders given in Fig. D.1g and Fig. D.1h. An overview of the known information on the function, composition, weight, and dose rate for all cyclotron parts is given in Tab. D.1. This information was provided by the team from UZ Leuven (see also Ref [1]).

Table D.1: Overview of properties of the 12 cyclotron parts from PARTICLE.

Identification number	Function	Composition	Weight [kg]	Dose rate on contact [µSv/h]
PTR12	Vacuum test plug / Beam stop	AlMgSi	0.500	2*
PTK42	Ion chamber (IC CYCLO)	AlMgSi1, stainless steel, viton, alumina, ertacetal, aluminium, polyamide	1.5	4*
PTK34			0.500	< 1
PTK22		Cu	1.0	< 1
PTK44A	Cooling cylinder		3.0	< 1
PTK44B	Cooling cylinder		10.0	< 1
PTK28A	Cooling cylinder		3.0	< 1
PTK28B	Cooling cylinder		10.0	< 1
PTK46A	Cooling cylinder		3.0	< 1
PTK46B	Cooling cylinder		10.0	< 1
PTK27A	Cooling cylinder		3.0	< 1
PTK27B	Cooling cylinder		10.0	< 1

* The dose rate is significantly higher for PTK42 and PTR12 than for the other cyclotron parts, because the proton beam went straight through these samples, whereas it was only scattered onto the others

(a) Front view of sample PTR12.

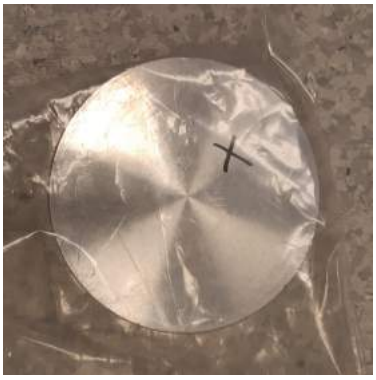

(b) Rear view of sample PTR12 with hotspot.

(c) Front view of sample PTK42 with hotspot.

(d) Rear view of sample PTK42.

(e) Sample PTK22.

(f) Sample PTK34.

(g) Sample PTK46A.

(h) Sample PTK46B.

Figure D.1: Pictures of the different cyclotron parts from the proton therapy center PARTICLE in Leuven. For PTK42 and PTR12, the hotspot is indicated by a cross.

DEPARTEMENT NATUURKUNDE EN STERRENKUNDE
Celestijnenlaan 200D bus 2412
3001 LEUVEN, BELGIË
tel. +32 16 32 71 24
fys.kuleuven.be